The computational investigation of a dinuclear manganese complex with Jahn-Teller compression and elongation

MSc Thesis

under the supervision of Assoc. Prof. Paul G. Plieger

Jenna K. Buchanan

Chemistry – Institute of Fundamental Sciences, Massey University

15 August 2017

Acknowledgements

I would like to express my sincere gratitude to my supervisor, Assoc. Prof. Paul Plieger, for his help, support and enthusiasm throughout this project. I would also like to acknowledge Prof. John McGrady from Oxford University for his specialist knowledge in modelling manganese complexes. I am grateful to Dist. Prof. Peter Schwerdtfeger and Mike Yap for allowing me to use the CTCP cluster for my calculations. A special thanks goes to David Nixon and Tyson Dais for their help in using Gaussian 09.

Abstract

Complexes that possess both Jahn-Teller compression and elongation effects at metal centres within the same molecule are extremely rare with only 11 examples known in the literature. Only two of these examples exist as discrete compounds. Jahn-Teller distortions influence metal-ligand bond lengths as well as the energy levels of the e_g and t_{2g} orbitals on the metal centre. The orientation of the Jahn-Teller axes have also been found to be an influential parameter in determining the exchange interactions in Mn^{III} dimers. X-ray crystallographic analysis of a di-manganese coordination compound serendipitously synthesised by Willoughby suggested that the complex possessed both Jahn-Teller compression and elongation. Willoughby's complex was synthesised in a very low yield and analysis of the crystals obtained by X-ray diffraction gave a structural determination of only moderate quality.

In this research project, the complex was computationally modelled in order to investigate the Jahn-Teller distortions and the coupling between the manganese centres. The bond lengths, molecular orbitals and spin density plot were explored in order to investigate these properties. The computational results gave strong evidence that Jahn-Teller compression and elongation were present in the di-manganese complex. The modelled ferromagnetic complex was found to be lower in energy than the modelled antiferromagnetic complex. Attempts were also made to re-synthesise the di-manganese complex in suitable quantity for complete structural and magnetic characterisation. Several different routes were trialled but after exhaustive attempts it was not possible to repeat the synthesis of the dinuclear complex.

Contents

Chapter One: Introduction

1.1 Magneto-structural correlations

Single molecule magnets (SMMs) are molecules which can act as a magnet due to having a large magnetic moment and magnetic anisotropy.[1] Magnetic anisotropy is the directional dependence of the magnetic properties, where a material is easier to magnetise along certain directions (easy axes) than others.[2] The magnetic moment of the SMM can be magnetised in response to an external magnetic field, with its spin either "up" or "down" along the axial magnetic anisotropy axis.[1] The barrier to relaxation for SMMs is given by the equation:

$$U = S^2|D| \quad (1)$$

where S is the spin state and D is the anisotropic zero-field splitting parameter.[3] Maximum values of S and D are desired in order to maximise the barrier to relaxation.[3]

SMMs are of interest due to their potential application in information storage and quantum computing.[4] In order to synthesise and study SMMs, it is of fundamental importance to understand the relationship between structure and magnetism.[5] Multiple structural properties have been found to influence the type and magnitude of the magnetic exchange interaction. As a molecule increases in size, the number of contributions to the magnetic exchange increases, which makes the understanding of the relationship between structure and magnetic properties much more difficult.[6] It is useful to instead explore the structure and properties of smaller molecules and manipulate their structures such that the magnetic exchange between the metal ions can be controlled. These small molecules can then be used as building blocks to construct larger molecules with selected magnetic properties.[5, 7]

The Jahn-Teller distorted Mn^{III} ion has often been used to construct SMMs due to its large single ion anisotropy.[7] The anisotropies of monomeric Mn^{III} complexes are typically $|D| \sim 4$ cm^{-1}.[3, 8] Strong ferromagnetic exchange between the neighbouring Mn centres is desired in order to construct SMMs.[5, 7] However, most di- and polynuclear Mn^{III} complexes exhibit very weak ferro- or antiferromagnetic interactions. The understanding of what controls the magnetic exchange between Mn centres is essential in order to construct complexes with the preferred ferromagnetic exchange.[7]

1.2 Ferromagnetic and antiferromagnetic coupling

Metal centres can interact with each other when the paramagnetic species are very close together or separated by a species which is able to transmit magnetic interactions.[9] In a ferromagnetic substance, the neighbouring spins are aligned in the same direction. In an antiferromagnetic compound, the neighbouring spins are antiparallel, meaning that they are aligned in opposite directions. Molecular complexes containing two ligand-bridged metal ions regularly exhibit antiferromagnetic coupling.[10]

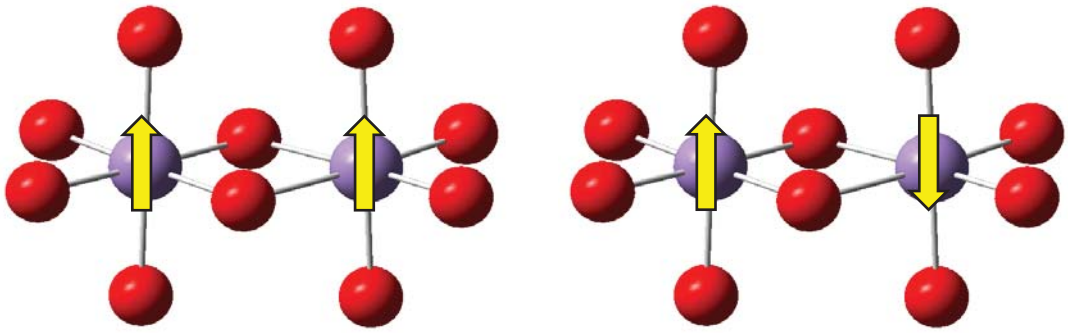

Figure 1. Illustration of ferromagnetic (left) and antiferromagnetic (right) coupling in a manganese dimer, where the arrows represent the alignment of spins.

A mechanism called *super-exchange* can occur through bridging ligands and results in antiferromagnetic coupling (Figure 2).[10] A small spin polarisation in an occupied orbital of a ligand is induced by the spin on one of the metal atoms. The spin of the adjacent metal atom becomes aligned antiparallel to this polarisation.[10]

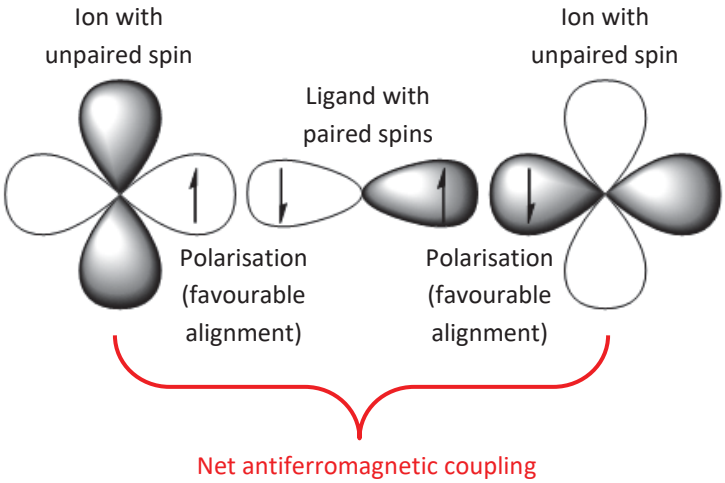

Figure 2. Antiferromagnetic coupling between two metal centres as a result of super-exchange through a bridging ligand. Reproduced from reference 10.

Many manganese dimers exhibit antiferromagnetic coupling, where one Mn has α *d*-electrons while the other Mn has β *d*-electrons.[7] If both manganese are in the +3 oxidation state and high-spin, this would result in $S = 0$ (Figure 3).

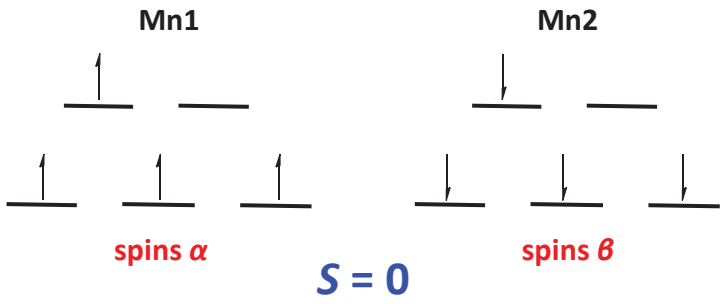

Figure 3. Illustration of the unpaired *d* electrons in an antiferromagnetic Mn^{III}/Mn^{III} dimer.

There are also examples of ferromagnetic coupling in manganese dimers.[7] For a Mn^{III}/Mn^{III} dimer, this would result in $S = 4$ (Figure 4).

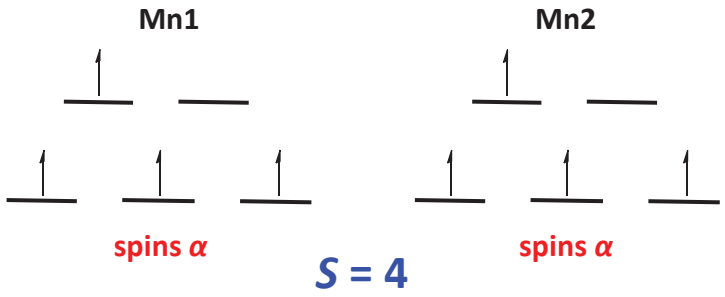

Figure 4. Illustration of the unpaired *d* electrons in a ferromagnetic Mn^{III}/Mn^{III} dimer.

1.2.1 Exchange coupling constant

An important parameter used to quantify the magnetic properties of dinuclear complexes is the exchange coupling constant (*J*). The exchange coupling constant is defined in the Heisenberg-Dirac-van Vleck spin-Hamiltonian:[11]

$$\hat{H} = -2J\hat{S}_1\hat{S}_2 \qquad (2)$$

The Heisenberg-Dirac-van Vleck Hamiltonian describes the coupling of two paramagnetic centres, S_1 and S_2. *J* is a measure of the strength of the interaction and is negative for antiferromagnetic interactions and positive for ferromagnetic interactions.[11a]

1.3 Jahn-Teller Theorum

The Jahn-Teller theorem suggests that a non-linear molecule cannot be stable in an orbitally degenerate electronic state. Instead, the molecule will distort to lower symmetry to remove the degeneracy.[12] The Jahn-Teller effect can be found in both organic compounds, such as cyclobutadiene, and transition metal complexes, such as $[Cu(OH_2)_6]^{2+}$.[13] It is more pronounced in octahedral complexes with d^9, low-spin d^7 and high-spin d^4 (e.g. high-spin Mn^{3+}) metal electrons.[9, 13] These metal ions have degenerate occupancy of the e_g subshell, which contains orbitals with metal-ligand antibonding character.[14]

In an octahedral environment, the two d orbitals $d_{x^2-y^2}$ and d_{z^2} (the e_g set) have lobes which point at the ligands, while the three d orbitals d_{xy}, d_{xz} and d_{yz} (the t_{2g} set) have lobes that point between the ligands.[13] The orbitals within each set are degenerate, but the e_g set are higher in energy than the t_{2g} set due to greater electrostatic repulsions between the d-electrons in the orbitals and the ligands (Figure 5).[13]

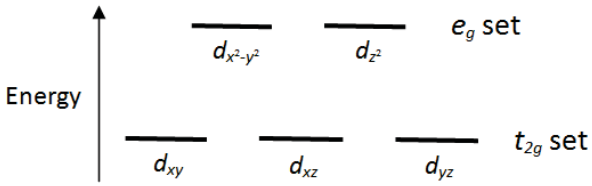

Figure 5. d orbitals in an octahedral coordination environment.[13]

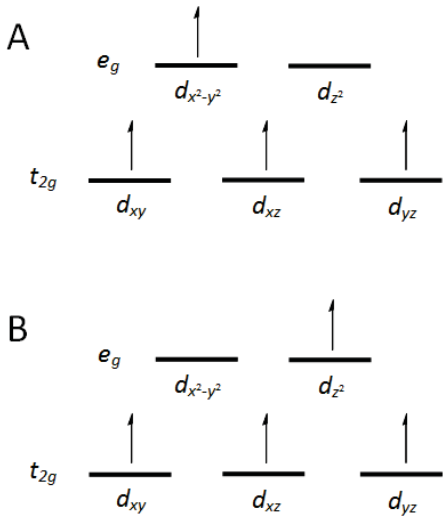

Figure 6. Two possible configurations of high-spin d^4 octahedral complexes: $d^1_{x^2-y^2}d^0_{z^2}$ (A) and $d^0_{x^2-y^2}d^1_{z^2}$ (B).[13]

Using high-spin Mn^{3+} (d^4) as an example, there is one vacancy in the e_g set either in the $d_{x^2-y^2}$ or d_{z^2} orbital. This results in two possible electronic configurations of equal energy: $d^1_{x^2-y^2}d^0_{z^2}$ or $d^0_{x^2-y^2}d^1_{z^2}$ (Figure 6).[13] According to Jahn and Teller, the octahedron must distort to reduce the symmetry so that the energies of the two configurations are not equal.[13] Two types of distortions are common: elongation where the two M-L bonds on the z axis are longer than the four bonds on the x and y axes, or compression where the two M-L bonds on the z axis are shorter.[13, 15] The effects of these distortions on the e_g and t_{2g} sets of orbitals are illustrated in Figure 7.

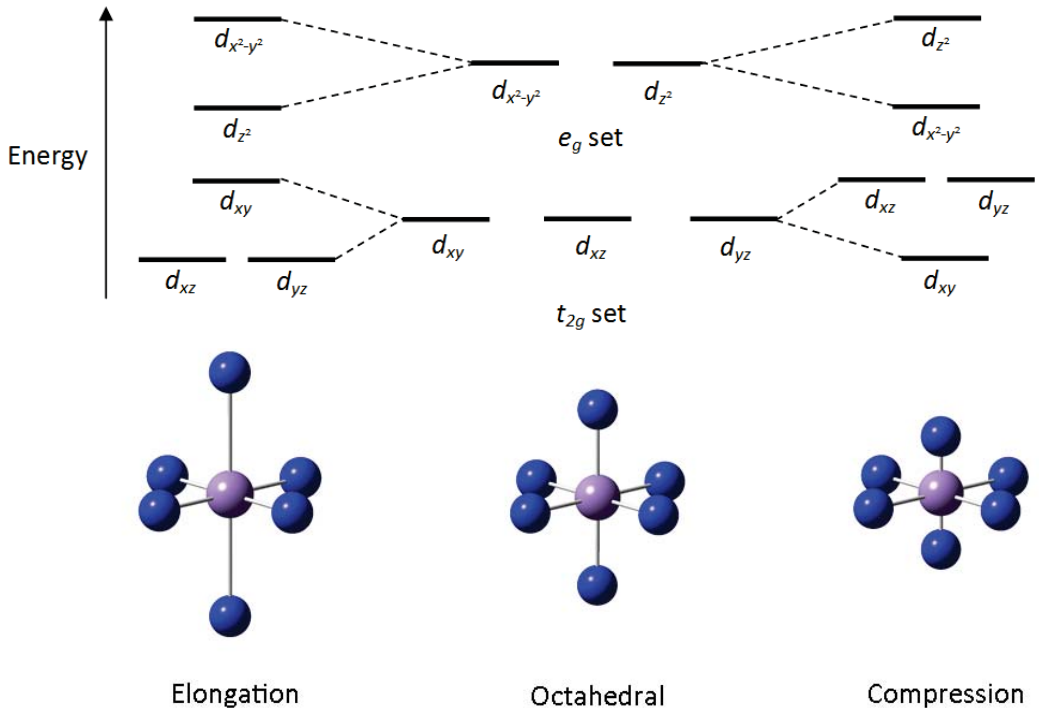

Figure 7. The effect of Jahn-Teller elongation and compression on energies of the *d* orbitals.[13]

In elongation, the ligands on the *z* axis move further away from the metal ion, which reduces the electrostatic repulsion between the ligands on the *z* axis and the d_{z^2} orbital. This leads to removal of the degeneracy of the $d_{x^2-y^2}$ and d_{z^2} orbitals upon elongation. The d_{z^2} orbital is reduced in energy while the energy of the $d_{x^2-y^2}$ orbital increases.[13] For high-spin Mn^{3+}, the fourth *d* electron fills the d_{z^2} orbital so that the electron configuration is $d^0_{x^2-y^2}d^1_{z^2}$ (Figure 8).[13] The lower energy of the d_{z^2} orbital due to the Jahn-Teller elongation causes the high-spin Mn^{3+} complex to be lower in energy.

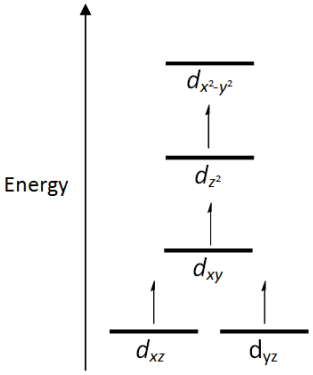

Figure 8. *d* orbital diagram for elongation in a high-spin d^4 complex.[13]

The opposite occurs in Jahn-Teller compression, where the ligands on the *z* axis are closer to the metal ion than the ligands on the *x* and *y* axes, causing the d_{z^2} orbital to be higher in energy than the $d_{x^2-y^2}$ orbital.[13] For high-spin Mn^{3+}, the fourth *d* electron fills the $d_{x^2-y^2}$ orbital so that the electron configuration is $d^1_{x^2-y^2}d^0_{z^2}$ (Figure 9).[13] This results in a reduced energy of the complex in comparison to an octahedral environment.

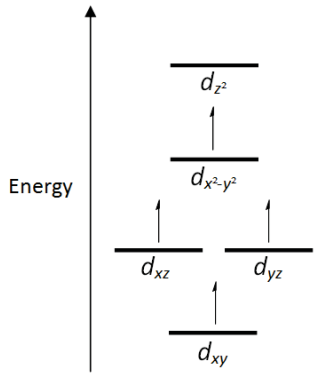

Figure 9. *d* orbital diagram for compression in a high-spin d^4 complex.[13]

1.3.1 Jahn-Teller-like distortions

According to some references, the Jahn-Teller effect only applies for six-coordinate complexes when all six ligands and all three molecular axes are the same. Complexes with six ligands which are not all identical would not possess *d*-orbital degeneracy, even if they were not distorted.[15] The metal-ligand bonds would be different lengths along the axial and equatorial planes caused by differences in metal-ligand bonding when there are different axial and equatorial ligands in a complex. This distortion is considered to be different to the "true" Jahn-Teller effect.[16] It is instead called a pseudo-Jahn-Teller distortion, which is a second-order Jahn-Teller phenomenon. The distortion in this case is caused by vibronic coupling of $d_{x^2-y^2}$ and d_{z^2} orbitals which are not degenerate, but are close in energy.[15] Even though complexes containing non-identical ligands are not considered to possess the "true" Jahn-Teller effect, the characteristics of these complexes exhibiting pseudo-Jahn-Teller distortions are usually very similar to those with the Jahn-Teller effect.[15]

The term Jahn-Teller effect is prevalently used in the literature to describe the distortions of six-coordinate complexes with non-identical ligands. These complexes exhibit similar structural characteristics, including further symmetry-lowering distortions, and orbital ordering as those possessing the true Jahn-Teller effect. Hence the distortions of these complexes can be described as "Jahn-Teller-like".[16] In the present study, the Jahn-Teller effect will be used to describe both complexes with "true" Jahn-Teller distortions and those with "Jahn-Teller-like" distortions, as this term is ubiquitously used in the literature for complexes containing non-identical ligands.

1.3.2 Literature structural examples exhibiting Jahn-Teller elongation and compression

A thorough search of the published literature found only eleven examples of substances for which both Jahn-Teller compression and elongation are present together in the same molecule. Doped materials or materials with pressure-induced changes were excluded from the search. Most of these examples are extended frameworks; only two exist as discrete compounds. The examples of discrete compounds are of the most relevance to the present study and will be covered in more depth.

The first example of a discrete compound with Jahn-Teller elongation and compression contained manganese ions in distorted octahedral environments. Dimitrakopoulou and co-

workers synthesised a mixed-valence hexanuclear manganese cluster $[Mn(II)_3Mn(III)_3O(OH)(CH_3pdol)_3(Hpdol)_3(pdol)](ClO_4)_4$.[17] The crystal structure revealed two distinct trinuclear units, Mn(II) / Mn(III) / Mn(II) and Mn(III) / Mn(II) / Mn(III), in a pseudocubane-like arrangement. This was the first reported compound with two trinuclear units in different valence distributions. Two of the Mn(III) ions showed Jahn-Teller elongation, while the other showed Jahn-Teller compression. Based on the magnetic susceptibility data, the interaction between two of the Mn(III) ions had a *J* value of 0.0 cm^{-1}. An X-band EPR spectrum was taken at various temperatures, but no values for *D* were recorded.[17]

The second example of a discrete compound with both types of distortions was a di-nuclear copper complex. De Munno and co-workers first synthesised, then investigated the crystal structures and magnetic properties of $[Cu_2(bpm)(H_2O)_4(SO_4)_2]\cdot 3H_2O$ (**1**) and $[Cu_2(bpm)(H_2O)_8](SO_4)_2\cdot 2H_2O$ (**2**) (bpm = 2,2'-bipyrimidine).[18] Compound **2** was obtained by recrystallisation of **1** in water. Both copper ions in **1** were in an elongated octahedral environment with two water molecules and two nitrogen atoms in the equatorial positions and two sulfate oxygens in the axial positions. In **1** the two metal centres were symmetrically equivalent but in **2** this symmetry equivalence was removed, resulting in slight structural variations in the two copper(II) atoms of the same molecule. The copper atoms in **2** were coordinated by two nitrogen atoms from bpm and four oxygen atoms from water molecules. In **2** both copper(II) ions were in a distorted octahedral CuO_6 coordination environment, with one elongated and the other compressed.[18] Therefore **2** was another example of both Jahn-Teller elongation and compression being present in a single complex. Magnetic susceptibility measurements were taken for both compounds. Both were found to exhibit antiferromagnetic coupling, which was relatively strong in **1** and weak in **2**. The weak coupling in **2** was attributed to the compressed Cu(1) having a magnetic orbital corresponding to a mixture of d_{z^2} and $d_{x^2-y^2}$ orbitals, reducing the σ in-plane overlap between the $d_{x^2-y^2}$ orbitals of the two copper atoms through the bpm ligand.[18]

There are several examples of extended frameworks with manganese ions in elongated and compressed octahedral environments. Mn_5VO_8 was found to contain both Jahn-Teller elongation and compression based on simultaneous analysis of X-ray diffraction and neutron diffraction data. One Mn(III) ion (Mn1) was in a compressed octahedral coordination environment, while a second site contained a Mn(III) ion (Mn2) in an elongated octahedral

environment. The other manganese ions (Mn3-5) were in the +2 oxidation state and in irregular tetrahedral environments.[19] In another example, Wandner and Hoppe prepared red crystals of $CaMnF_5$ by thermal decomposition of $CaMnF_6$. Two types of Mn(III) ions were observed: one in an elongated fluorine-octahedral environment, the other in a compressed fluorine-octahedral environment.[20] Three other examples of structures with both elongation and compression include $Ca_3Mn^{3+}{}_2O_2[Si_4O_{12}]$, $PbMn^{3+}{}_2O_2[Si_2O_7]$, and $BaSr_2Mn^{3+}{}_2O_2[Si_4O_{12}]$, which represent the synthetic silicate CMS-XI and the minerals kentrolite and taikanite respectively.[21] In each of these examples, there were two types of manganese atoms observed, one was in an elongated octahedral environment, while the other was in a compressed octahedral environment.[21]

Another example of an extended framework contained both manganese and gallium in distorted octahedral environments. Alekseeva and co-workers synthesised and determined the crystal structure of $Sr_2MnGaO_{4.78}F_{1.22}$.[22] The Mn atoms were in an "apically compressed" octahedral environment, while the Ga atoms were situated in a slightly elongated octahedral environment.[22]

There are also several examples of extended frameworks with Jahn-Teller elongation and compression distortions that do not contain manganese. The high temperature "HT" form of $Cr^{II}Nb^{IV}F_6$ consisted of elongated CrF_6 and compressed NbF_6 subunits due to the Jahn-Teller effect.[23] The order perovskite $BaCuWO_6$ was analysed via neutron powder diffraction at 10 K and room temperature. The Jahn-Teller effect caused the CuO_6 octahedron to be elongated parallel to the c-axis. The WO_6 octahedron was compressed. The compound exhibited two-dimensional antiferromagnetism.[24] β-$RbCrCl_3$ had a slightly distorted hexagonal perovskite structure. This phase was made up of chains of alternating compressed and elongated face-sharing octahedra.[25]

1.4 Influence of Jahn-Teller distortions on the magnetic properties of manganese dimers

The magnetic properties of a Mn^{III} ion have been shown to depend on the type of Jahn-Teller distortion, for instance, the axial zero-field splitting parameter (D) is positive for a compression and negative for an elongation distortion.[26] There has also been evidence that the type and relative orientation of the Jahn-Teller distortions influence the sign and magnitude of magnetic exchange (J) in bridged manganese dimers.[11b]

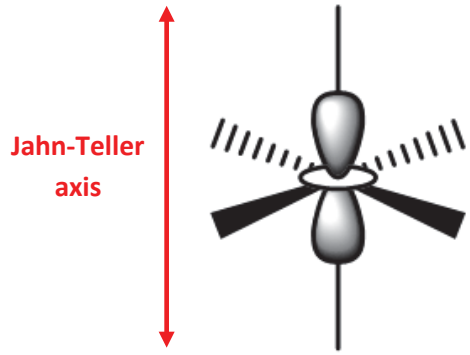

Figure 10. Illustration of the Jahn-Teller axis at a six-coordinate metal centre.

In both Jahn-Teller compression and elongation the distortions are taken along the z axis, with the x and y axes pointing toward the equatorial ligands.[26] The Jahn-Teller axis coincides with the orientation of the d_{z^2} orbital (Figure 10).[7]

In dinuclear μ-oxo Mn^{III} complexes where there is elongation at both Mn^{III} centres, a ferro- or antiferromagnetic interaction can be expected, depending on the rhombicity (E/|D|) of the system.[8, 11b] When there is compression in the direction of the oxo bridge, a ferromagnetic interaction has been predicted.[11b] For example, the structural and magnetic properties of seven (μ-oxo)bis(μ-carboxylato)dimanganese(III) compounds were compared by Corbella *et al*.[26] The two types of Jahn-Teller distortions were observed for these compounds and a correlation was found between ferromagnetic coupling and complexes with compressed Mn^{III} ions. It was also noted that the distortion (z) axis was different for the two types of distortion: the elongation axis passed through the carboxylate oxygen and the exogenous ligand, while the compression went through a bridging oxide.[26]

The interaction between the metal d orbitals of (μ-oxo)dimanganese(III) complexes with compressed Mn^{III} centres were investigated by Wieghardt and Girerd.[26-27] The importance of so-called "crossed interactions" between orbitals of different kinds on each metal were highlighted in this paper. At each Mn^{III} centre, the d_{z^2} orbital of each Mn^{III} ion was vacant due to the compression distortion. The mixing between d_{xy}, a singly occupied molecular orbital (SOMO) and the empty d_{z^2} orbital was found to be ferromagnetic. The importance of this contribution was inversely proportional to the energy difference between the two orbitals.

This contribution competed with the d_{yz}-d_{yz} interaction, which was antiferromagnetic.[26] Therefore the overlaps between *d* orbitals gave antiferromagnetic and ferromagnetic contributions, depending on whether one or both of the overlapping *d* orbitals were singly occupied.

Berg *et al*. investigated the magnetic interactions in five bis-μ-alkoxo Mn^{III} dimers using both experimental and theoretical methods.[7] The structural and magnetic properties of these complexes were compared to those of all other known bis-μ-alkoxo Mn^{III} dimers in the literature. Each compound was placed in one of three categories based on the relative orientation of the Jahn-Teller axes of the Mn^{III} ions with respect to one another as well as with respect to the μ-OR bridging plane. Type I dimers had the Jahn-Teller axes in a parallel orientation, perpendicular to the bridging plane of the complex (Figure 11). Type II had a parallel orientation in the μ-OR bridging plane, while Type III had a perpendicular orientation.[7]

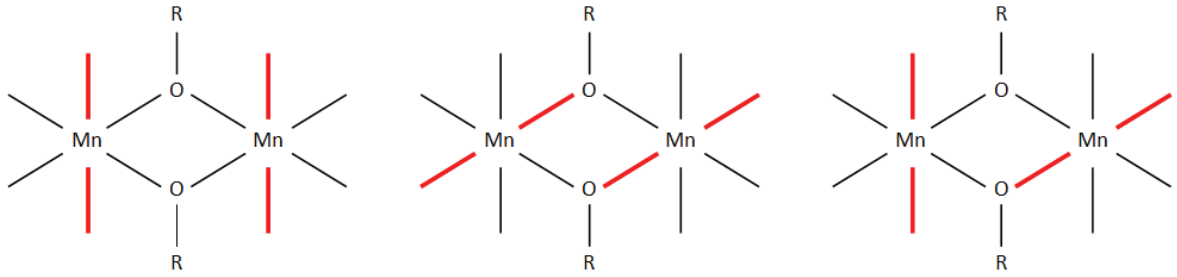

Figure 11. Type I-III structures of alkoxide bridged dimers which differ in the relative orientations of the Jahn-Teller axes (highlighted in red).[7]

Type I complexes were all found to be weakly antiferromagnetic with the magnetic exchange parameters (*J*) having values ranging from -8.2 cm^{-1} to -15.5 cm^{-1}. Type II had *J* values ranging from -1.68 cm^{-1} to +6.3 cm^{-1}, consistent with weakly antiferromagnetic to weakly ferromagnetic. Only two Type III complexes were identified and both exhibited ferromagnetic coupling. Both complexes possessed different ligands at each of their two Mn^{III} centres, leading to a low level of symmetry for this conformation.[7] However, both complexes had a much lower reported values for *D*, the axial anisotropy parameter, in comparison to typical measured values for high spin Mn^{III}.[8, 28] This was thought to be due to the perpendicular alignment of the Jahn-Teller axes.[8, 28]

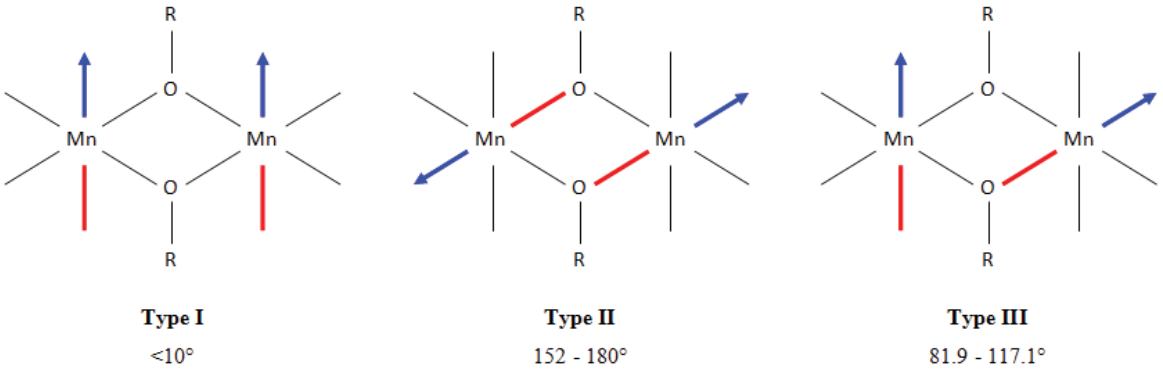

Figure 12. Illustration of the dihedral angle for Type I-III structures. The angle between the two blue arrows was measured for each type of structure.

The difference between the three types of dinuclear manganese complexes was further described by the dihedral plane between the Jahn-Teller axes, with a dihedral angle measured within the dihedral plane. Type I structures had dihedral angles <10°, type II structures had dihedral angles between 152° and 180°, and type III structures had dihedral angles in the range 81.9 - 117.1° (Figure 12). The *J* values were plotted against the dihedral angle and the grouping of the data clearly distinguished the types of structures.[7]

Density functional theory (DFT) calculations were carried out on selected structures of types I, II, and III.[7] With the exception of one of the type III complexes, the sign and magnitude of *J* were very similar to the experimentally reported values. The molecular orbitals of the selected structures were modelled. The net *J* values had both antiferromagnetic (J_{AF}) and ferromagnetic (J_F) contributions. J_F resulted from the overlap between the SOMOs and the unoccupied *d* orbitals, while J_{AF} resulted from the overlap between SOMOs. As the coordination sphere around each manganese atom was elongated, the unoccupied *d* orbital in each case was $d_{x^2-y^2}$. Therefore ferromagnetic interactions resulted from cross interactions between $d_{x^2-y^2}$ and other *d* orbitals, while the overlap between d_{xy}, d_{xz}, d_{yz} and d_{z^2} orbitals influenced the antiferromagnetic interactions.[7]

The computational analysis found that type I structures had a significant overlap between SOMOs but no significant interaction with the $d_{x^2-y^2}$ orbital, resulting in a larger J_{AF} contribution and a negligible J_F contribution. Type II structures had significant exchanges between SOMOs as well as significant cross-interactions with the $d_{x^2-y^2}$ orbital. Therefore type II structures had similar J_{AF} and J_F contributions, which led to a weak net exchange. The

cross-interactions were significant in type III structures, while fewer antiferromagnetic interactions were observed. The smaller J_{AF} and larger J_F resulted in a relatively strong net ferromagnetic exchange. This analysis was consistent with the experimental and calculated *J* values for the type I, II and III complexes.[7]

The magneto-structural correlations between four other structural parameters and the *J* values of the bis-μ-alkoxo Mn^{III} dimers were also investigated. These structural parameters included Mn-O-Mn angle, Mn-O distance, Mn-O-Mn-O dihedral angle and the out-of-plane shift of the alkyl group.[7] Overall, the relative orientation of the Jahn-Teller axes of the Mn^{III} atoms was found to be the most influential parameter in determining the exchange interactions in bis-μ-alkoxo Mn^{III} dimers.[7]

1.5 Computational Background

1.5.1 Density Functional Theory

Density Functional Theory (DFT) is a very popular computational method used in modelling inorganic systems. The basis of DFT is that the ground state electronic energy of a molecule can be expressed in terms of its electron density. It is an alternative to the traditional methods of quantum chemistry, which instead describe a system in terms of its many-electron wavefunction $\Psi(r_1 \ldots r_N)$.[29] DFT methods involve only a modest increase in cost over Hartree-Fock (HF) theory, while including many of the effects of electron correlation. When an appropriate functional and basis set are selected, DFT has been found to provide results that are of similar quality to those obtained by more elaborate methods at a greatly reduced computational cost.[30]

1.5.2 B3LYP

B3LYP (Becke's three-parameter hybrid exchange-correlation functional with the gradient correlation functional of Lee, Yang and Parr) is a hybrid DFT method which is one of the most widely used and accepted functionals in the literature. This method was suggested by Stephens *et al.* in 1994.[31] The values of the three parameters (a_0, a_x and a_c) of the exchange-correlation energy expression (equation 3) were taken directly from Becke's original paper.[32] In this paper Becke fitted the analogous B3PW91 (Becke's three-parameter hybrid functional with the non-local correlation of Perdew and Wang 91) functional to a set of atomization energies, ionization potentials, proton affinities, and total atomic energies.[33]

The B3LYP exchange-correlation energy expression is as follows:

$$E_{xc}^{B3LYP} = E_x^{LDA} + a_0(E_x^{HF} - E_x^{LDA}) + a_x(E_x^{GGA} - E_x^{LDA}) + E_c^{LDA} + a_c(E_c^{GGA} - E_c^{LDA}) \qquad (3)$$

where $a_0 = 0.20$, $a_x = 0.72$, and $a_c = 0.81$.

Table 1. List of components of the exchange-correlation energy expression and the corresponding definitions.

Component	Definition
E_x^{HF}	Hartree-Fock exact exchange functional.
E_x^{LDA}	Vosko-Wilk-Nusair local density approximation (LDA) to the exchange functional.
E_x^{GGA}	Generalised gradient approximation (GGA) from Becke's 88 exchange functional.[34]
E_c^{LDA}	Vosko-Wilk-Nusair LDA to the correlation functional.[35]
E_c^{GGA}	GGA from the correlation functional of Lee Yang and Parr for B3LYP.[36]

1.5.3 Basis sets

A basis set is a collection of mathematical functions used to describe a wave function for a molecular system.[37] Each combination of a basis set such as 6-31+G(d,p) with a theoretical method such as B3LYP results in a different approximation to the Schrödinger equation. When selecting a basis set for a computational model, there is a trade-off between accuracy and computational cost. Larger basis sets impose fewer restrictions on the locations of the electrons in space, allowing for more accurate approximations of the Schrödinger equation, but require greater computational resources.[37]

Most basis sets generate orbitals from a linear combination of Gaussian functions, called *primitive functions*.[37] In order to approximate the atomic orbitals, basis sets assign a group of basis functions to each atom in a molecule.[37] *Contracted functions* are basis functions which are composed of a linear combination of Gaussian functions, while *uncontracted functions* consist of a single Gaussian function.[37-38]

Cartesian Gaussian functions take the form:

$$g_{ijk} = Nx^i y^j z^k e^{-\alpha r^2} \quad (4)$$

where i, j and k are non-negative integers, α is a positive orbital exponent and N is a normalisation constant.[39]

1.5.3.1 The 6-31+G(d,p) basis set

The 6-31+G(d,p) basis set is a double-zeta split valence basis set, meaning it contains two sets of basis function for each valence orbital, each with a different value of α. The primed and unprimed orbitals denote the different sizes in Table 2. The inner orbitals are made up of six Gaussians, and the valence is described by three contracted Gaussians and one extended Gaussian (denoted by 6-31). The 6-31+G(d,p) basis set also features polarisation (d,p) and diffuse (+) functions, where orbitals with different shapes have been added to improve the basis set, this is referred to as *polarisation*. The added orbitals have larger angular momenta than are needed to describe the ground state of each atom at the HF level.[37] This basis set has both *d*-polarisation and *p*-polarisation, with *d*-functions added to heavy atoms (Li-Ar) and *p*-functions added to light atoms (H and He). This basis set also features *diffusion* on heavy atoms, by including valence orbitals which occupy a larger region of space. This is vital for systems where electrons may be relatively far from the nucleus.[37] The 6-31+G(d,p) basis set includes diffuse *s* and *p* functions. In the present study this basis set has been used to describe all non-metallic elements.

Table 2. Summary of the number of 6-31+G(d,p) basis functions and constituent primitive Gaussians for elements H – Ne.

Atomic Number	**1 – 2**		**3 – 10**	
Basis functions	*Basis functions*	*Consisting of:*	*Basis functions*	*Consisting of:*
	1s	3 Gaussians	1s	6 Gaussians
	1s’	1 Gaussian	2s, $2p_x$, $2p_y$, $2p_z$	3 Gaussians
	$2p_x$, $2p_y$, $2p_z$	1 Gaussian	2s’, $2p_x$’, $2p_y$’, $2p_z$’	1 Gaussian
			$3d_{xx}$, $3d_{yy}$, $3d_{zz}$, $3d_{xy}$, $3d_{xz}$, $3d_{yz}$	1 Gaussian
			3s, $3p_x$, $3p_y$, $3p_z$	1 Gaussian
Total number	5	7	19	32

1.5.3.2 LANL2DZ

LANL2DZ (Los Alamos National Laboratory 2 Double-Zeta) is an Effective Core Potential (ECP) type basis set which has commonly been used to model transition metal (TM) atoms.[40] ECP approaches allow chemically inactive core electrons to be treated as an averaged potential rather than actual particles. This reduces the computational cost and takes care of

relativistic effects.[40c] The outer electrons are represented by double-ζ atomic orbitals. Studies of TM containing systems have widely utilised density functional methods with the LANL2DZ basis set for the transition metal(s) and an all-electron Pople type basis set for all other atoms.[40c] Structures of transition metal complexes, including manganese complexes, have been successfully predicted by methodologies using B3LYP and the LANL2DZ basis set.[41] In the present study this basis set has been used to describe the manganese atoms.

1.5.4 Closed shell and open shell calculations

Closed shell systems have equal numbers of spin up (α) and spin down (β) electrons, which are divided into pairs with opposite spin. *Spin restricted* models are used for calculations on closed shell molecules.[42] The spin restricted model assumes that all molecular orbitals are doubly occupied, with each orbital containing two electrons of opposite spin. Each electron pair in a restricted calculation is forced into a single spatial orbital.[42] Figure 13 depicts five orbitals of a closed shell system, including the three highest energy doubly occupied orbitals (8, 9 and 10), and the two lowest energy unoccupied orbitals (11 and 12).

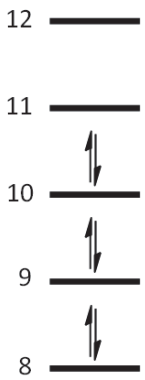

Figure 13. Example of a closed shell system.

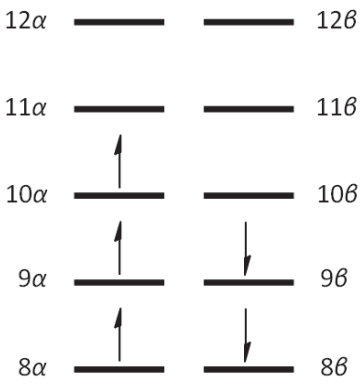

Figure 14. Example of an open shell system.

Molecules with unequal numbers of α and β electrons (unpaired electrons) are referred to as open shell systems. For these systems, a *spin unrestricted* model is used. Spin unrestricted calculations consider the spin up and spin down electrons separately, by using separate α and β spatial orbitals.[42] Figure 14 shows five orbitals of an open shell system with one unpaired electron, where there are separate α and β orbitals. The orbital diagram shows the unpaired electron in orbital 10α, paired electrons in orbitals 8 and 9 as well as two unoccupied α orbitals and three unoccupied β orbitals.

1.5.5 Broken symmetry approach

The broken symmetry approach, developed by Noodleman *et al.*, is a method used to calculate antiferromagnetic spin states. It has been widely used to model weakly coupled polymetallic systems and describe their structural and magnetic properties.[43] In the broken symmetry approach, the symmetry elements connecting the two metal centres are removed and an asymmetry in the initial spin density is imposed by the two metal centres having opposite spins.[43] A spin unrestricted calculation is performed, allowing individual electrons to localise on one centre or the other, but only if this is energetically favoured over delocalisation. This means that α and β electrons are able to localise on opposite sides of the molecule, giving the antiferromagnetic state. Through use of the broken symmetry approach, a range of antiferromagnetic coupling modes are possible, from weak antiferromagnetic coupling to strong metal-metal bonding modes.[44] The broken symmetry state contains a weighted average of the $M_s = 0$ components of all spin states; it is not a pure antiferromagnetic spin singlet.[43] The broken symmetry approach has been used to approximate the antiferromagnetic state of many transition metal dimers.[44]

1.5.6 Calculating the exchange coupling constant

A number of different equations have been proposed to determine the exchange coupling constant of a dimer from the calculated broken-symmetry and high-spin states. The appropriateness of each approximation is a subject of debate in the literature.[11a]

Using the Heisenberg-Dirac-van Vleck spin-Hamiltonian (equation 2) there are three equations that can be used to calculate J.[11]

$$\hat{H} = -2J\hat{S}_1\hat{S}_2 \tag{2}$$

The equation originally proposed by Noodleman assumes the weak interaction limit between metal centres:[11a, 45]

$$J = -\frac{E_{HS} - E_{BS}}{4S_1S_2} \tag{5}$$

where E_{HS} and E_{BS} are the calculated energies of the high-spin and broken symmetry states respectively. S_1 and S_2 are the spins of the two centres.[11a]

Where there is strong coupling, the equation advocated by Ruiz *et al.* can be applied:[11a, 46]

(6)

$$J = -\frac{E_{HS} - E_{BS}}{4S_1S_2 + 2S_2}$$

It has also been claimed that this equation can be used in cases of moderate or weak coupling.[11a]

Yamaguchi proposed an alternative formulation, which covers the range of coupling situations:[11, 47]

$$J = -\frac{E_{HS} - E_{BS}}{\langle \hat{S}^2 \rangle_{HS} - \langle \hat{S}^2 \rangle_{BS}} \quad (7)$$

where $\langle \hat{S}^2 \rangle_{HS}$ and $\langle \hat{S}^2 \rangle_{BS}$ are the total spin angular momentum expectation values for the high-spin and broken-symmetry states respectively.[11b]

The equation proposed by Yamaguchi will be used in the present study to calculate the exchange coupling constant as it is suitable for a range of coupling situations.

1.6 Modelling of manganese dimers and Jahn-Teller distortions using DFT methods

Density functional theory has been used to model a variety of manganese dimers. One particular consideration that must be made when modelling manganese dimers is whether the coupling between the two manganese ions is ferromagnetic or antiferromagnetic. Jahn-Teller distortions have also been investigated using DFT. A number of papers modelling manganese dimers and/or Jahn-Teller distortions most relevant to the present study are discussed below.

McGrady and Stranger have used DFT methods for the modelling of manganese dimers. The electronic and structural properties of the complex $Mn_2O_2(NH_3)_8^{z+}$ in three different oxidation states: $Mn_2^{IV/IV}$ (z = 4), $Mn_2^{III/IV}$ (z = 3) and $Mn_2^{III/III}$ (z =2) were investigated.[44] The $Mn_2^{III/III}$ complex is of particular interest having parallels with the present study. Magnetic measurements on each of the complexes suggested that the two manganese ions were antiferromagnetically coupled in each oxidation state, which gave an S = 0 ground state for the $Mn_2^{III/III}$ complex.[44] Unrestricted DFT calculations were performed to optimise the structure of the complexes, with the broken-symmetry methodology applied in order to model the antiferromagnetically coupled systems. The axial Mn-NH_3 bonds in the $Mn_2^{III/III}$ complex were observed to be elongated, which was attributed to the Jahn-Teller effect. The composition of the molecular orbitals was investigated, and it was found that the highest occupied molecular orbital (HOMO) was mostly composed of majority-spin d_{z^2} orbitals. A higher energy orbital had majority-spin $d_{x^2-y^2}$ character. This ordering of the *d* orbitals was consistent Jahn-Teller elongation, as the lengthening of the Mn-NH_3 axial bond reduced the ligand field and stabilised the d_{z^2} orbital.[44]

Inglis *et al.* also explored the magnetic coupling of a manganese dimer using DFT methods. The complex $[Mn^{III}_2Zn^{II}_2(Ph\text{-}sao)_2(Ph\text{-}saoH)_4(hmp)_2]$ (**1**) was serendipitously synthesised, and the complex had a magnetic core comprising of two symmetry equivalent Mn(III) ions linked by two symmetry equivalent oxime moieties.[48] DFT studies were performed on a simplified model complex of **1** in order to investigate the magnetic coupling. Calculations were completed with the Gaussian 09 program, using the B3LYP functional. Guess functions generated by the Gaussian fragment tool were used to obtain the unrestricted solutions of the antiferromagnetic spin state, and the broken symmetry approach was used to describe these

solutions. The DFT calculations determined that the Mn(III) ions were ferromagnetically coupled, which was in agreement with DC magnetic susceptibility measurements performed on the complex.[48]

Barone *et al.* modelled the di-oxo bridged dinuclear complexes $[Mn_2O_2(NH_3)_8]^{n+}$ (n = 0 – 4) using DFT in order to mimic the active site of biologically important enzymes.[49] The structures of the complexes were optimised using the broken symmetry wave function and the Becke-Perdew gradient-corrected functional. The exchange-coupling constant was calculated, which involved determination of the energies of the spin multiplets of the dimer. The calculations indicated that the manganese ions were antiferromagnetically coupled in all of the compounds, however the strength of the coupling was overestimated in comparison to the experimental values. This overestimation was considered to be a common drawback of broken symmetry calculations. In the Mn^{II}/Mn^{III} and Mn^{III}/Mn^{IV} structures the Mn^{III} centres were in axially elongated environments, but the Jahn-Teller distortions were not further investigated.[49]

Sameera, McKenzie and McGrady optimised the structure of the dicationic manganese dimer $[Mn(II)_2(mcbpen)_2(H_2O)_2]^{2+}$ using the Gaussian 03 program with the hybrid B3LYP functional and the LANL2DZ basis set.[50] The calculations utilised the spin-unrestricted Kohn-Sham (UKS) formalism. The broken symmetry methodology was used to obtain the antiferromagnetic electron configurations. The ground state was determined to be a broken-symmetry singlet (M_S = 0) with two localised high-spin (S = 5/2) Mn(II) centres with net spin densities of -4.89 and +4.89. The corresponding ferromagnetically coupled (S = 5) state was found to be almost identical in structure and only slightly higher in energy (0.1 kcal mol^{-1}).[50]

Gostynski, Rooyen and Conradie investigated Jahn-Teller distortion in different isomers of $[Mn(CF_3COCHCOC_4H_3S)_3]$, both experimentally and computationally.[51] Different electronic states of $[Mn(acac)_3]$ (the best known [Mn(β-diketonato)$_3$] complex) were optimised in order to justify the computational approach. A number of functionals (including B3LYP) were used and they correctly predicted the high spin state (S = 2) of $[Mn(acac)_3]$. The filled d_{z^2} orbital and unfilled $d_{x^2-y^2}$ orbital of $[Mn(acac)_3]$ led to the conclusion that the elongation present in the complex was due to the Jahn-Teller effect.[51] The same functionals were then used to model the isomers of $[Mn(CF_3COCHCOC_4H_3S)_3]$. All of the isomers had

the electronic ground state of $d^1_{xy}d^1_{xz}d^1_{yz}d^1_{z^2}$ and axial Mn-O bonds longer than the equatorial Mn-O bonds, which gave evidence for Jahn-Teller elongation being present.[51]

Ouyang, Shi and Lei used the general gradient approximation GGA+U method (generalised gradient approximation with the Hubbard parameter, *U*, which describes the effective on-site electronic interaction) to reproduce the Jahn-Teller distortion present in $LiMnO_4$.[52] In $LiMnO_4$, the manganese ions have mixed valence states of +3 and +4. With the GGA+U method, the e_g orbitals were split by approximately 0.5 eV, with the filled d_{z^2} orbital lower in energy than the $d_{x^2-y^2}$ orbital. The elongation of the Mn-O bonds along the z-axis was therefore attributed to the Jahn-Teller effect.[52]

In summary, the broken symmetry approach is commonly used to model antiferromagnetic coupling in manganese dimers. The ordering of the energies of the d_{z^2} and $d_{x^2-y^2}$ orbitals in a manganese dimer can be compared to provide evidence for the Jahn-Teller effect.

1.7 Background of the dinuclear manganese complex under investigation

In 2011, Amy Willoughby serendipitously synthesised a new dinuclear manganese complex (Figure 15).[53] Based on the X-ray crystallographic analysis, the dinuclear complex appeared to possess both Jahn-Teller-like elongation and compression.[53] Unfortunately, due to time constraints the complex remained largely uncharacterised.

1.7.1 X-ray crystallographic analysis

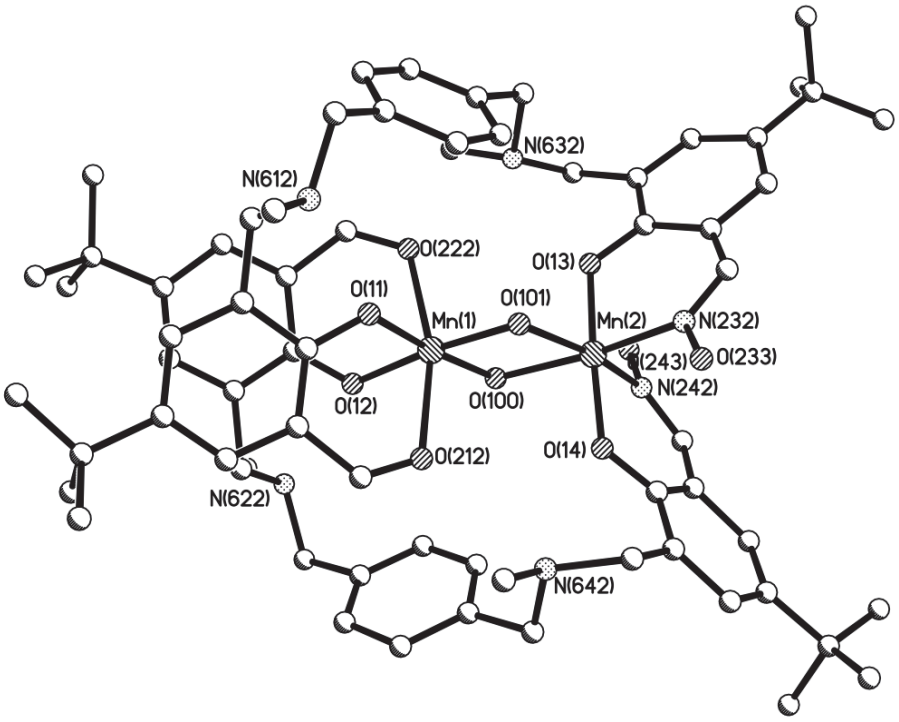

Figure 15. X-ray structure of the dinuclear complex synthesised by Willoughby.[53]

The di-manganese complex crystallised in the form of black, fine, rod shaped crystals, one of which was used for the X-ray structure determination.[53] The dinuclear complex featured two manganese centres each in an octahedral coordination environment. Mn(1) had two phenolates and two bridging oxygens in the equatorial positions and two carbonyl oxygens in the axial positions. Mn(2) had two oximes and two bridging oxygens in the equatorial positions and two phenolates in the axial positions. Both octahedrons were distorted. The axial bonds of Mn(1) were longer than the equatorial ones (Table 3), which suggested Mn(1) was Jahn-Teller elongated. The axial bonds of Mn(2) were shorter than the equatorial ones (Table 3), which suggested Mn(2) was Jahn-Teller compressed. It was initially thought that the two manganese were in different oxidation states, with Mn(1) in a +3 oxidation state and

Mn(2) in a +2 oxidation state.[53] However, it was later found that both manganese were Mn(III).[54]

Table 3. Coordination bond lengths measured from the X-ray crystal structure of Willoughby's complex.[53]

Atoms	Type of coordination bond	Bond length (Å)
Mn1-O11 (phenolate)	equatorial	1.926(4)
Mn1-O12 (phenolate)	equatorial	1.943(4)
Mn1-O100 (bridging oxygen)	equatorial	1.913(4)
Mn1-O101 (bridging oxygen)	equatorial	1.917(4)
Mn1-O212 (aldehyde)	axial	2.281(5)
Mn1-O222 (aldehyde)	axial	2.258(4)
Mn2-O13 (phenolate)	axial	1.882(5)
Mn2-O14 (phenolate)	axial	1.893(5)
Mn2-O100 (bridging oxygen)	equatorial	2.085(5)
Mn2-O101 (bridging oxygen)	equatorial	2.079(4)
Mn2-N232 (oxime)	equatorial	2.094(6)
Mn2-N242 (oxime)	equatorial	2.096(7)

1.7.2 Synthesis

Based on the X-ray structure, each ligand contained one oxime group and one aldehyde group.[53] The non-coordinated form of the ligand is given in figure 16. The complexation reaction had been undertaken from the fully oximated di-oxime. According to ^{1}H NMR analysis of the reactant ligand, the di-oxime still contained a small impurity of the mono-oxime (~ 6%).[53] Therefore, the complexation reaction may have involved partial hydrolysation of the di-oxime to form the ligand, either during complexation or upon crystallisation, or the complex may have been formed from the mono-oxime impurity present.

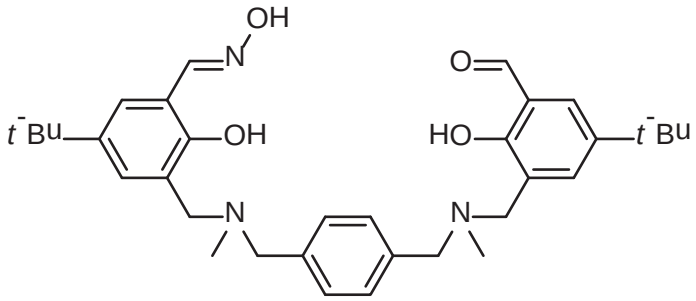

Figure 16. (1*E*,1'*E*)-5-*tert*-Butyl-3-(((4-(((5-*tert*-butyl-2-hydroxy-3-((*E*)(hydroxyimino)methyl)benzyl)(methyl)amino)methyl)benzyl)(methyl)amino)methyl)-2-hydroxybenzaldehyde (**L2**).[53]

The di-oxime (**L1**) was synthesised based on the method of Stevens and Plieger (Figure 17).[55]

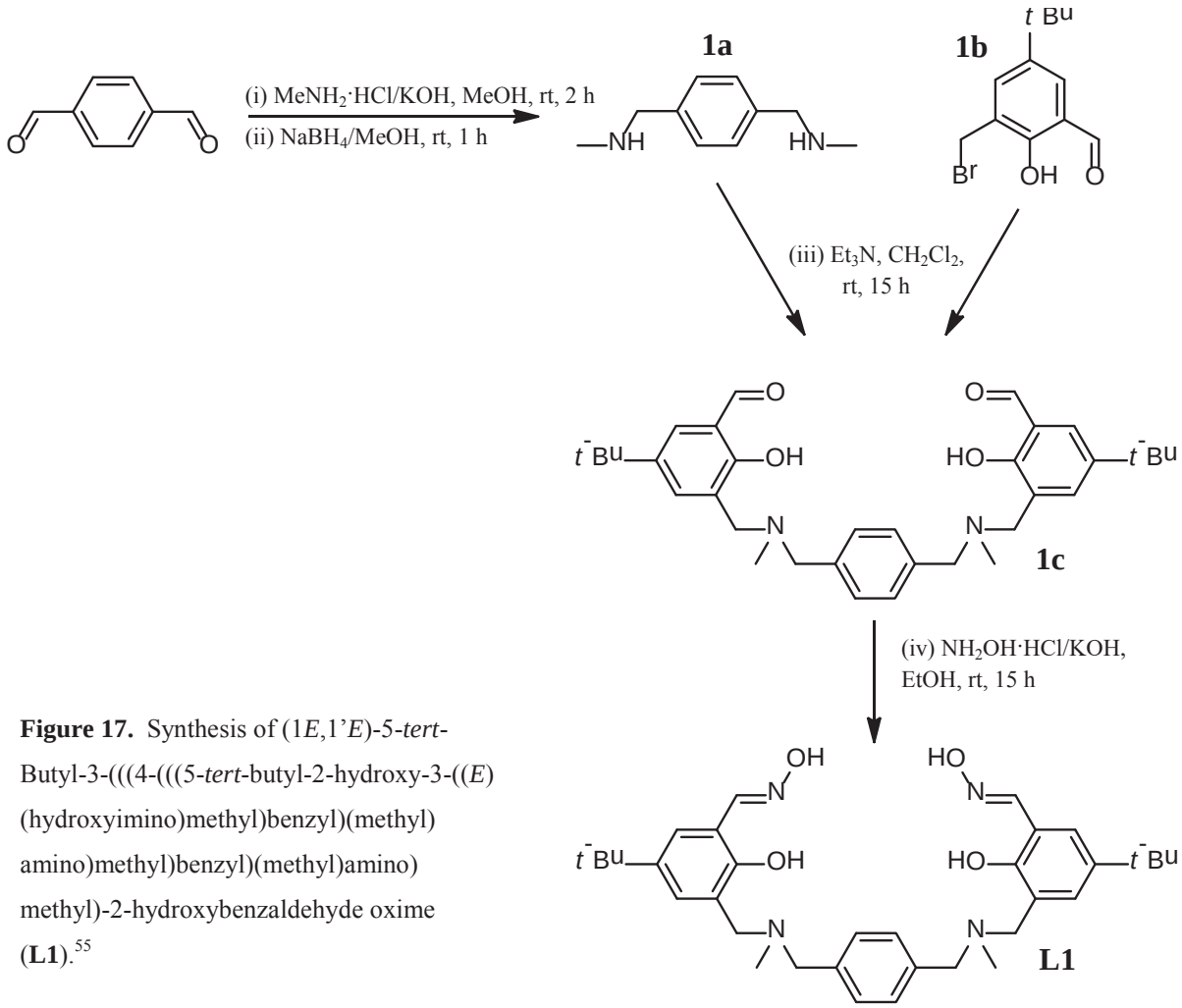

Figure 17. Synthesis of (1*E*,1'*E*)-5-*tert*-Butyl-3-(((4-(((5-*tert*-butyl-2-hydroxy-3-((*E*)(hydroxyimino)methyl)benzyl)(methyl)amino)methyl)benzyl)(methyl)amino)methyl)-2-hydroxybenzaldehyde oxime (**L1**).[55]

The dinuclear manganese complex was synthesised by reacting **1c** with manganese perchlorate and sodium methoxide in a 1:2:2 ratio, using acetonitrile as the solvent. The crystals of the dinuclear manganese complex were formed via slow diffusion of diethyl ether into an acetonitrile solution containing the complex.[53] To determine if hydrolysis of the oxime was occurring, the dinuclear complex was remade. After all reagents were combined, Electrospray Ionisation Mass Spectroscopy (ESMS) was taken at one and two hour intervals

and an overnight period. Two more samples were then taken two hours apart after the solution was heated to approximately 50°C. The ESMS results suggested that hydrolysis increased as the reaction time increased.[53]

Willoughby made suggestions as to how to isolate and concentrate the complex. Firstly, by using the same reaction conditions but prolonging reaction time may allow more time for the hydrolysis. Secondly, by first synthesising the partially oximated ligand directly before attempting complexation to synthesise the dinuclear complex.[53]

1.8 Objectives

The present study has two primary objectives. Firstly, to model the di-nuclear manganese complex in order to investigate the relationship between the Jahn-Teller distortions and the coupling of the manganese centres. This will involve modelling both the ferromagnetic and antiferromagnetic states and investigating the structure and molecular orbitals of the lowest energy state. DFT calculations will be performed using an unrestricted B3LYP functional with 6-31+G(d,p) basis sets for the C, H, N and O atoms and LANL2DZ basis sets for the Mn atoms. The broken symmetry approach will be used to model the antiferromagnetic state and the exchange coupling constant will be calculated. The bond lengths and molecular orbitals will be compared to provide evidence for Jahn-Teller effects. Secondly, to re-synthesise the dinuclear manganese complex in suitable quantity and quality to fully investigate its structural and magnetic properties. The planned structural and magnetic characterisation included X-ray crystallographic analysis, elemental analysis, magnetics and electron paramagnetic resonance (EPR).

1.9 Hypothesis

The dinuclear manganese complex serendipitously synthesised by Willoughby exhibits both Jahn-Teller compression and elongation. The distortions are parallel to each other, perpendicular to the bridging plane. The complex will be antiferromagnetic due to the orientation of the distortions.

Chapter Two: The di-manganese complex

2.1 Closer analysis of the structure

The X-ray crystallographic analysis of the dinuclear complex synthesised by Willoughby featured two manganese centres in the +3 oxidation state. Mn(1) was in an elongated octahedral coordination environment, with two phenolates and two bridging oxygens in the equatorial positions and two carbonyl oxygens in the axial positions. Mn(2) was in a compressed octahedral coordination environment, with two oximes and two bridging oxygens in the equatorial positions and two phenolates in the axial positions.

The data for the X-ray structural determination of Willoughby's dinuclear complex was not of sufficient quality for all of the protonated sites to be determined. In particular, the X-ray crystallographic analysis does not show if there were any hydrogens attached to the bridging oxygens in the complex or on the amine nitrogen atoms. It was possible to determine the bridging oxygens and amines were protonated by examining the results of the X-ray crystallographic analysis together with the CHN analysis, and keeping in mind the charge balance of the complex (see 2.4).

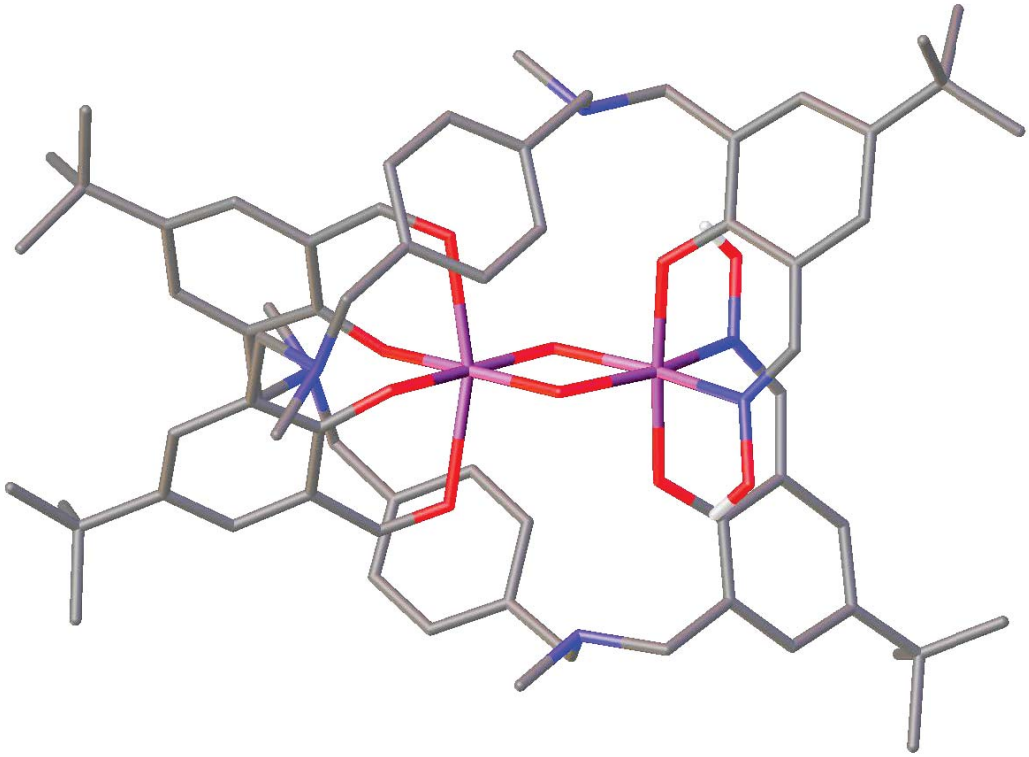

Figure 18. X-ray crystallographic structure of the dinuclear manganese complex, with non-essential hydrogens omitted for clarity.

2.2 Bond Lengths

Searches for crystallographic structures containing the same primary coordination sphere as the dinuclear manganese complex were conducted using the Cambridge Structural Database.[56] These were characterised by three distinct motifs (Figure 19).

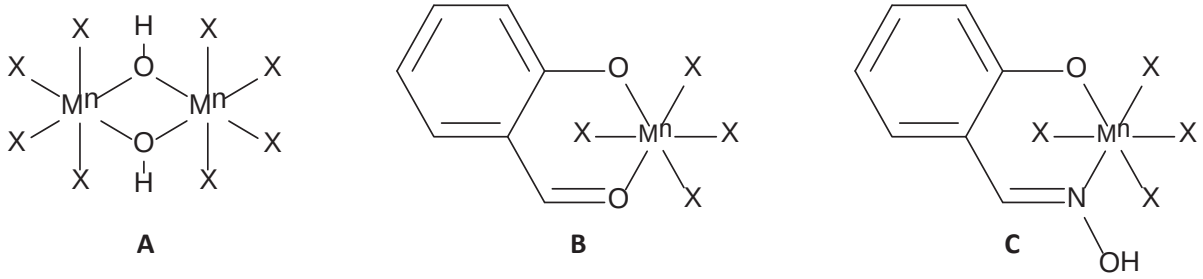

Figure 19. Motifs searched for in the Cambridge Structural Database.

Any structures which did not have manganese in the +3 oxidation state were excluded from each search. Any structures with motif **A** which contained other atoms bonded to the hydroxyl groups were also excluded. Specific bond lengths of each of the motifs in the searched structures were compared with the bond lengths of the dinuclear manganese complex determined by X-ray crystallographic analysis (Table 4).

There were four structures which contained motif **A**, but one of these did not give the bond lengths in the database or in the associated literature. The Mn-O bond lengths of the remaining three structures were determined and the range of these bond lengths is given in table 4. There were 22 compounds which contained motif **B** and the range of phenolate Mn-O and aldehyde Mn-O bond lengths are given in table 4. There were nine structures identified to contain motif **C** and the range of phenolate Mn-O and oxime Mn-N bond lengths are given in table 4. All of the experimental bond lengths measure from the Willoughby structure fell within the range of the comparable bond lengths found in the literature. In particular, it is of note that the bridging oxygen Mn-O bond lengths were consistent with hydroxyl Mn-O bond lengths in the database. For example, the oxo (O^{2-}) Mn^{III}-O bond lengths in the database spanned the range 1.815 – 1.866 Å and the Mn-O bond lengths for the dinuclear manganese complex of Willoughby did not fall in this range. This gave strong evidence that the bridging oxygens were protonated.

Table 4. Comparison of di-manganese complex bond lengths determined by X-ray crystallographic analysis with bond lengths of compounds in the Cambridge Structural Database containing the same motifs.

Motif	Atoms	Type of coordination bond	Willoughby structure bond length (Å)	Range of bond lengths in literature (Å)[56]
A	Mn1-O100 (hydroxyl)	equatorial	1.913(4)	1.826 – 2.126
	Mn1-O101 (hydroxyl)	equatorial	1.917(4)	1.826 – 2.126
	Mn2-O100 (hydroxyl)	equatorial	2.085(5)	1.826 – 2.126
	Mn2-O101 (hydroxyl)	equatorial	2.079(4)	1.826 – 2.126
B	Mn1-O11 (phenolate)	equatorial	1.926(4)	1.807 – 1.948
	Mn1-O12 (phenolate)	equatorial	1.943(4)	1.807 – 1.948
	Mn1-O212 (aldehyde)	axial	2.281(5)	1.854 – 2.285
	Mn1-O222 (aldehyde)	axial	2.258(4)	1.854 – 2.285
C	Mn2-O13 (phenolate)	axial	1.882(5)	1.867 – 1.989
	Mn2-O14 (phenolate)	axial	1.893(5)	1.867 – 1.989
	Mn2-N232 (oxime)	equatorial	2.094(6)	2.042 – 2.291
	Mn2-N242 (oxime)	equatorial	2.096(7)	2.042 – 2.291

2.3 Elemental Analysis

Elemental analysis is a common form of composition analysis used to determine the percentage of carbon, hydrogen and nitrogen in a sample. The analysis is carried out in a CHN analyser, where the sample is fully combusted and the amounts of gaseous products are measured and related to the initial mass.[9] An accurately weighed mass of sample is placed in a sealed capsule and passed into a pyrolysis tube. The sample is heated at approximately 900 °C in a pure O_2 atmosphere, where the oxidation of carbon, hydrogen and nitrogen produces CO_2, H_2O and nitrogen oxides. The nitrogen oxides are then reduced to N_2, excess O_2 is removed, and the mixture of CO_2, H_2O and N_2 are separated using a specialised type of gas chromatography called frontal chromatography. The gases are detected using a thermal conductivity detector and the mass percentages of C, H and N are recorded to within an accuracy of $< 0.3\%$.[9] The estimated composition of the di-manganese complex based on the X-ray crystallographic structure is presented in Table 5.

Table 5. Estimated composition of di-manganese complex as based on analysis of Willoughby's structure.

Composition	C	H	N	O	Cl	Mn
2 x Mn	0	0	0	0	0	2
2 x L2	68	90	6	8	0	0
2 x OH	0	2	0	2	0	0
3 x ClO_4^-	0	0	0	12	3	0
Total	68	92	6	22	3	2
Mass percentage	**52.30%**	**5.94%**	**5.38%**	**22.54%**	**6.81%**	**7.04%**

CHN analysis was carried out on the crystals synthesised by Amy Willoughby.[53] The results of this analysis are presented in Table 6. The mass percentages of carbon and nitrogen differ significantly from the estimated composition.

Table 6. CHN analysis of AW crystals.

%C	%H	%N
46.80	5.67	4.54

Table 7 depicts further examination of the CHN analysis results. The difference between the estimated and experimentally determined CHN compositions can be attributed to the presence of four water molecules for every di-manganese molecule, as well as a fourth perchlorate ion being present in the crystal structure. The presence of the water molecules suggests that the sample sent for CHN analysis was not dry when analysed. Overall, the CHN analysis was consistent with the di-manganese structure determined by X-ray crystallographic analysis.

Table 7. Estimated composition of di-manganese complex.

Composition	C	H	N	O	Cl	Mn
2 x Mn	0	0	0	0	0	2
2 x L2	68	90	6	8	0	0
2 x OH	0	2	0	2	0	0
4 x ClO_4^-	0	0	0	16	4	0
4 x H_2O	0	8	0	4	0	0
Total	68	100	6	30	4	2
Mass percentage	**47.12%**	**5.82%**	**4.85%**	**27.69%**	**8.18%**	**6.34%**

2.4 Charge balance

The results of the X-ray crystallographic analysis and CHN analysis could be used in conjunction with the concept of charge balance in order to determine the whether the bridging oxo oxygens of the dinuclear manganese complex were protonated. The overall charge of the complex plus any counter ions should equal zero. It was assumed that the amines and oximes were protonated, while the phenolates were deprotonated. CHN analysis suggested that there were four perchlorate counter ions present in the crystal structure, rather than the three that were determined by X-ray crystallographic analysis.

Table 8. Balance of charges for the dinuclear complex.

Group	**Charge**
2 x Mn^{3+}	+ 6
4 x phenolate donors	- 4
4 x ammonium groups	+ 4
4 x ClO_4^- counter ions	- 4
2 x OH^- (bridging)	- 2
Total	**0**

Based on the balance of charges presented in Table 8, X-ray analysis and elemental analysis it appears that the bridging oxygens were protonated. Therefore the bridging ligands of the di-manganese complex were assigned as hydroxo ligands.

2.5 Similar structure search

Searches for manganese dimers with certain motifs were completed on the Cambridge Structural Database. Any dimers which contained manganese ions that were not specified as being in the +3 oxidation state or contained any additional metal ions were excluded from each search.

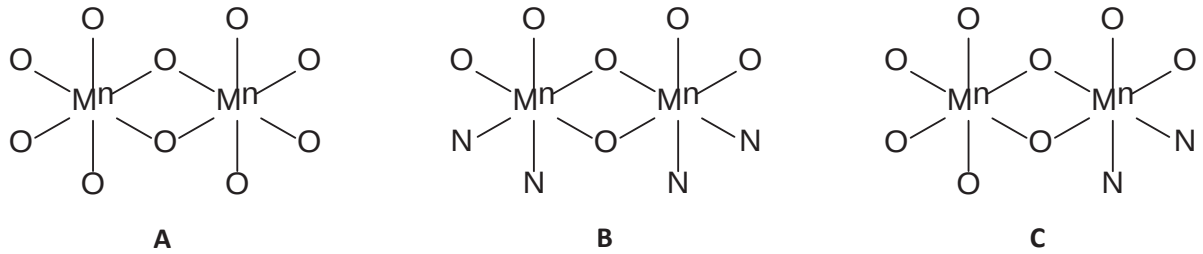

Figure 20. Motifs searched for in the Cambridge Structural Database.

The first search conducted was for motif A; Mn(III) dimers with an oxygen-containing bridge where each Mn(III) was hexa-coordinated by six oxygens (Figure 20). Eight crystallographic structures containing motif A were identified. Five of these structures had elongation distortions parallel to each other and perpendicular to the bridging plane of the complex. Two other structures had elongation distortions in a parallel orientation in the bridging plane. The remaining structure had both manganese ions in a compressed coordination environment, with the distortions in a parallel orientation in the bridging plane. None contained both elongation and compression in the same molecule.

Manganese dimers containing motif B were then investigated. These dimers had an oxygen-containing bridge where each Mn(III) was hexa-coordinated by four oxygens and two nitrogens (Figure 20). 63 crystallographic structures containing motif B were identified, 58 of which had three-dimensional coordinates in the database. Approximately 81% of these structures had elongation distortions in a parallel orientation and in the bridging plane of the complex, 7% had elongation distortions in a parallel orientation and perpendicular to the bridging plane and 3% had elongation distortions in a perpendicular orientation. 5% had distorted octahedral coordination environments at each manganese centre, but the distortions were not consistent with elongation or compression. The two remaining structures were identified in the literature as having both manganese centres elongated with the axial bonds (in the bridging plane) longer than the equatorial ones.[57] However, this was not consistent with the bond lengths in the crystallographic structures (Figure 21). The crystallographic structure of complex 1 appeared to be consistent with compression distortions in a parallel orientation and perpendicular to the bridging plane. The distortions at the manganese centres of complex 2 are difficult to identify from the crystallographic structures, but are not consistent with Jahn-Teller elongation as the two axial bonds are not longer than all four equatorial bonds at each centre.

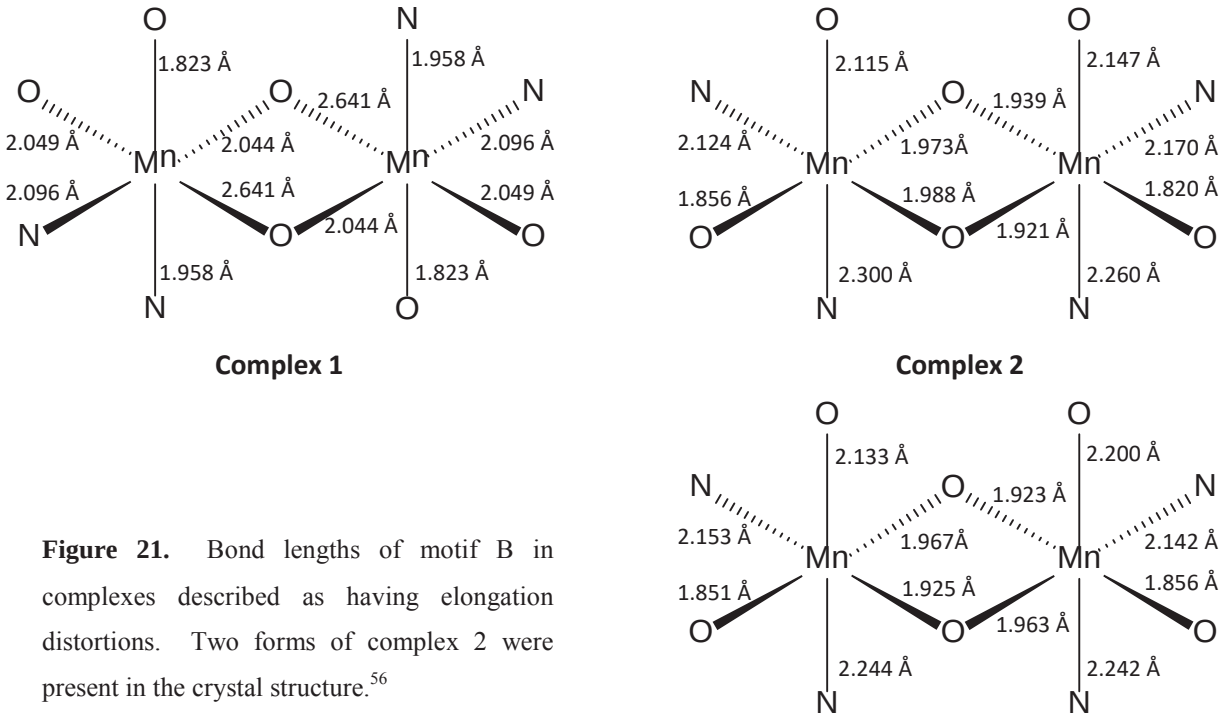

Figure 21. Bond lengths of motif B in complexes described as having elongation distortions. Two forms of complex 2 were present in the crystal structure.[56]

The axial elongated bonds were both Mn-O bonds for most (~89%) of the motif B structures with elongation distortions. For both motif A and B searches, the axial elongated Mn-O bonds fell in a range of 2.002 – 2.813 Å. The range of bond lengths for axial elongated Mn-N bonds was 2.189 – 2.286 Å.

A search was then conducted for motif C; Mn(III) dimers with an oxygen-containing bridge where one Mn(III) was hexa-coordinated by six oxygens and one Mn(III) was hexa-coordinated by four oxygens and two nitrogens (Figure 20). No structures were identified containing this motif.

Based on the search of crystallographic structures similar to that of the dinuclear complex, several conclusions can be made. Firstly, elongation distortions are much more common in manganese dimers containing motifs A and B. Secondly, there are no reported manganese dimers containing motifs A, B or C with both elongation and compression distortions in the same complex. Thirdly, there is no reported crystallographic structure with motif C, which the dinuclear complex contains. This may be due to the lowered symmetry of motif C. Finally, the identification of Jahn-Teller elongation and compression cannot be clearly identified when only looking at the geometric data of a crystallographically determined structure of a complex. Some papers have identified the distortions of the manganese octahedral environments as elongation, when they are clearly open to interpretation.

2.6 Summary

The analysis of the incomplete data from Willoughby gives strong evidence that this complex is a di-manganese(III) complex containing two ligands and two bridging hydroxo groups. The ligands are not symmetric, with one aldehyde and one oxime at each end. There is no similar reported crystallographic structure of a Mn(III) dimer with an oxygen-containing bridge where one Mn(III) was hexa-coordinated by six oxygens and one Mn(III) was hexa-coordinated by four oxygens and two nitrogens. Each of the Mn(III) ions are distorted, with Mn(1) in a elongated octahedral environment and Mn(2) in a compressed octahedral environment. There are no similar structures in the Cambridge Structural Database containing both of these distortions.

Chapter 3: Computational analysis

3.1 Introduction

Computational analysis was undertaken to model the di-nuclear manganese complex in order to investigate the Jahn-Teller distortions and the coupling of the manganese centres.

A di-manganese complex may be ferromagnetic or antiferromagnetic due to the alignment of the unpaired spins on the two manganese ions. When modelling a manganese dimer, both the ferromagnetic and antiferromagnetic states should be modelled and the energies of the two structures compared. The corresponding ferromagnetic and antiferromagnetic structures of manganese dimers in the literature tend to be very similar.[50] However, there are usually differences in the energies of the two structures.[7, 49-50] The broken symmetry approach, developed by Noodleman *et al.*, is a method commonly used to calculate antiferromagnetic spin states. The broken symmetry method removes the symmetry elements connecting the two metal centres and imposes an asymmetry in the starting spin density.[43]

3.2 Discussion of method

3.2.1 Overview

The manganese ions were both Mn(III) and were assumed to be high-spin due to the Jahn-Teller distortions present in the structure determined by X-ray crystallographic analysis. The Jahn-Teller effect is ubiquitous for high-spin d^4 ions such as Mn^{3+} but significantly less common for low-spin d^4 complexes.[14]

The ferromagnetic state was much simpler to model computationally than the antiferromagnetic state. The ferromagnetic state was first optimised, before using this optimised structure as an initial guess for the antiferromagnetic state (approximated by the broken symmetry state).

The following procedure was adhered to for each structure that was modelled. First, the geometry of the structure was optimised. *Stable=opt* was then used to ensure that the wavefunction of the optimised geometry was stable and re-optimisation of the structure was

automatically executed if an instability was found. A frequency calculation was then performed to verify if the optimised geometry was at a minimum point with no imaginary frequencies.

The complex cation was built in GaussView 5.0, rather than the initial geometry being taken from the X-ray crystal structure. This was done to confirm that the structure obtained by X-ray crystallographic analysis, with both Jahn-Teller elongation and compression, was the optimum geometry for this complex. A number of changes were made to the experimentally determined structure. The four perchlorate counter anions were excluded. The *tert*-butyl groups were replaced with methyl groups to simplify the structure, and hence simplify the calculations. Hydrogen atoms were added to each of the amines and to the bridging oxygens (to form hydroxo bridging ligands). This was done as the X-ray crystallographic analysis was not of sufficient quality to show these hydrogens were present but charge balance suggested they should be. DFT calculations were performed using an unrestricted B3LYP functional with 6-31+G(d,p) basis sets for the C, H, N and O atoms and LANL2DZ basis sets for the Mn atoms. Calculations were completed using Gaussian 09 revision D.01.

The first set of calculations were performed with a spin multiplicity of nine in order to model the ferromagnetically coupled complex. The spin multiplicity for a molecule is given by the equation $2S+1$ where S is the total spin.[58] In the ferromagnetic state the four *d*-electrons of each Mn^{3+} ion would be in the α spin-state. The eight unpaired electrons would result in a total spin of $8 \times \frac{1}{2} = 4$. The spin multiplicity would then be $2S+1 = 9$ (nonet).

Calculations were then performed with the spin multiplicity of one in order to model the antiferromagnetically coupled complex. In the antiferromagnetic state the four *d*-electrons of one Mn^{3+} ion would in the α spin-state, and the *d*-electrons of the other Mn^{3+} ion would be in the β spin-state. This would result in zero net spin. The spin multiplicity would then be $2S+1 = 1$ (singlet).

The value of $\langle S^2 \rangle$ (spin-squared operator) was monitored throughout each of the calculations in order to ensure that the calculated system had the correct spin distribution. The generalised spin-squared operator equation for the spin of a multi-electron system is as follows:[37]

$$\hat{\mathbf{S}}^2\boldsymbol{\Psi} = S(S+1)\hbar^2\boldsymbol{\Psi} \quad (8)$$

Based on this equation, the eigenvalue of $\langle S^2 \rangle$ for a nonet spin state would be 4(4+1) = 20. For a singlet spin state the eigenvalue of $\langle S^2 \rangle$ would be 0(0+1) = 0. This value was printed in the output after each SCF cycle. The ferromagnetic calculation was monitored to ensure that the value of $\langle S^2 \rangle$ was approximately 20.

If the value of $\langle S^2 \rangle$ is significantly greater than *S*(*S*+1), it is common practice to consider the calculation to be "badly spin contaminated".[59] However, for the broken symmetry state, used to model the antiferromagnetic state, it is required that the value of $\langle S^2 \rangle$ is much greater than the correct value. This higher value of $\langle S^2 \rangle$ represents the "variational adjustment of neutral and ionic components" that is required for the correct result to be achieved.[59] The expectation value for the S^2 operator over the broken symmetry state is given by the following equation:[60]

$$\langle \hat{S}^2 \rangle_{BS} = \left(\frac{N^\alpha - N^\beta}{2}\right)\left(\frac{N^\alpha - N^\beta}{2} + 1\right) + N^\beta - \sum_i n_i^\alpha n_i^\beta \left|S_{ii}^{\alpha\beta}\right|^2 \quad (9)$$

where N^α and N^β are the number of α and β electrons, n_i^α and n_i^β are the spin–orbital occupation numbers. For the broken symmetry state approximating the antiferromagnetic singlet of the di-manganese complex, the number of α and β electrons should be equal. If the overlap integrals between the spin-up and spin-down orbitals are zero, the expectation value for the spin-squared operator for the broken symmetry state becomes $\langle \hat{S} \rangle_{BS} = N^\beta$. Therefore for the broken symmetry state of the di-manganese complex, the value of $\langle S^2 \rangle$ should be approximately four, as this was the number of unpaired electrons at one Mn(III) centre.

The molecular orbitals were investigated using Chemcraft software, a graphical program which is useful for visualising the computed results of chemistry calculations.[61] The program renders three-dimensional pictures of molecules and can be used to view the molecular orbitals.

The spin density plot was constructed by first generating a cube file from the data in the formatted checkpoint file. A cube file contains volumetric data, which are the X-, Y-, and Z-coordinates that are mapped on to a 3D grid, and atom positions. The cube file was loaded into GaussView 5.0 for visualisation of the spin density plot.

3.2.2 Ferromagnetic (nonet)

Job 1: Optimisation of the nonet

The initial geometry optimisation for the dinuclear manganese complex in the ferromagnetic state was performed with the multiplicity set to nine and the charge set to (+) four. The optimisation read in a permutation of orbitals in the initial guess and the initial connectivities were obtained from the complex built in GaussView 5.0. An ultrafine integration grid was used and the integral accuracy was increased by one order of magnitude compared to the default. Full integral accuracy was used throughout the calculation. A quadratic convergence was allowed using *SCF=XQC* and the limit on conventional SCF cycles during *SCF=XQC* was set to 40 cycles.

The optimisation completed successfully, with the maximum force, RMS force, Maximum displacement and RMS placement all smaller than the default thresholds, indicating that they had converged. The optimisation went through 76 geometry iterations. The spin-squared operator for the optimised structure was 20.1128. This was consistent with the expected value of 20 for the ferromagnetically coupled manganese centres.

Job 2: *Stable=opt*

Stable=opt was then used to check the stability of the wavefunction at the optimised geometry. Specifying "opt" ensured that if an instability was found, the wavefunction would be re-optimised with the appropriate reduction in constraints until a stable wavefunction was found. The output indicated that the wavefunction of the optimised geometry was stable under the perturbations considered.

Job 3: Frequency

A frequency calculation was then performed to determine if the optimised geometry was at an energetic minimum. A frequency calculation computes force constants and vibrational frequencies. The vibrational frequencies were computed by determining the second derivatives of the energy with respect to the nuclear positions.[37]

Only two of the four convergence checks were smaller than the indicated thresholds. The other two were within one order of magnitude. However, the default thresholds in Gaussian are designed for much simpler organic molecules rather than the large inorganic molecule

being investigated.[62] The frequency calculation showed no imaginary (negative) frequencies for the optimised ferromagnetic di-manganese complex. This indicated that the optimised ferromagnetic dinuclear complex had converged on an energetic minimum and no further optimisations of the ferromagnetic di-manganese complex needed to be completed.[62]

3.2.3 Antiferromagnetic (singlet)

Job 1: *Guess=read*

The first calculation for modelling the antiferromagnetically coupled dinuclear complex was performed using the optimised geometry from the first nonet calculation as an initial guess and extracting the force constants from the checkpoint file. If the calculation had been started from a structure built in GaussView 5.0, as for the nonet optimisation, it would have converged on a closed-shell singlet consistent with low-spin Mn(III) rather than a singlet consistent with two antiferromagnetically coupled high spin Mn(III).[63] *Guess=read* ensured that the calculation used the orbitals converged for the ferromagnetic state as an initial guess. If this had not been included, the standard run would have given a crude guess which seldom works for complicated systems such as broken symmetry states.[63] The initial guess gave a value of $\langle S^2 \rangle$ of 2.7980. The geometry optimisation completed with all four convergence checks under the indicated thresholds. After 30 geometry iterations the final $\langle S^2 \rangle$ value was 2.0380. Therefore this calculation did not give the desired broken symmetry state based on the expected value of $\langle S^2 \rangle = 4$.

Job 2: *Guess=mix*

A single point calculation was then performed to see if *guess=mix* would help to give the desired spin state, again using the nonet checkpoint file for the initial geometry. *Guess=mix* caused the calculation to mix the HOMO and LUMO such that the α-β and spatial symmetries are destroyed. At the conclusion of the calculation $\langle S^2 \rangle$ was 2.0752, which was too low for the desired broken symmetry state.

Job 3: Fragment guess

Using the first optimised nonet structure in Gaussview 05, six fragments were defined using the atoms group editor. The selected fragments are shown in Figure 22. Note in this image

and all subsequent images of this complex cation Mn(1) is the metal centre on the left and Mn(2) is the metal centre on the right. The six fragments were defined as: Mn(1), Mn(2), ligand 1, ligand 2, hydroxyl 1 and hydroxyl 2.

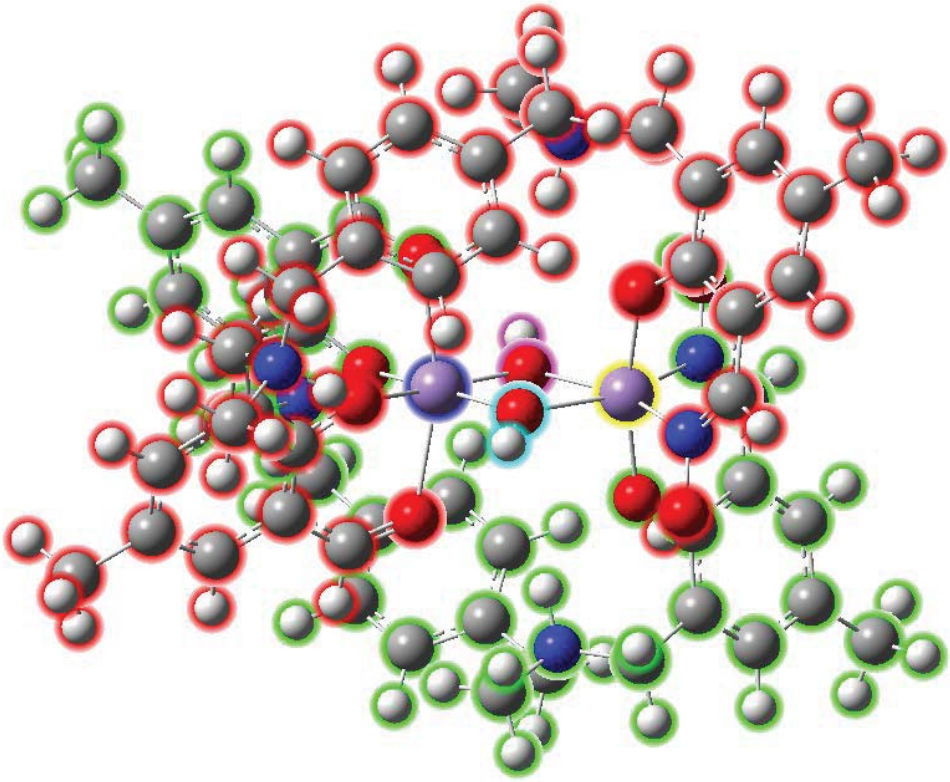

Figure 22. Fragments of the dinuclear manganese complex defined using the atoms group editor in Gaussview 5.0.

Charges of -1 were assigned to each hydroxyl fragment, +3 to each manganese fragment and each ligand fragment had a neutral charge. Each of the manganese fragments were specified to be a quintets as they contained four unpaired electrons. The other fragments were each singlets as they contained no unpaired electrons. The hydroxyl fragments, ligand fragments and Mn(1) fragment were defined as having α spin, the Mn(2) fragment was defined as having β spin. This forced the manganese atoms of the dinuclear complex to have opposite spins.

A fragment guess calculation was then set up. The overall spin multiplicity was set to one and the charge was set to (+) four. The fragment charges, multiplicities and connectivities were obtained from the structure with assigned fragments in Figure 22 using the Gaussian

calculation setup. *Guess=(fragment=6, only)* was included in the input file in order to generate a guess from fragment guess orbitals. The calculation completed successfully.

Job 4: Optimisation of the broken symmetry state

The fragment guess job did not ensure that the geometry of the dinuclear complex in the broken symmetry state was of the minimum energy. Hence an optimisation was completed using the fragment guess calculation as an initial guess. The first attempt at optimising the broken symmetry state removed all orbital symmetry constraints. This attempt resulted in a convergence failure. An ultrafine integration grid was then used and a quadratic convergence was allowed. This optimisation completed successfully. All four of the convergence checks were under the default thresholds, indicating that they had converged. The optimisation went through 31 geometry iterations. The value of $\langle S^2 \rangle$ was 4.0989, which was consistent with the expected value of $\langle S^2 \rangle = 4$ for the broken symmetry state.

Job 5: *Stable=opt*

Stable=opt was then used to check the stability of the resulting wavefunction of the optimised broken symmetry state. The output indicated that the wavefunction of the broken symmetry state calculated by optimisation was stable under the perturbations considered.

Job 6: Frequency

A frequency calculation was then performed to determine if the optimised geometry was at an energetic minimum. Only two of the four convergence checks were smaller than the indicated thresholds. The other two were within one order of magnitude. There was one negative frequency in the output (-8.2615 cm^{-1}). This frequency can be overlooked as it is relatively small and on a molecule of this size it can be considered within the uncertainty of the calculation.[62] Overall, the frequency calculation indicated that the optimisation of the broken symmetry state of the dinuclear manganese complex was acceptable and no further optimisations of the broken symmetry state needed to be completed.

3.3 Results and discussion

3.3.1 Ferromagnetic (nonet)

The optimised geometry of the ferromagnetic dinuclear manganese complex is given in Figure 23. The optimised structure shows elongation at Mn(1) and compression at Mn(2), which is consistent with the structure obtained by X-ray crystallography. The energy of the optimised geometry was -3462.6528 Hartrees (-9091195 kJ mol^{-1}). The spin-squared operator was 20.1128, which was consistent with ferromagnetic coupling between the manganese centres. The optimisation job took 427 hours to complete and the frequency job took 369 hours to complete. The large amount of time required was a disadvantage of using the 6-31+G(d,p) basis sets for the C, H, N and O atoms and LANL2DZ basis sets for the Mn atoms.

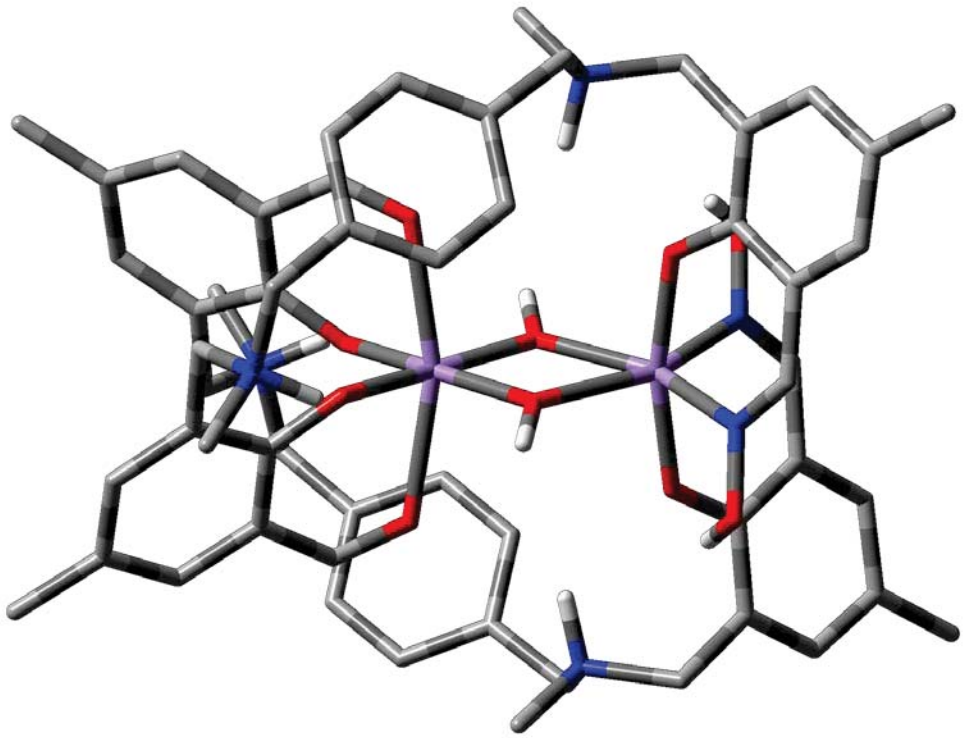

Figure 23. Computationally optimised structure of the di-manganese complex, with non-essential hydrogens removed for clarity.

Figure 24 gives a comparison between the structure obtained by X-ray crystallography and the computationally optimised structure of the ferromagnetic dinuclear complex. The general structural features of the experimental X-ray crystal structure are mirrored in the calculated structure, although the bond lengths and bond angles are slightly outside the range for an identical structure.

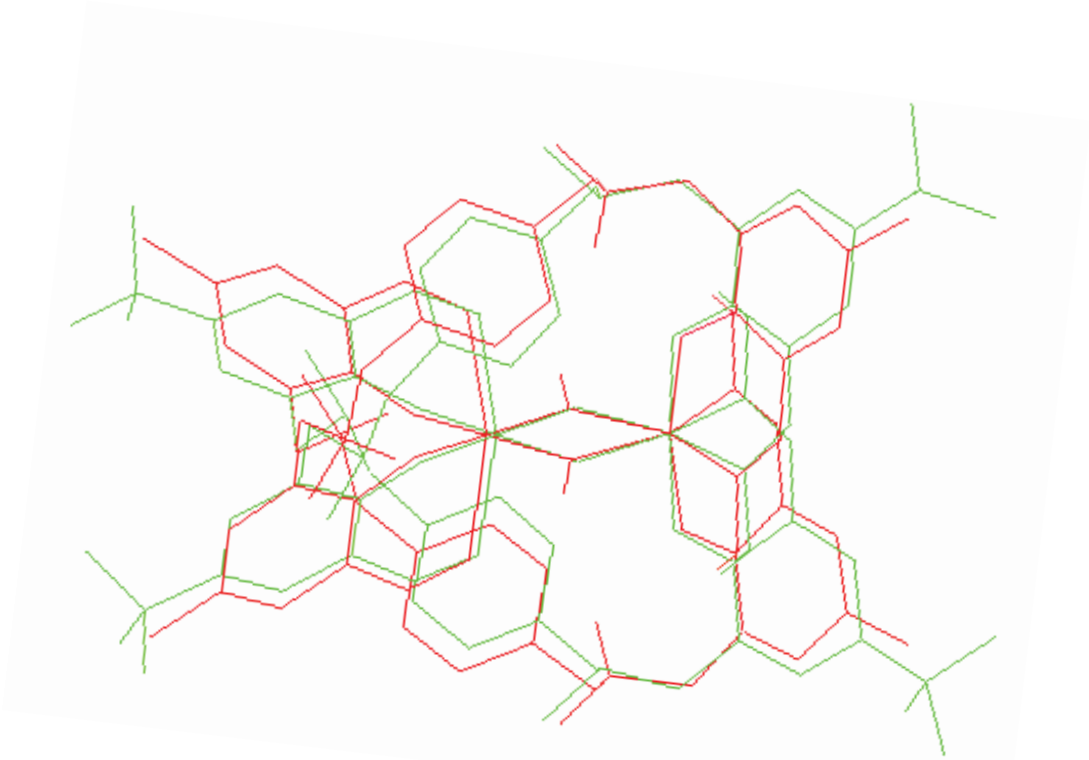

Figure 24. Superposition of the geometries of the X-ray crystallographic structure (green) and the computed ferromagnetic state (red) of the dinuclear complex.

From the comparison of the computationally optimised ferromagnetic di-manganese complex and the X-ray crystallographic structure it was concluded that the ferromagnetic dinuclear manganese complex was successfully modelled.

3.3.2 Antiferromagnetic (singlet)

The optimised geometry of the antiferromagnetic dinuclear manganese complex is given in Figure 25. The optimised structure shows elongation at Mn(1) and compression at Mn(2), which is consistent with the structure obtained by X-ray crystallography and the computed structure for the ferromagnetic complex. The energy of the optimised geometry was -3462.6514 Hartrees (-9091191 kJ mol^{-1}). The spin-squared operator was 4.0989, which was consistent with the desired broken symmetry state, with four α *d*-electrons at Mn(1) and four β *d*-electrons at Mn(2). The optimisation job took 119 hours to complete and the frequency job took 519 hours to complete. The large amount of time required was a disadvantage of using the 6-31+G(d,p) basis sets for the C, H, N and O atoms and LANL2DZ basis sets for the Mn atoms.

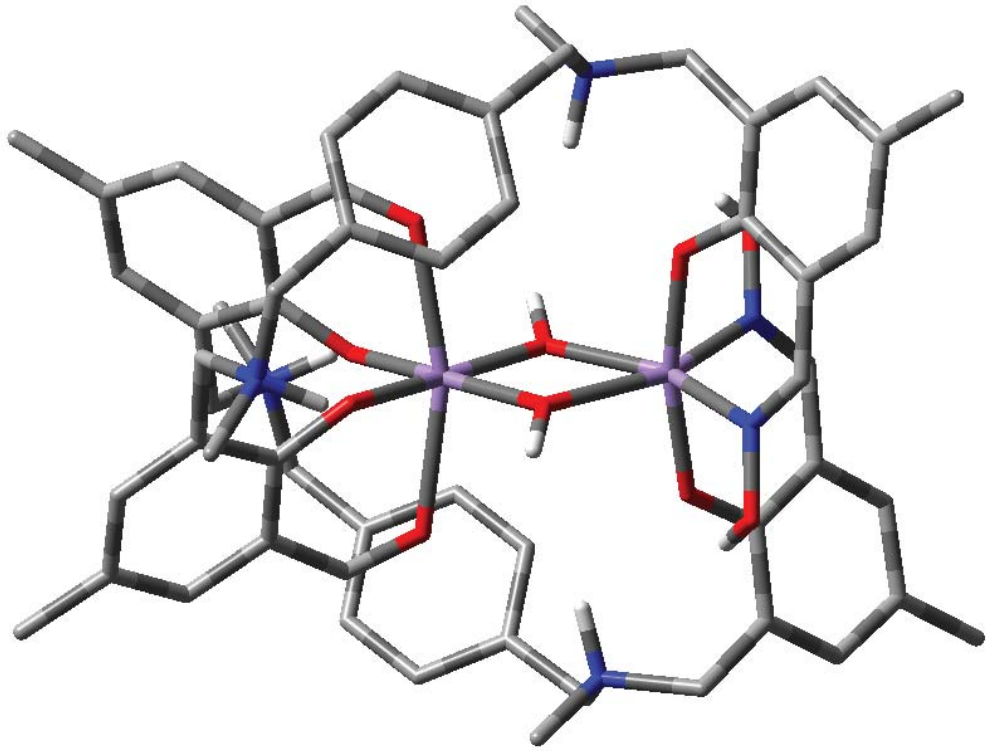

Figure 25. Optimised geometry of the antiferromagnetic (broken symmetry) di-manganese complex, with non-essential hydrogens removed for clarity.

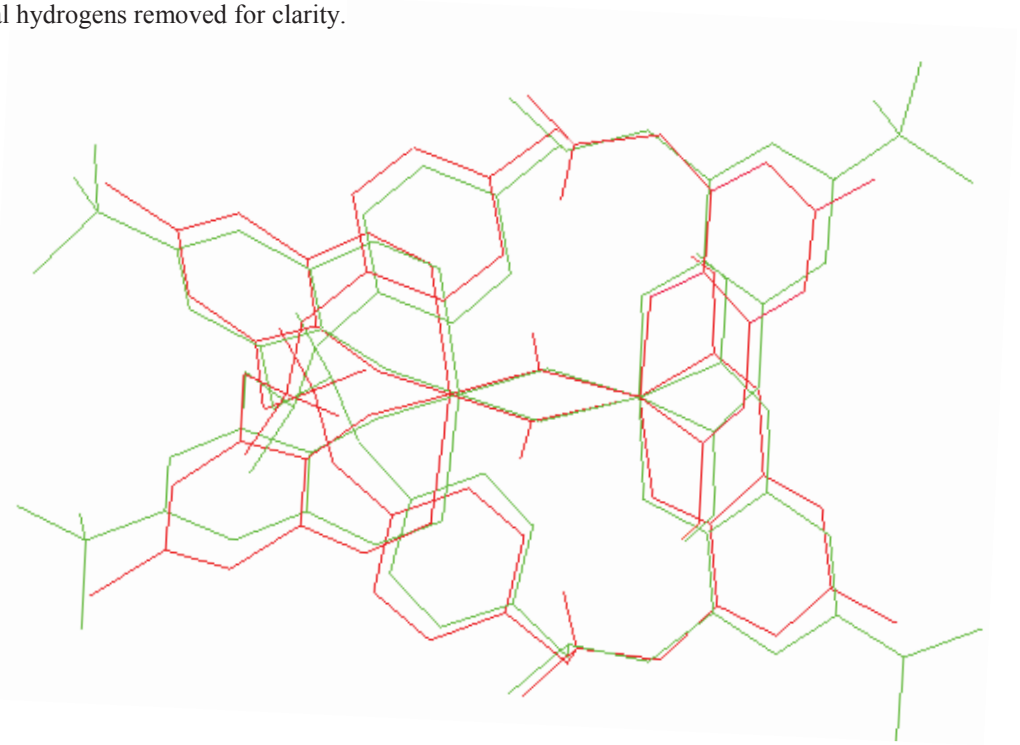

Figure 26. Superposition of the geometries of the X-ray crystallographic structure (green) and the computed broken symmetry state (red) of the dinuclear complex.

Figure 26 gives a comparison between the structure obtained by X-ray crystallography and the computationally optimised structure of the antiferromagnetic dinuclear complex. The general structural features of the experimental X-ray crystal structure are mirrored in the

calculated structure, although the bond lengths and bond angles are slightly outside the range for an identical structure.

From the comparison of the computationally optimised broken symmetry state and the X-ray crystallographic structure, as well as the value of the spin squared operator, it was concluded that the antiferromagnetic dinuclear manganese complex was successfully modelled.

3.3.3 Comparison of calculated structures

The calculations performed to model the dinuclear manganese complex are summarised in table 9.

Table 9. Summary of calculations performed for the dinuclear manganese complex.

State	Calculation	Total Spin	Energy (Hartrees)	Desired state achieved?	Stable?	Imaginary frequencies
Ferromagnetic	optimisation	20.1128	**-3462.65281406**	yes	yes	0
Broken Symmetry	guess=read	2.0380	-3462.60916348	no	-	-
Broken Symmetry	guess=mix singlepoint	2.0752	-3462.53535490	no	-	-
Broken Symmetry	fragment guess	4.0985	-3462.65124412	yes	yes	-
Broken Symmetry	fragment optimisation	4.0989	-3462.65135966	yes	yes	1

The energies of the computationally optimised ferromagnetic and antiferromagnetic complexes were compared to determine the most energetically favourable structure of the dinuclear complex. The ferromagnetic di-manganese complex was lower in energy than the antiferromagnetic (broken symmetry) di-manganese complex by 1.46×10^{-3} Hartrees (3.82 kJ mol^{-1}). This suggested that ferromagnetic coupling between the two manganese centres was more energetically favourable, with the 4 *d*-electrons at each Mn centre in the α spin-state, in contrast to the hypothesis that the complex would be antiferromagnetic. In the following sections, only the ferromagnetic di-manganese complex will be further investigated.

The energy difference between the antiferromagnetic and ferromagnetic structures was close to kT at room temperature (2.48 kJ mol^{-1}) which suggests that the ferromagnetic and antiferromagnetic structures will both be present at room temperature in approximately an 8:2 ratio. At lower temperatures the ferromagnetic structure will dominate. Due to the small difference in the energies of the calculated structures, if a different functional or basis set was used the results may differ.

The energy difference between the two structures was used to calculate the value of the exchange coupling using the equation proposed by Yamaguchi.[47b]

$E_{HS} - E_{BS} = -1.455 \text{ x } 10^{-3}$ Hartrees
$E_{HS} - E_{BS} = -319.3355866 \text{ cm}^{-1}$

$$J = -\frac{E_{HS} - E_{BS}}{\langle \hat{S}^2 \rangle_{HS} - \langle \hat{S}^2 \rangle_{BS}} \quad (7)$$

$$J = -\frac{-319.3355866 \text{ cm}^{-1}}{20.1128 - 4.0989}$$

$J = +19.9 \text{ cm}^{-1}$ $(3sf)$

The calculated exchange coupling constant of +19.9 cm^{-1} is consistent with ferromagnetic coupling. This calculated *J* value is larger than those reported by Berg *et al.* for the two bis-μ-alkoxo Mn^{III} dimers with Jahn-Teller axes in a perpendicular orientation. These complexes had calculated *J* values of +9.45 and +9.8 cm^{-1}, with corresponding experimental *J* values of +6.25 and +9.85 cm^{-1}.[7] However, these calculated *J* values were determined using the equation advocated by Ruiz *et al.*:[11a, 46]

$$J = -\frac{E_{HS} - E_{BS}}{4S_1S_2 + 2S_2} \quad (6)$$

Based on this equation, the calculated *J* value for the di-manganese complex would instead be 16.0 cm^{-1}, which remains larger than those reported by Berg and coworkers.

3.3.4 Further investigation of the ferromagnetic di-manganese complex

The bond lengths, molecular orbitals, spin densities and orbital overlap integrals of the computationally optimised ferromagnetic complex, the most energetically favourable structure, were then investigated. This allowed the Jahn-Teller distortions and the coupling of the manganese centres to be explored.

3.3.4.1 Bond lengths

Optimisation of the structure of the di-manganese complex allowed a comparison to be made between the metal-ligand bond lengths of the calculated structure with the experimental bond lengths as determined by X-ray crystallography. For Mn(1), where there was thought to be Jahn-Teller-like elongation, the axial bonds were expected to be longer than the equatorial bonds. For Mn(2), where there was predicted Jahn-Teller-like compression, the equatorial bonds were expected to be longer that the axial ones. The calculated bond lengths for the optimised structure are given in table 10.

Table 10. Calculated bond lengths for the ferromagnetic di-manganese complex.

Atoms	Type of coordination bond	Range of bond lengths in literature (Å)[56]	Experimental bond length (Å)	Computed bond length (Å)
Mn1-O11 (phenolate)	equatorial	1.807 – 1.948	1.926(4)	1.95851
Mn1-O12 (phenolate)	equatorial	1.807 – 1.948	1.943(4)	1.95858
Mn1-O100 (hydroxyl)	equatorial	1.826 – 2.126	1.913(4)	1.91147
Mn1-O101 (hydroxyl)	equatorial	1.826 – 2.126	1.917(4)	1.91115
Mn1-O212 (aldehyde)	axial	1.854 – 2.285	2.281(5)	2.30201
Mn1-O222 (aldehyde)	axial	1.854 – 2.285	2.258(4)	2.30211
Mn2-O13 (phenolate)	axial	1.867 – 1.989	1.882(5)	1.92143
Mn2-O14 (phenolate)	axial	1.867 – 1.989	1.893(5)	1.92133
Mn2-O100 (hydroxyl)	equatorial	1.826 – 2.126	2.085(5)	2.14758
Mn2-O101 (hydroxyl)	equatorial	1.826 – 2.126	2.079(4)	2.14963
Mn2-N232 (oxime)	equatorial	2.042 – 2.291	2.094(6)	2.10114
Mn2-N242 (oxime)	equatorial	2.042 – 2.291	2.096(7)	2.10248

At the Mn(1) centre, the axial metal-ligand bonds were longer than the equatorial ones, which was consistent with Jahn-Teller elongation. The calculated bond lengths were also consistent with the experimental bond lengths obtained by from X-ray crystallographic analysis, although the calculated aldehyde Mn-O and phenolate Mn-O bond lengths were slightly outside of the range of bond lengths of similar structures in the Cambridge Structural Database.[56]

At the Mn(2) centre, the equatorial metal-ligand bonds were longer than the axial ones, which was consistent with Jahn-Teller compression. The calculated bond lengths were also consistent with the experimental bond lengths obtained by from X-ray crystallographic analysis, although the calculated hydroxyl Mn-O bond lengths were slightly outside of the range of bond lengths of similar structures in the Cambridge Structural Database.[56]

3.3.4.2 Molecular orbitals

Following the optimisation of the ferromagnetic complex, the molecular orbitals of the complex were investigated to allow comparison between the calculated molecular orbitals and the expected molecular orbital diagrams for Jahn-Teller elongation and compression illustrated in section 1.3. For Jahn-Teller elongation to be present at Mn(1), the d_{z^2} orbital was expected to be singly occupied and lower in energy than the unoccupied $d_{x^2-y^2}$ orbital. At Mn(2) where Jahn-Teller compression was expected, the d_{z^2} orbital should be unoccupied and higher in energy than the singly occupied $d_{x^2-y^2}$ orbital.[14] The shapes and compositions of the orbitals provided information on the character of the molecular orbitals of the complex.

The contributions from manganese *d* orbitals to the molecular orbitals were first examined. The population analysis of the 100 highest energy filled MOs and 100 lowest energy MOs was requested by including the keyword *Pop=Orbitals=100*. For each orbital, the output of the population analysis gives the orbital energy and a relative contribution of the basis functions for a given angular momentum per atom. A contribution of 1 represents 100% contribution. A list of selected α molecular orbitals which contain contributions from manganese *d* orbitals is given in Figure 27. "occ" and "vir" refer to whether the orbitals are occupied or virtual (unoccupied) respectively. OE stands for the orbital energy, which is given in Hartrees.

```
Alpha occ 191 OE=-0.748 is Mn2-d=0.07
Alpha occ 196 OE=-0.742 is Mn2-d=0.08
Alpha occ 202 OE=-0.736 is Mn2-d=0.10
Alpha occ 208 OE=-0.728 is Mn2-d=0.22
Alpha occ 209 OE=-0.727 is Mn2-d=0.05
Alpha occ 213 OE=-0.722 is Mn2-d=0.13
Alpha occ 214 OE=-0.721 is Mn2-d=0.07
Alpha occ 215 OE=-0.719 is Mn2-d=0.12
Alpha occ 217 OE=-0.716 is Mn1-d=0.15
Alpha occ 221 OE=-0.710 is Mn1-d=0.23
```

```
Alpha occ 223 OE=-0.702 is Mn1-d=0.20 C92-p=0.10 C128-p=0.10
Alpha occ 224 OE=-0.700 is Mn2-d=0.16
Alpha occ 225 OE=-0.698 is Mn1-d=0.11
Alpha occ 226 OE=-0.697 is Mn1-d=0.13
Alpha occ 229 OE=-0.687 is Mn1-d=0.07
Alpha occ 230 OE=-0.686 is Mn1-d=0.37 Mn2-s=0.16
Alpha occ 232 OE=-0.685 is Mn1-d=0.11
Alpha occ 233 OE=-0.684 is Mn1-d=0.11
Alpha occ 235 OE=-0.678 is Mn1-d=0.31
Alpha occ 236 OE=-0.676 is Mn2-d=0.55
Alpha occ 238 OE=-0.675 is Mn1-d=0.05
Alpha occ 239 OE=-0.673 is Mn2-d=0.13
Alpha occ 240 OE=-0.672 is Mn2-d=0.16
Alpha occ 246 OE=-0.656 is Mn2-d=0.13
Alpha occ 259 OE=-0.624 is Mn2-d=0.10
Alpha occ 264 OE=-0.601 is Mn1-d=0.13 O4-p=0.12 O3-p=0.12
Alpha occ 265 OE=-0.599 is O3-p=0.33 O4-p=0.33 Mn1-d=0.18
Alpha occ 273 OE=-0.566 is Mn2-d=0.34
Alpha occ 274 OE=-0.558 is Mn1-d=0.23 O50-p=0.17 O49-p=0.17
Alpha vir 281 OE=-0.442 is Mn2-d=0.57
Alpha vir 282 OE=-0.418 is Mn1-d=0.54 O4-p=0.11 O3-p=0.11
```

Figure 27. Selected output of orbital contributions for α molecular orbitals which contain contributions from manganese *d* orbitals.

Selected β molecular orbitals which contain contributions from manganese *d* orbitals are given in figure 28. These orbitals were all unoccupied, which was consistent with ferromagnetic coupling, where all electrons are in the α-spin state.

```
Beta  vir 273 OE=-0.399 is Mn2-d=0.68
Beta  vir 274 OE=-0.395 is Mn1-d=0.19 Mn2-d=0.14 C132-p=0.11 C90-p=0.11
Beta  vir 275 OE=-0.393 is Mn2-d=0.50
Beta  vir 276 OE=-0.390 is Mn2-d=0.62
Beta  vir 277 OE=-0.389 is Mn2-d=0.19 C90-p=0.12 C132-p=0.12
Beta  vir 278 OE=-0.375 is Mn1-d=0.71
Beta  vir 279 OE=-0.365 is Mn1-d=0.49
Beta  vir 280 OE=-0.364 is Mn1-d=0.80
Beta  vir 281 OE=-0.362 is Mn1-d=0.23 Mn2-d=0.19
Beta  vir 284 OE=-0.352 is Mn2-d=0.57
Beta  vir 285 OE=-0.348 is Mn2-d=0.34
Beta  vir 286 OE=-0.345 is Mn2-d=0.41 Mn1-d=0.21
Beta  vir 289 OE=-0.338 is Mn1-d=0.68
Beta  vir 290 OE=-0.328 is C113-s=0.11 Mn2-d=0.11 C79-s=0.11
```

Figure 28. Selected output of orbital contributions for β molecular orbitals which contain contributions from manganese *d* orbitals.

In Gaussian 09, it is not possible to obtain a print-out of which type of *d* orbitals contribute to a molecular orbital. However, the orbitals listed in figures 27 and 28 which contained manganese *d* orbital character were further investigated by rendering their molecular orbitals and observing the *d* orbital character present. The most relevant orbitals are given in Figures 29 – 32. Each of the four orbitals pictured showed clear $d_{x^2-y^2}$ or d_{z^2} character, and the ordering of these orbitals can be compared to the expected molecular orbital diagrams for Jahn-Teller distortions.

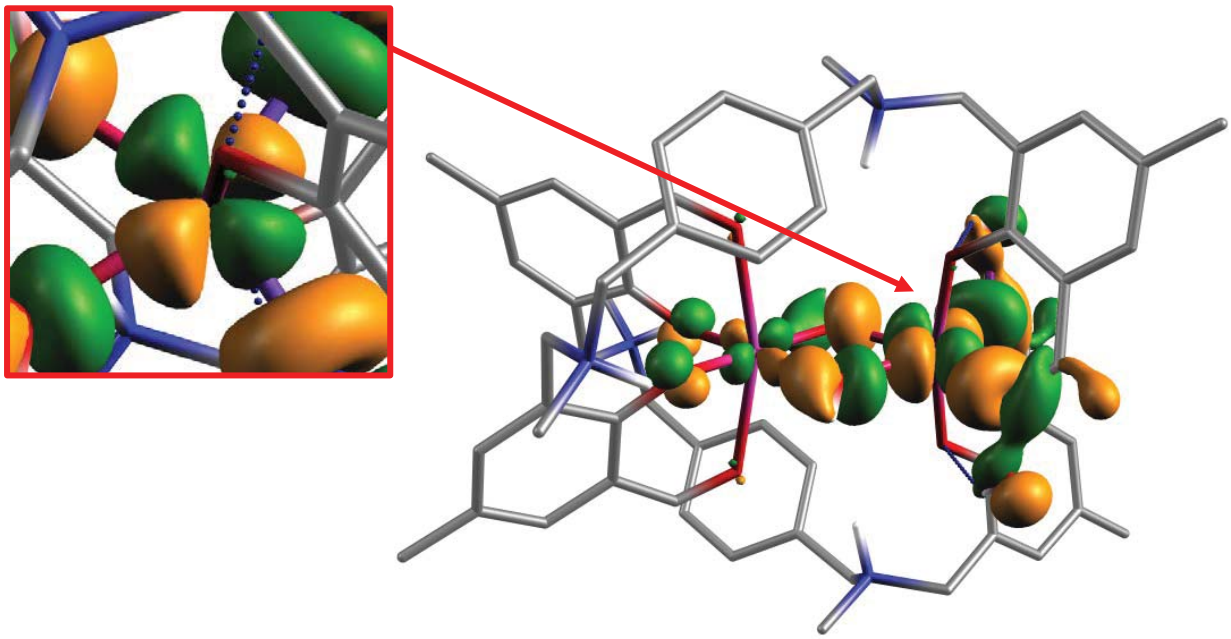

Figure 29. Molecular orbital 273α, including a close-up of the $d_{x^2-y^2}$ character at Mn(2).

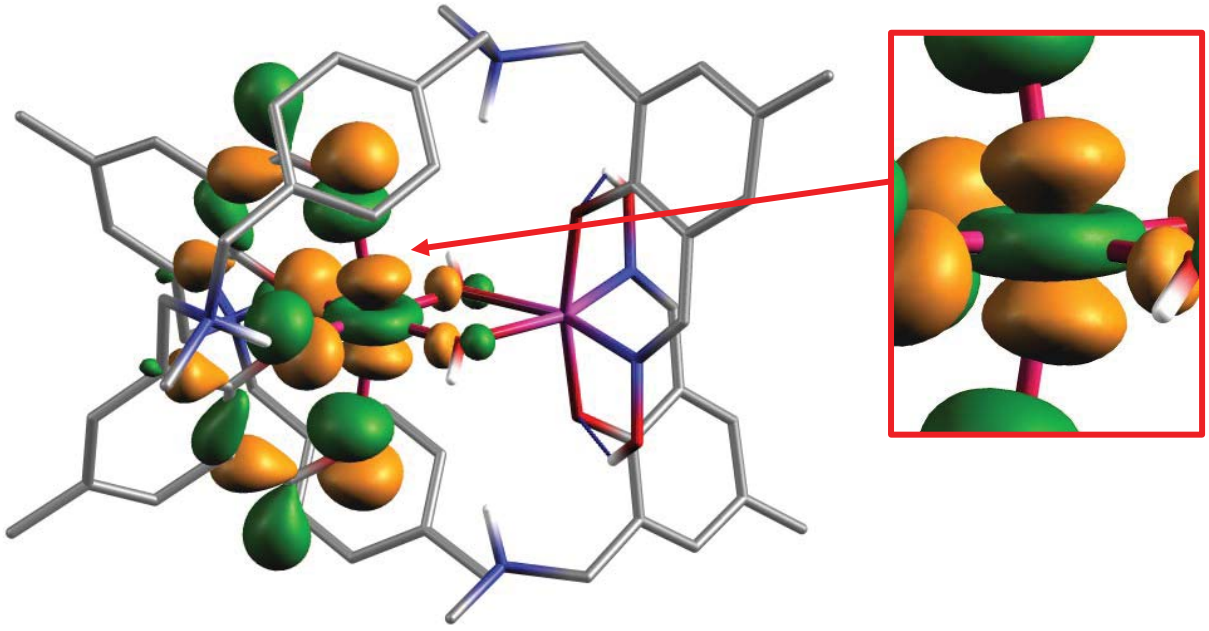

Figure 30. Molecular orbital 274α, including a close-up of the d_{z^2} character at Mn(1).

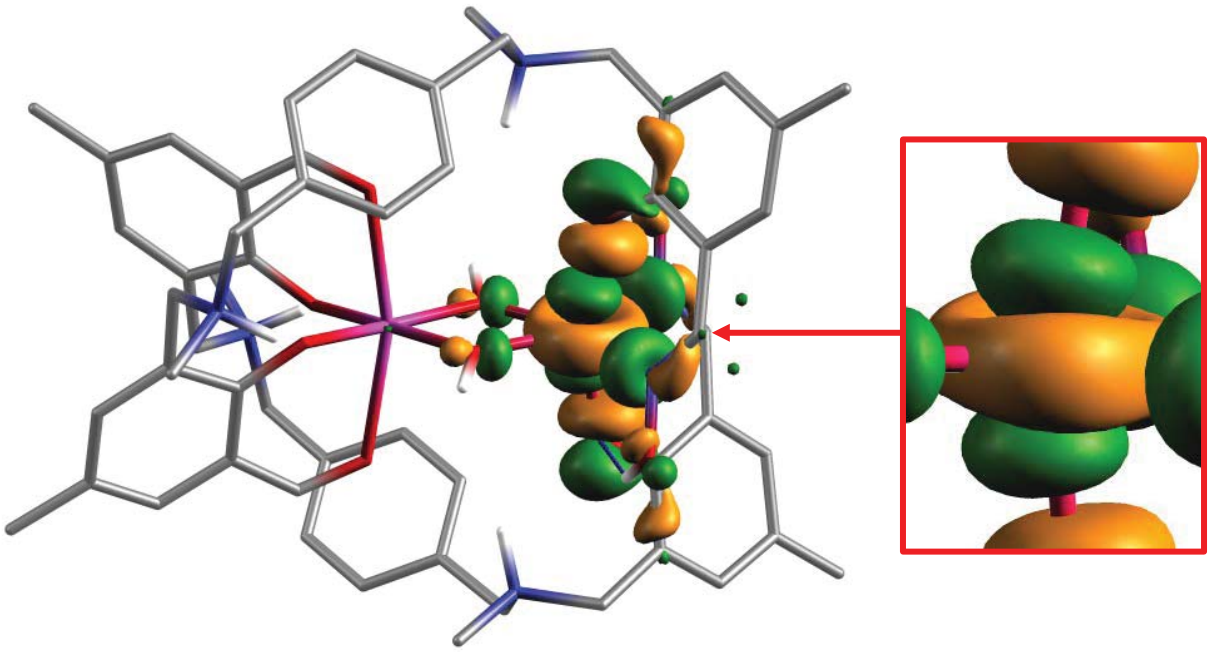

Figure 31. Molecular orbital 281α (LUMO), including a close-up of the d_{z^2} character at Mn(2).

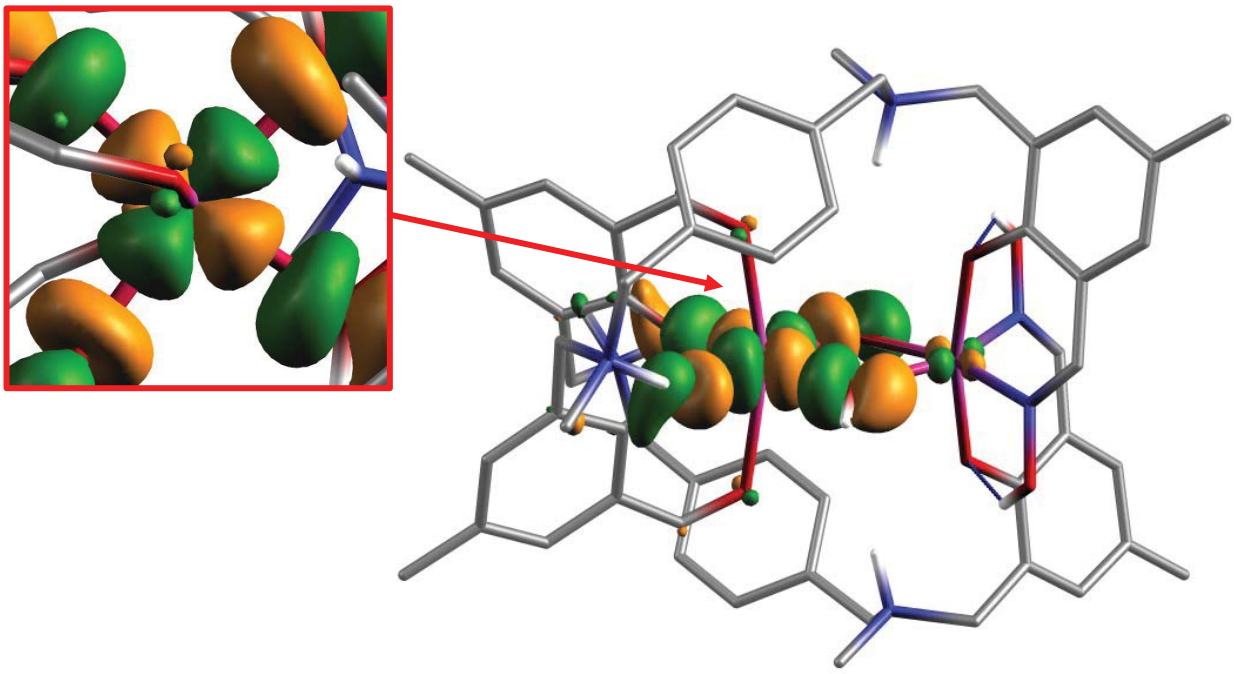

Figure 32. Molecular orbital 282α (LUMO+1), including a close-up of the $d_{x^2-y^2}$ character at Mn(1).

Figures 30 and 32 show that molecular orbital 274α (E = -0.558 Hartrees) exhibited Mn(1) d_{z^2} character while molecular orbital 282α (E = -0.418 Hartrees) exhibited Mn(1) $d_{x^2-y^2}$ character. Mn(1) was expected to have Jahn-Teller elongation. Therefore the calculated molecular orbitals can be compared to the molecular orbital diagram for Jahn-Teller elongation (Figure 33).

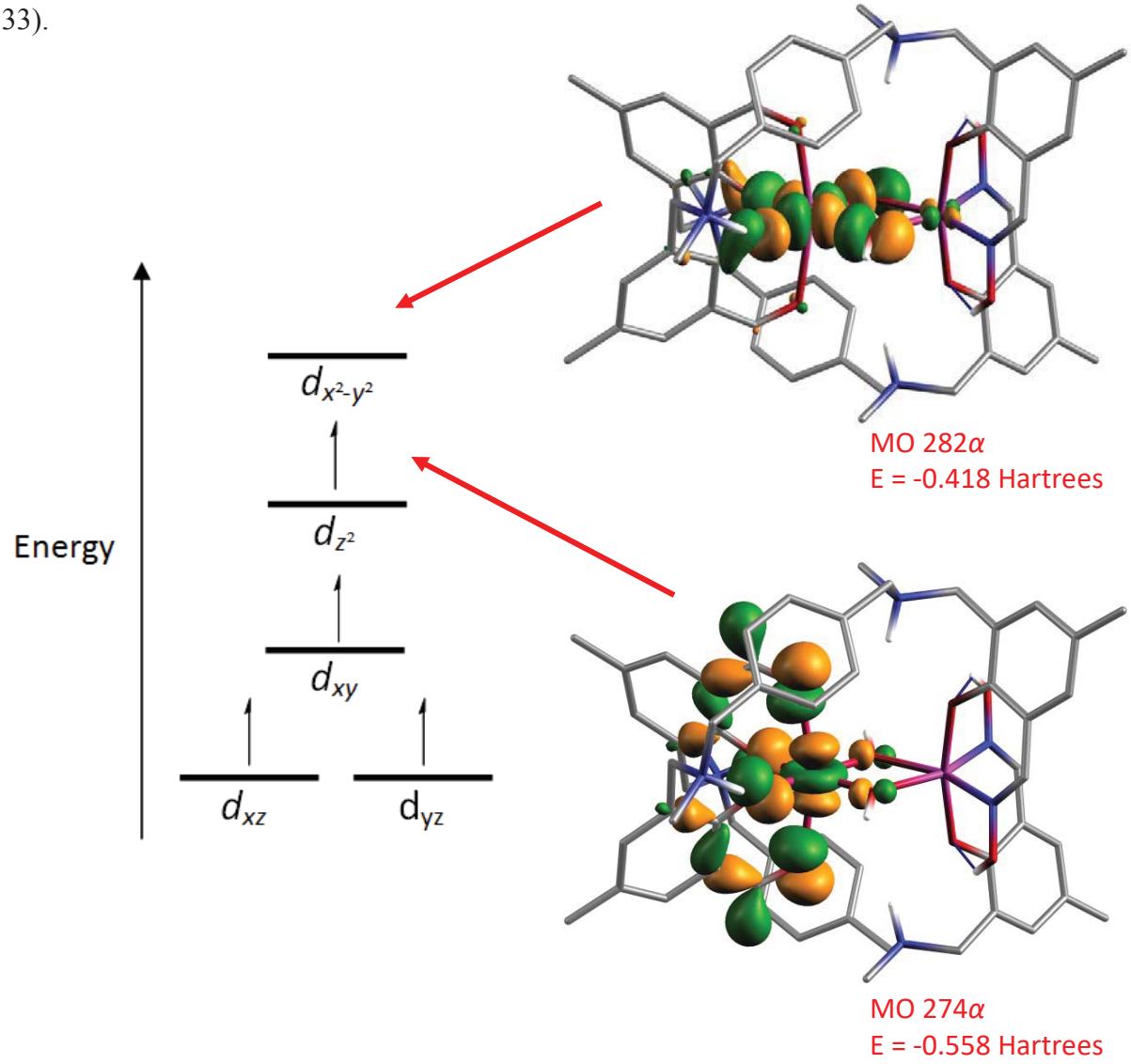

Figure 33. Comparison between molecular orbitals at Mn(1) and the expected ordering of orbitals when Jahn-Teller elongation is present.

The Mn(1) centred molecular orbital with d_{z^2} character (MO 274α) was lower in energy than the Mn(1) centred molecular orbital with $d_{x^2-y^2}$ character (MO 282α) by 326 nm. This was consistent with the expected ordering of the molecular orbitals for Jahn-Teller elongation. The energy difference would result in an absorbance at 326 nm, and is consistent with the broad charge transfer band at ~ 350 nm in a UV/Vis spectrum of Willoughby's dinuclear complex. Therefore, analysis of the calculated molecular orbitals gives further evidence that Jahn-Teller elongation is present at Mn(1).

Figures 29 and 31 show that molecular orbital 273α (E = -0.566 Hartrees) displayed Mn(2) $d_{x^2-y^2}$ character while molecular orbital 281α (E = -0.442 Hartrees) exhibited Mn(2) d_{z^2} character. Mn(2) was expected to have Jahn-Teller compression. Therefore the calculated molecular orbitals can be compared to the molecular orbital diagram for Jahn-Teller compression (Figure 34).

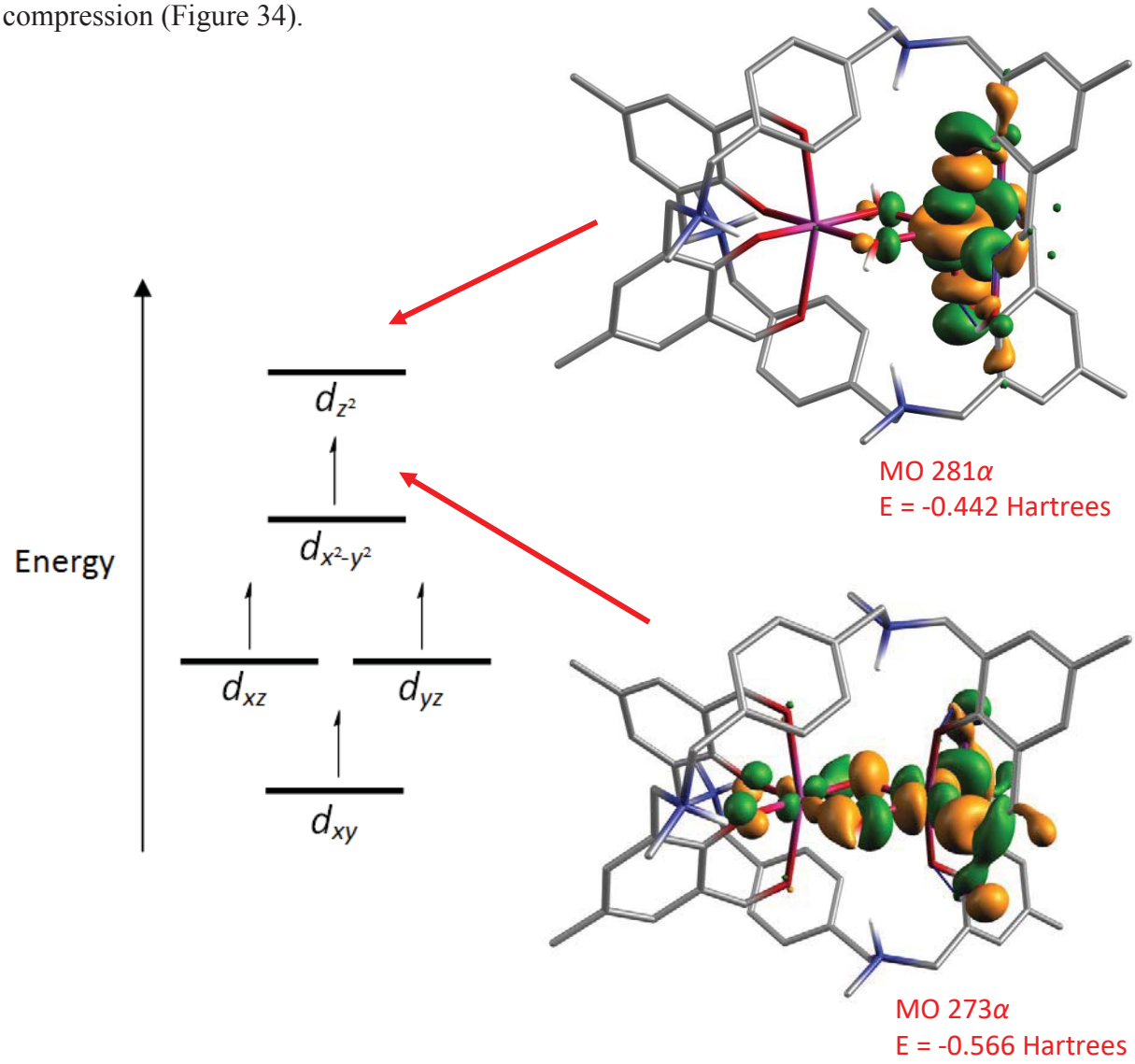

Figure 34. Comparison between molecular orbitals at Mn(2) and the expected ordering of orbitals when Jahn-Teller compression is present.

The Mn(2) centred molecular orbital with $d_{x^2-y^2}$ character (MO 273α) was lower in energy than the Mn(2) centred molecular orbital with d_{z^2} character (MO 281α) by 0.139 Hartrees. This was consistent with the expected ordering of the molecular orbitals for Jahn-Teller compression. The energy difference would result in an absorbance at 369 nm, and is consistent with the broad charge transfer band at ~ 350 nm in a UV/Vis spectrum of Willoughby's dinuclear complex. Therefore, analysis of the calculated molecular orbitals gives further evidence that Jahn-Teller compression is present at Mn(2).

The remaining molecular orbitals with contributions from the manganese *d* orbitals were also rendered. Multiple orbitals showed d_{xz}, d_{yz} or d_{xy} character at each manganese centre; therefore the orbitals with the highest *d* orbital contribution showing d_{xz}, d_{yz} or d_{xy} character were selected. A summary of the *d* orbitals for the optimised dinuclear manganese complex is given in table 11.

Table 11. Molecular orbitals with d orbital character centred at Mn(1) and Mn(2).

***d* orbital**	**Mn(1)**	**Mn(2)**
$\boldsymbol{d_{xy}}$	235α	236α
$\boldsymbol{d_{yz}}$	265α	208α
$\boldsymbol{d_{xz}}$	221α	240α
$\boldsymbol{d_{x^2-y^2}}$	282α	273α
$\boldsymbol{d_{z^2}}$	274α	281α

3.3.4.3 Overlap integrals of molecular orbitals

The overlap integrals of the molecular orbitals provided information about the coupling between the manganese centres. The ferromagnetic contribution to the magnetic exchange (J_F) arises from the cross interaction between singly occupied molecular orbitals (SOMOs) and unoccupied *d* orbitals. The antiferromagnetic contribution (J_{AF}) is associated with the overlap between SOMOs.[7] The overlap integral values for the molecular orbitals in table 11 are given in table 12.

Table 12. Overlap integral values for the dinuclear manganese complex (SOMOs highlighted in red).

		Mn(2)				
		d_{xy}	d_{yz}	d_{xz}	$d_{x^2-y^2}$	d_{z^2}
Mn(1)	d_{xy}	0.000	**-0.093**	0.000	0.000	0.008
	d_{yz}	-0.016	**0.237**	0.000	0.000	0.000
	d_{xz}	-0.005	0.000	0.007	0.000	0.008
	$d_{x^2-y^2}$	**-0.074**	0.003	0.000	0.000	0.000
	d_{z^2}	0.000	0.000	0.000	0.000	0.000

The most notable orbital interactions are between the Mn(1) d_{yz} and Mn(2) d_{yz} orbitals and the Mn(1) d_{xy} and Mn(2) d_{yz} orbitals. These interactions are between two SOMOs, therefore

would lead to an antiferromagnetic contribution to the *J* value. There is also a significant ferromagnetic contribution to the *J* value resulting from the overlap between the Mn(1) $d_{x^2-y^2}$ orbital and Mn(2) d_{xy} orbitals. The analysis of the overlap integral values suggests there may be a net antiferromagnetic rather than ferromagnetic coupling in the dinuclear manganese complex in contrast to the ferromagnetic and broken symmetry calculations (Section 3.3.3).

The value of the exchange coupling constant calculated in section 3.3.3 depended on the quality of both the ferromagnetic and antiferromagnetic (broken symmetry) optimisations. Further calculations of the broken symmetry state may need to be completed, as the overlap integral analysis suggests that antiferromagnetic coupling in the dinuclear manganese complex may be more favourable, which would lead to the broken symmetry state of the dinuclear complex being lower in energy than the ferromagnetic state. Unfortunately this could not be pursued further.

3.3.4.4 Spin density plot

A spin density plot is used to visualise the spin distribution on the atoms of a molecule. The spin density plot of the optimised dinuclear manganese complex is given in figure 35. The blue surface (positive spin density) represents an excess of α-electron density, while the green surface (negative spin density) represents an excess of β-electron density.

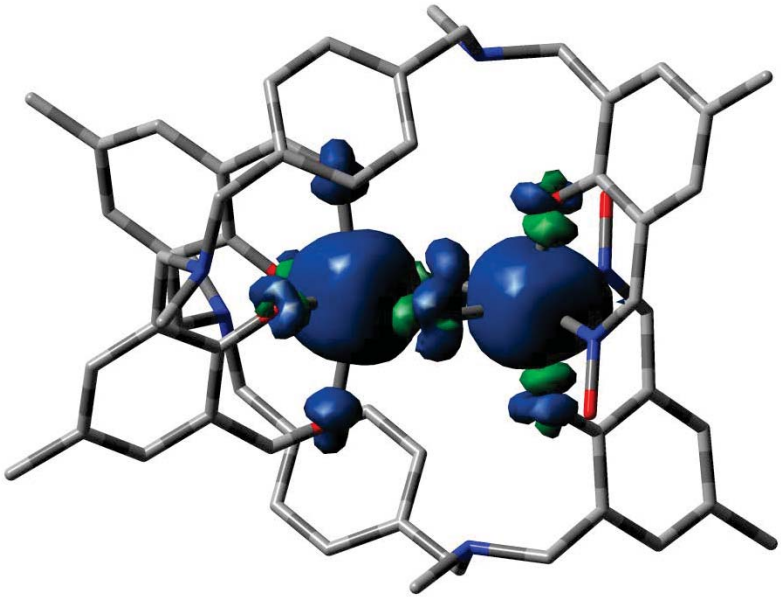

Figure 35. Spin density plot of the optimised dinuclear manganese complex.

The plot shows α-electron density at both manganese centres, which suggests that the electrons at Mn(1) and Mn(2) are in the same spin state, as expected with ferromagnetic coupling between the two manganese ions.

Spin density is transferred from the metal to neighbouring atoms by two methods: *spin delocalisation* and *spin polarisation*. Spin delocalisation is the direct transfer of spin density from the metal to another atom. It results from the mixing of ligand orbitals with a metal *d* orbital to form the metal orbital with an unpaired electron.[64] In spin polarisation, the unpaired spin at one atom induces a spin of opposite sign at a neighbouring atom.[64]

At Mn(1), the d_{z^2} orbital is singly occupied, while the $d_{x^2-y^2}$ orbital is unoccupied. Spin delocalisation is expected to dominate at ligands coordinated along the Mn(1) Jahn-Teller axis, coinciding with the d_{z^2} orbital. This is consistent with the spin density plot as there is positive spin density located on the axial oxygen atoms at Mn(1), which suggests spin delocalisation is predominant in this direction.

At the hydroxyl oxygen atoms and the axial phenolate oxygen atoms at Mn(2) there appears to be a mixture of spin polarisation and spin delocalisation. There is negligible spin density at the equatorial oxygen atoms at Mn(1) and equatorial nitrogen atoms at Mn(2).

3.3.4.5 Hydrogen bonding

Another feature of the di-manganese complex was the intramolecular hydrogen bonding between the phenolate oxygen atoms and the hydrogen atoms of the oxime groups at Mn(2). Hydrogen bonding was successfully modelled by using diffuse functions in the basis set for C, H, N and O atoms. The X-ray crystallographic analysis of Willoughby's structure was not of sufficient quality to locate the hydrogens atoms of the oxime groups. The computational modelling of the dinuclear complex gave a visualisation of the hydrogen bonding present between the phenolate oxygen atoms and the hydrogen atoms of the oxime groups at Mn(2). This hydrogen bonding was visualised in Chemcraft (Figure 36).

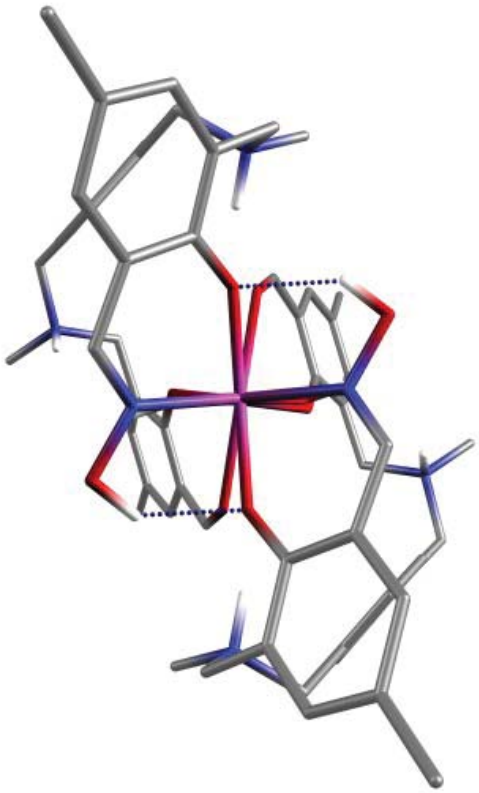

Figure 36. Side view of the dinuclear manganese complex showing the hydrogen bonding present.

3.4 Summary

The ferromagnetic and antiferromagnetic states of the dinuclear manganese complex were modelled. The optimised ferromagnetic complex was found to be the most energetically favourable structure. The bond lengths of the optimised structure were consistent with the experimental bond lengths obtained by X-ray crystallographic analysis of Willoughby's complex. The calculated bond lengths and ordering of the d_{z^2} and $d_{x^2-y^2}$ orbitals gave further evidence for the presence of Jahn-Teller elongation at Mn(1) and Jahn-Teller compression at Mn(2).

The calculated exchange coupling constant was +19.9 cm^{-1}, which was consistent with ferromagnetic coupling between the manganese centres. However, the analysis of the overlap integrals of the manganese *d* orbitals showed significant antiferromagnetic contributions to the exchange coupling constant, which may indicate further calculations are required to find a lower energy broken symmetry state.

The spin density plot for the ferromagnetic structure showed spin delocalisation along the *z* axis at Mn(1) and a mixture of spin polarisation and delocalisation at the hydroxyl oxygen atoms and the axial phenolate oxygen atoms at Mn(2).

The hydrogen bonding between the phenolate oxygen atoms and the hydrogen atoms of the oxime groups at Mn(2) was visualised in the computational modelling of the dinuclear manganese complex.

Chapter 4: Experimental Approaches

4.1 Introduction

A nonsymmetrical dinuclear manganese complex was serendipitously synthesised by Willoughby in 2011 by a complexation reaction beginning with the di-oxime **L1** (Figure 37). The reaction contained **L1**, $Mn(ClO_4)_2$ and MeONa in a 1:2:2 ratio in acetonitrile. The solution was stirred for 30 – 60 minutes, filtered and left to evaporate. Black rod-shaped crystals suitable for X-ray diffraction analysis were formed over a week in a ~7% yield by the slow diffusion of diethyl ether into an acetonitrile solution containing the complex. Upon solving the structure it was clear the complexed ligand differed from the di-oxime starting ligand. Willoughby concluded that the partial hydrolysis of **L1** had occurred to form the mono-oxime **L2** (Figure 38). This report suggests another pathway may be to blame: the complex may have formed from the ~6% mono-oxime impurity in Willoughby's sample of **L1**.

One of the aims of the current research was to re-synthesise the dinuclear manganese complex in suitable quantity and quality to fully investigate its structural and magnetic properties. The planned structural and magnetic characterisation included X-ray crystallographic analysis, elemental analysis, magnetics and electron paramagnetic resonance (EPR). The yield of the dinuclear complex needed to be increased significantly in order to obtain a suitable quantity of complex for complete analysis.

Ultimately, after exhaustive attempts it was not possible to repeat the synthesis of the dinuclear complex. The following chapter outlines the many attempts that were performed.

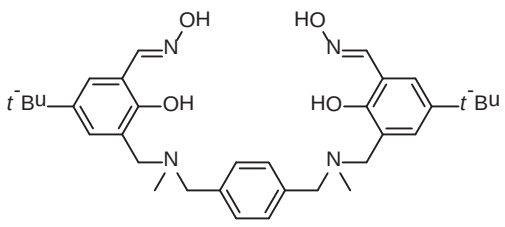

Figure 37. (1*E*,1'*E*)-5-*tert*-Butyl-3-(((4-(((5-*tert*-butyl-2-hydroxy-3-((*E*)(hydroxyimino)methyl) benzyl)(methyl)amino)methyl)benzyl)(methyl) amino)methyl)-2-hydroxybenzaldehyde oxime (**L1**).[53]

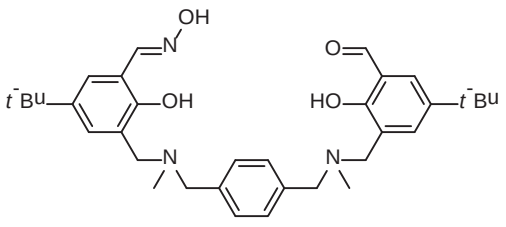

Figure 38. (1*E*,1'*E*)-5-*tert*-Butyl-3-(((4-(((5-*tert*-butyl-2-hydroxy-3-((*E*)(hydroxyimino)methyl) benzyl)(methyl)amino)methyl)benzyl)(methyl) amino)methyl)-2-hydroxybenzaldehyde (**L2**).[53]

4.2 Synthetic Route

Three different synthetic routes were attempted for the synthesis of the dinuclear manganese complex (Figure 39). The first route (A), similar to that of Willoughby, consisted of the synthesis of the di-oxime **L1** using conditions (v) followed by the attempted formation of the complex (vi). The second route (B) combined oximation and complexation reactions of the di-aldehyde **1c** in a one-pot synthesis (vii). The third route (C) involved the synthesis of the partially oximated ligand **L2** using conditions (viii), followed by a complexation reaction (ix).

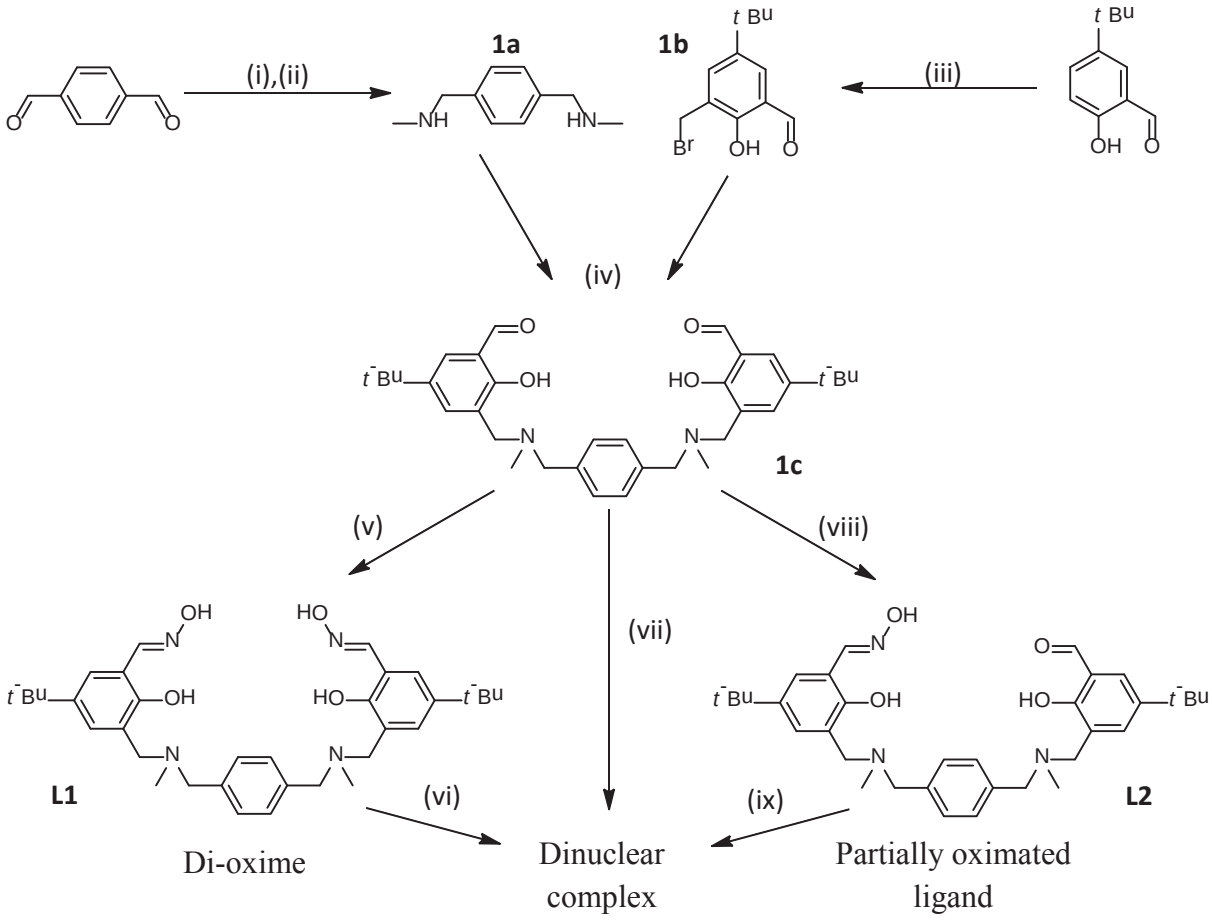

Figure 39. Synthetic routes for the synthesis of the dinuclear manganese complex. Reagents and conditions: (i) $MeNH_2 \cdot HCl$/KOH, MeOH, rt, 2 h; (ii) $NaBH_4$ / MeOH, rt, 1 h; (iii) Paraformaldehyde / HBr / H_2SO_4, 70°C, 20 h; (iv) Et_3N, CH_2Cl_2 , rt, 17 h; (v) $NH_2OH \cdot HCl$ / KOH, EtOH, rt, 17 h; (vii) 2 equiv. $NH_2OH \cdot HCl$ / KOH, CH_3CN / EtOH, 17 h (viii) $NH_2OH \cdot HCl$ / KOH.

Depending on the route complexation was performed *in situ* or sequential following a standard procedure outlined in the following sections. The isolation and characterisation of the complexes were standardised as outlined below.

After each of the complexations, the following procedure was adhered to. Slow diffusion of diethyl ether into an acetonitrile solution containing the complex was performed twice: the first to isolate the complex and the second in an attempt to form X-ray quality crystals. Direct reduction of the solvent by rotary evaporation was avoided as the counter ion was a perchlorate. If no crystals formed, attenuated total reflection infrared spectroscopy (ATR-IR) of the solid material was conducted in order to determine the ratio of imine to aldehyde peaks. Clearly, both the presence of an imine and aldehyde stretch was a desirable outcome. The imine peak was expected to be in the range 1690 – 1620 cm^{-1}.[65] For a non-coordinated organic compound, an aromatic aldehyde peak is usually in the range 1720 -1680 cm^{-1}, however the peak may shift to a lower frequency upon coordination.[65-66] In the literature, the manganese bound C=O peak is close to that of the imine.[67] Based on the IR spectra of Willoughby, the manganese bound C=O peak was expected to be found at approximately 1646 cm^{-1}.[53] If the IR analysis suggested the sample was a viable candidate for the dinuclear complex, CHN analysis was performed on the solid to further aid in the determination of its composition.

4.3 Results and Discussion

4.3.1 Route A

Willoughby originally synthesised the dinuclear manganese complex by a complexation reaction beginning with the di-oxime **L1**. There were three ways that the dinuclear complex may have formed from Willoughby's di-oxime **L1**. Firstly, there may have been partial hydrolysis during the complexation reaction, followed by the formation of X-ray crystallography quality crystals. Secondly, the partial hydrolysis may have instead occurred during the week that the X-ray crystal growth was attempted following complexation. Thirdly, the complex may have formed from the ~6% mono-oxime impurity in Willoughy's sample of **L1**. This third option will be discussed in route C.

L1 was synthesised from the di-aldehyde **1c** by a Schiff-base oximation reaction and recrystallized in hot ethanol. ^{1}H NMR analysis confirmed that the desired product had been successfully synthesised in high purity (Figure 40).

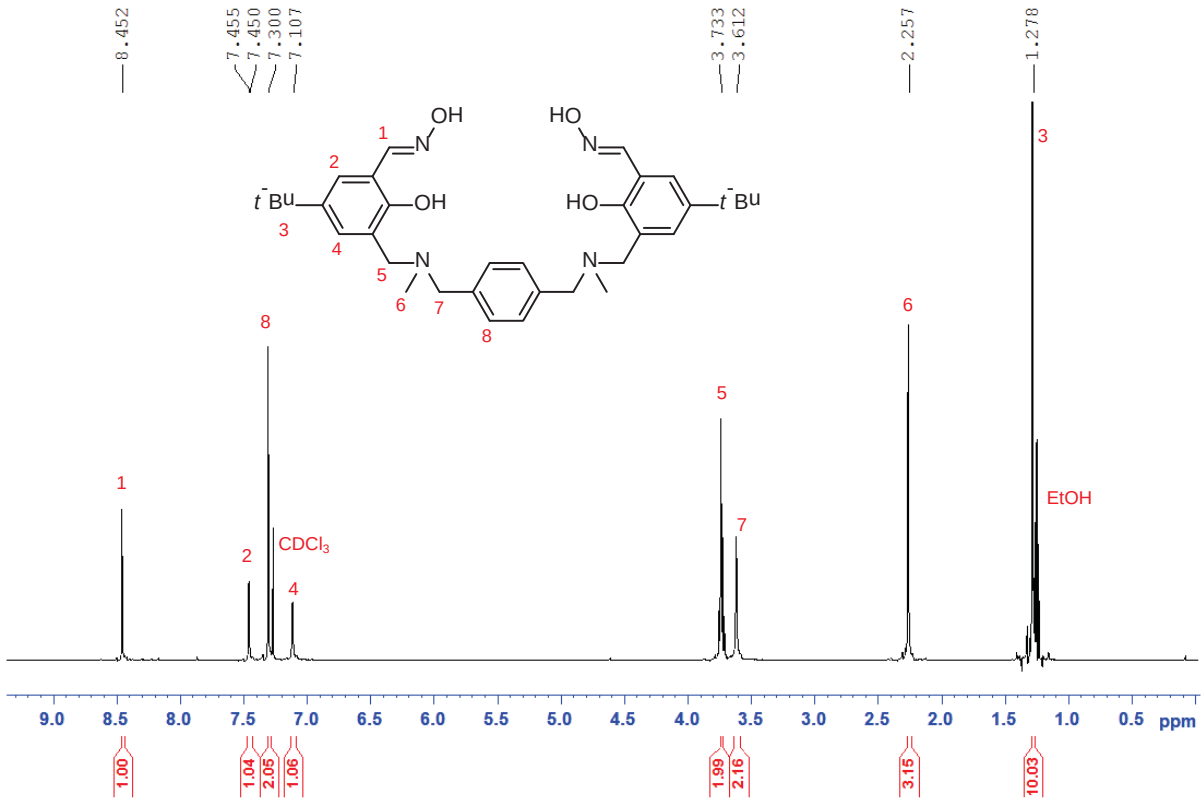

Figure 40. ^{1}H NMR spectrum of **L1**.

A variety of different conditions were trialled in order to attempt the synthesis of the dinuclear manganese complex. Firstly, the reaction was repeated with the same reaction conditions as those reported by Willoughby. Different ratios of **L1** : Mn : base were also trialled. Most reactions were attempted with a 1:1:1 ratio of **L1** : Mn : base, as this was consistent with the formation of the dinuclear manganese complex. The reaction time was extended for some of the reactions in order to allow more time for the suspected ligand hydrolysis to occur. One reaction attempt was heated at reflux in order to add energy to the reaction. Another reaction attempt included the addition of a small percentage of water in order to help drive the hydrolysis. In the presence of an aldehyde, the hydrolysis of oximes has been found to increase.[53] For this reason, **L1** was doped with varying amounts of the di-aldehyde **1c** in other trials of the complexation reaction. The reaction solutions ranged in colour from dark green to dark brown.

The same solvent system used by Willoughby (acetonitrile and diethyl ether) was used in each slow diffusion recrystallisation of the complexation reactions completed. Based on X-ray diffraction analysis of the crystal structure of Willoughby's complex, acetonitrile was present in the crystal structure of the dinuclear complex. This supports the use of acetonitrile as one of the solvents in the recrystallisation by slow diffusion. The recrystallisation by slow diffusion was repeated twice for each reaction. When the first attempt for each reaction was unsuccessful, the solid was separated from the solution, re-dissolved in acetonitrile and again set up for slow diffusion. The remaining mother liquor was also set up for a slow diffusion recrystallisation attempt. In addition to the slow diffusion attempts, a vial containing the remaining sample was also set up for slow evaporation in another attempt at forming crystals.

None of the complexation reactions yielded crystals suitable for X-ray crystallographic analysis. A few of the vials had shown signs of crystal formation, but further attempts to form crystals had no success. The precipitated solids were dark green, brown, or black in colour.

It was noted that in reaction 235 a black precipitate had formed after it had been left stirring for one week. Attempts were made to form crystals from both the solution as well as from the re-dissolved solid, but no suitable crystals formed.

ATR-IR spectra were collected for each solid sample to determine if they contained both imine and aldehyde peaks, indicating they were a viable candidate for further analysis. All samples contained a weak imine peak in the range 1657.2 – 1627.5 cm^{-1}. Most samples contained an aldehyde peak in the range 1697.1 – 1693.2 cm^{-1}. As the aldehyde peak was significantly higher than the imine, it suggests that the aldehyde was not bound to manganese. However, these aldehyde peaks were all very weak, indicating that the aldehyde was not present in sufficient quantities for the desired dinuclear complex to be present. CHN analysis was not performed on the samples from route A as they were not viable candidates based on the IR analysis.

The many unsuccessful attempts at synthesising the dinuclear manganese complex from the di-oxime **L1** suggested that this may not be the most suitable route for the synthesis. The di-oxime **L2** may not have been hydrolysed to the mono-oxime **L1** during Willoughby's original synthesis of the dinuclear complex. Instead, the complex may have formed from the ~6% mono-oxime impurity in Willoughy's sample of **L1** (see route C).

4.3.2 Route B

The oximation and complexation steps were combined in Route B in an attempt to synthesise the dinuclear manganese complex directly. This method was trialled in an effort to form the mono-oxime ligand and the complex immediately to prevent a statistical ratio of the ligand from being established. By having the reagents together in a one-pot synthesis, the complex could be produced without the need to synthesise and isolate the mono-oxime **L1**.

Several attempts were made for the combined oximation and complexation reactions. Different bases were trialled, including triethylamine and sodium methoxide, as well as the absence of a base.

For the first attempt of each reaction, as the solution was reduced in volume, 1 mL aliquots of sample were removed and isolated by vapour diffusion of diethyl ether into a vial containing the sample in acetonitrile solution. This provided a way to have differing concentrations of the reaction mixture to attempt formation of crystals. As for the samples in Route A, after product isolation by this method, the solid was separated from the solution, redissolved in

acetonitrile and again set up for slow diffusion. The remaining solution was also set up for a slow diffusion recrystallisation attempt.

The reaction JKB-217 was performed in the absence of a base and the reaction solution was dark green. Several of the vials set up for slow diffusion appeared to contain black rod-shaped crystals on the sides of the inner vials. The reaction was repeated four times (in two different scales) in order to synthesise the product in larger amounts so that it could be analysed by multiple techniques including X-ray crystallographic analysis, ^{1}H NMR analysis and UV-Vis spectroscopy. While the crystals appeared to be black under a magnifying glass, under a microscope it was revealed that they were instead transluscent rod-shaped crystals coated in black powder. This suggested that the desired product had not been synthesised, as the absence of colour in the crystals suggested a non-complexed product. IR analysis of the solid material showed a weak imine peak at 1633.3 cm^{-1} and a very weak aldehyde peak at 1695.0 cm^{-1}. Based on the IR analysis this reaction product was not a viable candidate for the dinuclear complex, therefore CHN analysis was not performed.

The reaction JKB-218 had sodium methoxide added as a base and the reaction solution was brown. After two attempts were made for the formation of crystals, brown solid had precipitated but no signs of crystal formation were observed. IR analysis of the solid material had a moderate imine peak at 1642.1 cm^{-1} and a weak aldehyde shoulder at 1695.1 cm^{-1}. Based on the IR analysis this reaction product was not a viable candidate for the dinuclear complex, therefore CHN analysis was not performed.

The reaction JKB-221 had triethylamine added as a base. On reduction of the dark brown solution, a black precipitate formed. The black powder was removed by filtration. Vials were set up for the slow diffusion of diethyl ether into a vial containing 1 mL of the reaction solution. Attempts were made to redissolve the black solid in acetonitrile for recrystallisation, but it would not dissolve. The reaction was repeated multiple times in order to synthesise more of the black solid in the hope of determining its composition. Elemental analysis (Table 13) indicated that the black solid was not the desired dinuclear manganese complex synthesised by Willoughby. However, the colour of the solid did suggest that it contained manganese.

Further attempts were made to recrystallise the black solid, however it was not soluble in many solvents. The solid was soluble in nitromethane, but vials set up for slow evaporation and for slow diffusion of diethyl ether did not yield crystals. The solid also had some solubility in methanol, ethanol, DMSO and DMF but attempts for recrystallisations using these solvents were also unsuccessful. A preliminary study using the technique of powder diffraction indicated that the solid was not of sufficient quality for an X-ray powder diffraction to be conducted to determine any structural information.

Table 13. CHN analysis of black solid produced in reaction JKB-225 compared to the CHN analysis of the dinuclear complex synthesised by Willoughby.

Measurement	%C	%H	%N
1	61.86%	6.93%	5.30%
2	61.76%	6.73%	5.44%
AW crystals	46.80%	5.67%	4.54%

CHN analysis was performed and is given in table 13. IR analysis of the black solid had a strong imine peak at 1635.2 cm^{-1} and a shoulder at 1673.9 cm^{-1} which may be due to an aldehyde stretch. There was an absence of a perchlorate peak at 1085 cm^{-1} which indicated that counter anions may be absent and the compound may be a neutral species.[68]

Mass spectrometer analysis of the black solid displayed a parent peak at 1261.6898 m/z and a base peak at 631.3484 m/z. These values were close to the molar masses of the chemical formulae $C_{68}H_{90}Mn_2N_6O_{10}$ (M_r = 1261.35 g mol^{-1}) and respectively $C_{34}H_{43}MnN_3O_4$ (M_r = 631.68 g mol^{-1}). Possible configurations for each of these formulae are given in Figure 41. The mass spectrometer analysis was consistent with the IR information but was not consistent with the CHN analysis. No candidate was found which fitted the CHN analysis as well as the IR analysis and the mass spectrometer analysis.

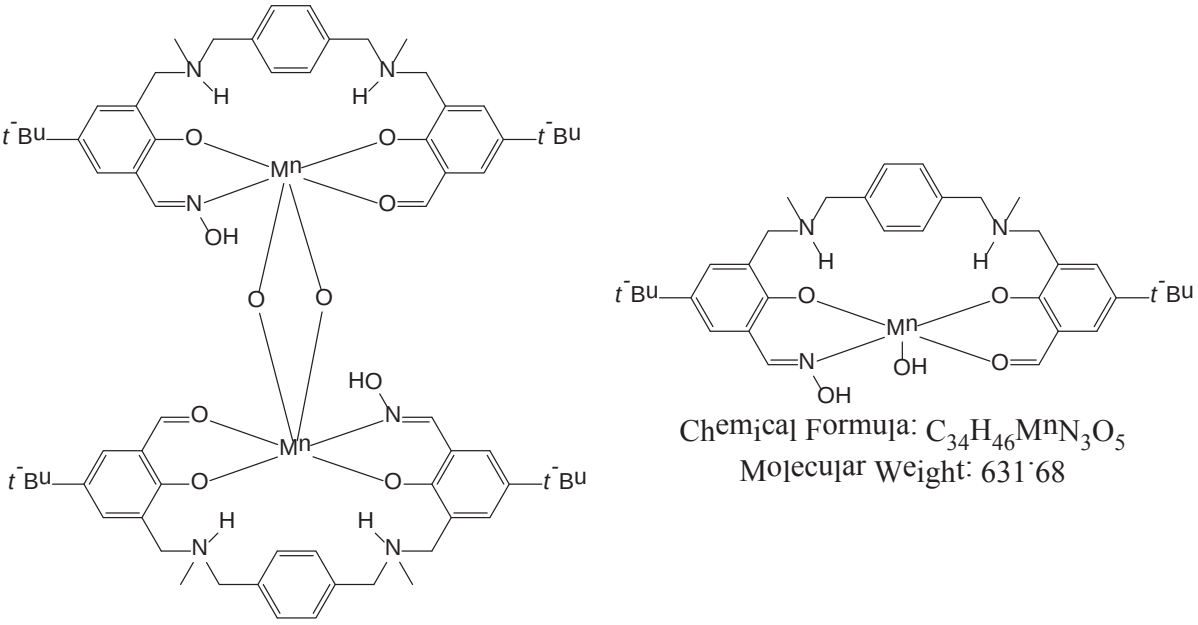

Figure 41. Chemical structures with molecular weights close to the m/z peaks of the mass spectrum.

Overall, the analysis of the black solid was inconclusive and the composition of this compound remains unknown.

4.3.3 Route C

Reactions to form the partially oximated ligand **L2** were performed by using the same reagents as in the di-oxime **L1** synthesis, but in equimolar amounts. Anhydrous $MgSO_4$ was also added to each reaction to help drive the reaction to immediate completion by removing generated H_2O. The reactions were performed by slowly dropping solutions of hydroxylamine and **1c** into a large volume of solvent with the idea that diluting the reaction may reduce the chances of synthesising the di-oxime **L1**.

The $MgSO_4$ was difficult to remove from the product as it had become a very fine powder after stirring overnight. In the first reactions attempted, ^{1}H-NMR spectra was taken before the reaction yields were calculated. While the spectra indicated that the mono-oxime was present (Figure 42), the mass of product indicated yields significantly greater than 100%. The extra mass was attributed to the lingering fine $MgSO_4$ solid. The products from each reaction were re-dissolved in chloroform and several filtrations were conducted to remove the remaining $MgSO_4$ solid. Another ^{1}H-NMR spectra was taken for each reaction after removal

of the magnesium sulfate. These spectra greatly differed from the initial spectra, as the imine peaks (at 8.4 ppm) had split, indicating redistribution of the oxime groups had begun (Figure 43). This may be due to the acidity of $MgSO_4$, or due to the product reacting further in solution when the product was re-filtered. The spectra showed that the mono-oxime was still present, although in lower yield and purity.

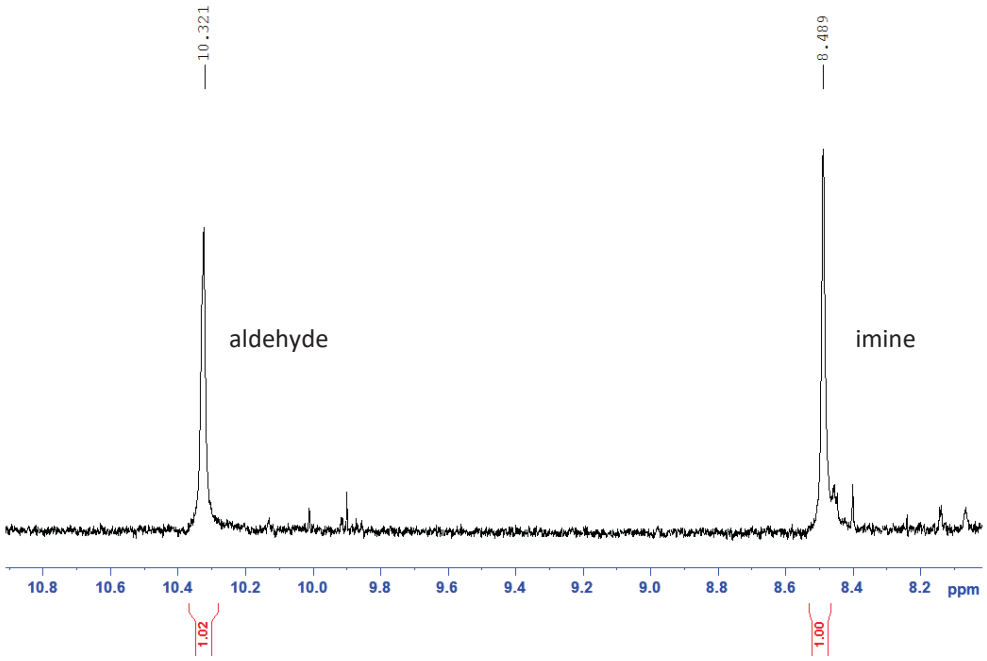

Figure 42. Selected peaks of the initial ^{1}H NMR spectrum of partially oximated ligand **L2**.

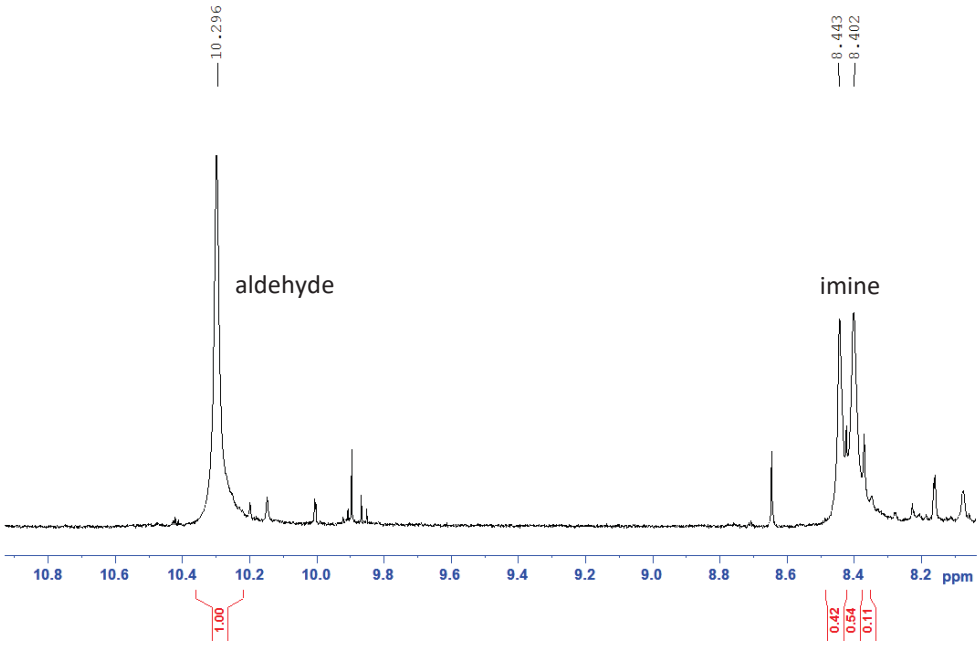

Figure 43. Selected peaks of the ^{1}H NMR spectrum of partially oximated ligand **L2** after filtering off the $MgSO_4$ solid.

All other reaction attempts showed a mixture of products based on ^{1}H NMR analysis. Each of the reaction products were set up for complexation reactions, as they contained the mono-oxime in a greater percentage than that in Willoughby's sample. The reaction solutions were brown. As in previous reaction routes, two attempts were made for each set of recrystallisations by slow diffusion of diethyl ether into an acetonitrile solution containing the crude reaction mixture.

None of the complexation reactions yielded crystals suitable for X-ray crystallographic analysis. The samples were left for approximately two weeks, until the colour was lost in the solution indicating full precipitation. A few of the vials had shown signs of crystal formation, but further attempts to form crystals had no success. The solid which precipitated out ranged from brown to black in colour.

ATR-IR analysis was collected for each solid sample to determine if it contained both the imine and aldehyde peaks, indicating it was a viable candidate for further analysis. All samples contained a weak imine peak in the range 1638.6 – 1631.0 cm^{-1}. Most samples contained an aldehyde peak in the range 1696.8 – 1692.5 cm^{-1}. As the aldehyde peak was significantly higher than the imine, it suggests that the aldehyde was not bound to manganese. CHN analysis was not performed on the samples as they were not viable candidates based on the IR analysis.

Around this time, a paper by Schmidt, Görls and Plass was published (August 2016) which presented a new straightforward synthetic route for unsymmetric double Schiff-base ligands.[69] This involved a two-step procedure, first isolating intermediate single Schiff-base precursor ligands derived from the condensation reactions of 2,6-diformyl-4-methylphenol with semicarbazide and thiosemicarbazide.[69] The unsymmetrical double Schiff-base ligands were then formed by reaction of the single Schiff-based precursors with different amine compounds. The synthesis gave the unsymmetrical double Schiff-base ligands in high yield and purity.[69] The starting material, 2,6-diformyl-cresol, was present in high concentration (0.378 mol L^{-1}) in the solvent acetonitrile in a round bottom flask. A fritted glass filter with pressure equaliser was fitted to the round bottomed flask and thiosemicarbazide placed on the frit. A condenser was then placed on top of the assembly, the temperature was set to 40°C, and the pressure was reduced. The pressure of the system was maintained at 240 mbar, causing the system to reflux. After a few minutes, a solid started to form. The reaction was

stopped after all solid starting material had eluted from above the frit. The desired single Schiff-base ligand was filtered off from the reaction mixture, yielding a yellow solid.[69]

The key idea for the synthesis of the single Schiff-base precursor ligand was the difference in solubilities between the starting material and the Schiff-base product. The starting material was significantly more soluble in the chosen solvent than the Schiff-base product. As the Schiff-base reaction proceeded, the single Schiff-base ligand was formed and precipitated out of solution due to the decrease in solubility.[69] This left the Schiff-base ligand unable to further react to form the double Schiff-base. Following the reaction, the solid was able to be filtered off, yielding the single Schiff-base in high purity.[69]

The ideas contained in this paper presented an alternative way to synthesise the mono-oxime **L2** from the di-aldehyde **1c**. Therefore the focus of the synthesis of **L2** was shifted from the high dilution reaction to the slow addition reaction under reduced pressure. Multiple attempts of this reaction were completed with the di-aldehyde **1c**, hydroxylamine hydrochloride and base in a 1:1:1 ratio. The base and solvent system was varied between reaction attempts.

The equipment was set up with a round-bottomed flask fitted to a fritted glass filter with pressure equaliser. A condenser was then placed on top of the assembly and a vacuum pump with a pressure control unit was attached at the top. The round-bottomed flask was placed in a temperature controlled oil bath (Appendix 6). For each reaction, the temperature was set to 40°C and the pressure was reduced until the solvent condensed above the solid on the frit. The reaction was then left to react for 2 days. The reaction conditions are given in table 14.

Table 14. Reaction conditions for the synthesis of **L2** by slow addition under low pressure.

Reaction	Solvent	Volume (mL)	Base	Temperature (°C)	Pressure (mbar)	Mass of 1c (g)
JKB-228	acetonitrile	20	Et_3N	40	230	0.15
JKB-229	1:1 ethanol : acetonitrile	200	Et_3N	40	185	0.50
JKB-234	ethanol	200	KOH	40	120	0.39
JKB-239	1:1 ethanol : acetonitrile	200	KOH	40	220	2.3
JKB-248	1:7 ethanol : acetonitrile	70	KOH	40	190	0.95
JKB-261	1:9 ethanol : dichloroethane	40	KOH	40	185	3.9

The first two reaction attempts (JKB-228 and JKB-229) to form **L2** by slow addition used triethylamine as a base. The round-bottomed flask contained **1c** and triethylamine in solution and hydroxylamine hydrochloride was placed on the frit. No solid formed from either reaction attempt and ^{1}H NMR analysis suggested that only starting material was present after two days. This suggested that the base was not strong enough to neutralise the hydroxylamine hydrochloride so that the hydroxylamine could react to form the oxime.

Potassium hydroxide was used as a base in the subsequent reactions, as this had proven a sufficient base in the synthesis of the di-oxime **L1**. For reactions JKB-234, JKB-239 and JKB-248, the round-bottomed flask contained **1c** and hydroxylamine hydrochloride in solution and potassium hydroxide was placed on the frit.

The reaction JKB-234 was performed in ethanol solvent. No solid formed from this reaction and ^{1}H NMR analysis suggested the solution contained a mixture of **1c**, **L1** and **L2**.

JKB-239 was performed in 1:1 ethanol/acetonitrile solvent and produced a solid (0.1010 g) which was filtered off and dissolved in deuterated DMSO. ^{1}H NMR analysis of product suggested that the mono-oxime **L2** had been successfully synthesised (Figure 44). However, CHN analysis indicated that most of the solid present (~96%) was potassium chloride salt, formed by the reaction of the hydroxylamine hydrochloride with the potassium hydroxide. In

an attempt to isolate **L2**, deuterated chloroform was then added to the sample and the solution was filtered. ^{1}H NMR analysis was not consistent with the previous spectrum (Figure 45). The sample was dried *in vacuo* and re-dissolved in DMSO, however this spectrum was not consistent with the first spectrum obtained (Figure 46). This suggested redistribution of the imine had occurred.

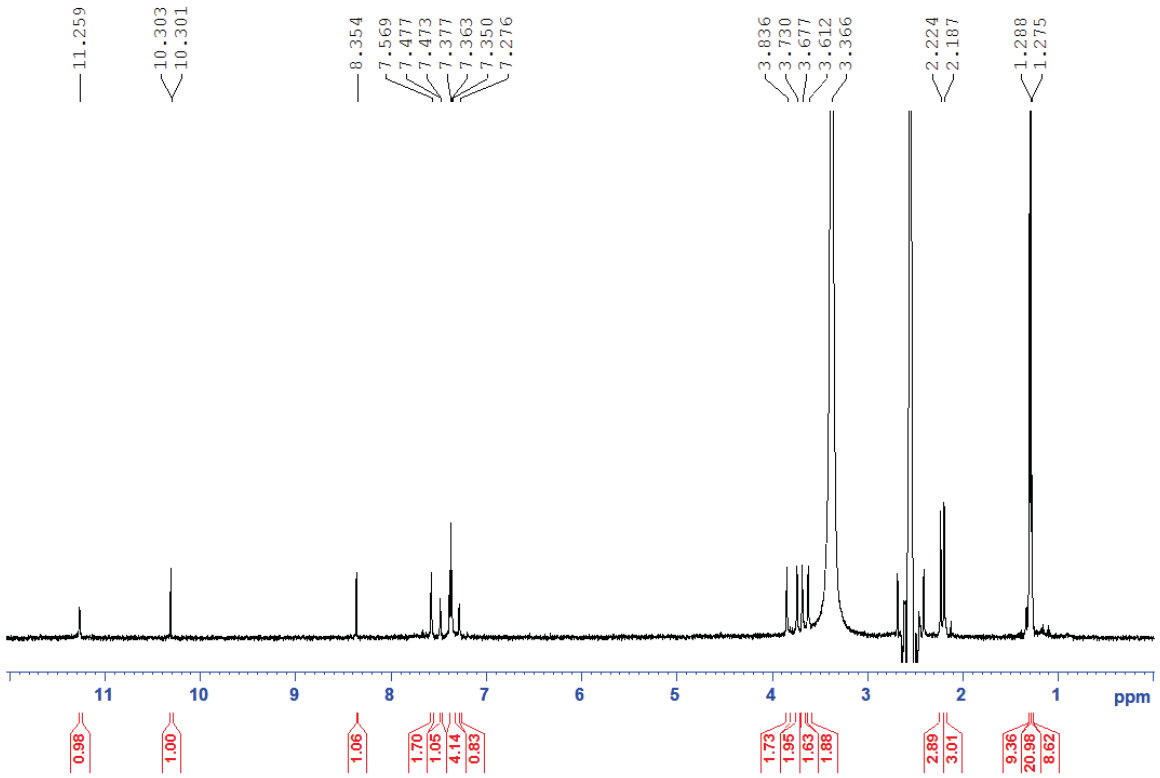

Figure 44. ^{1}H NMR spectrum of JKB-239 solid in DMSO.

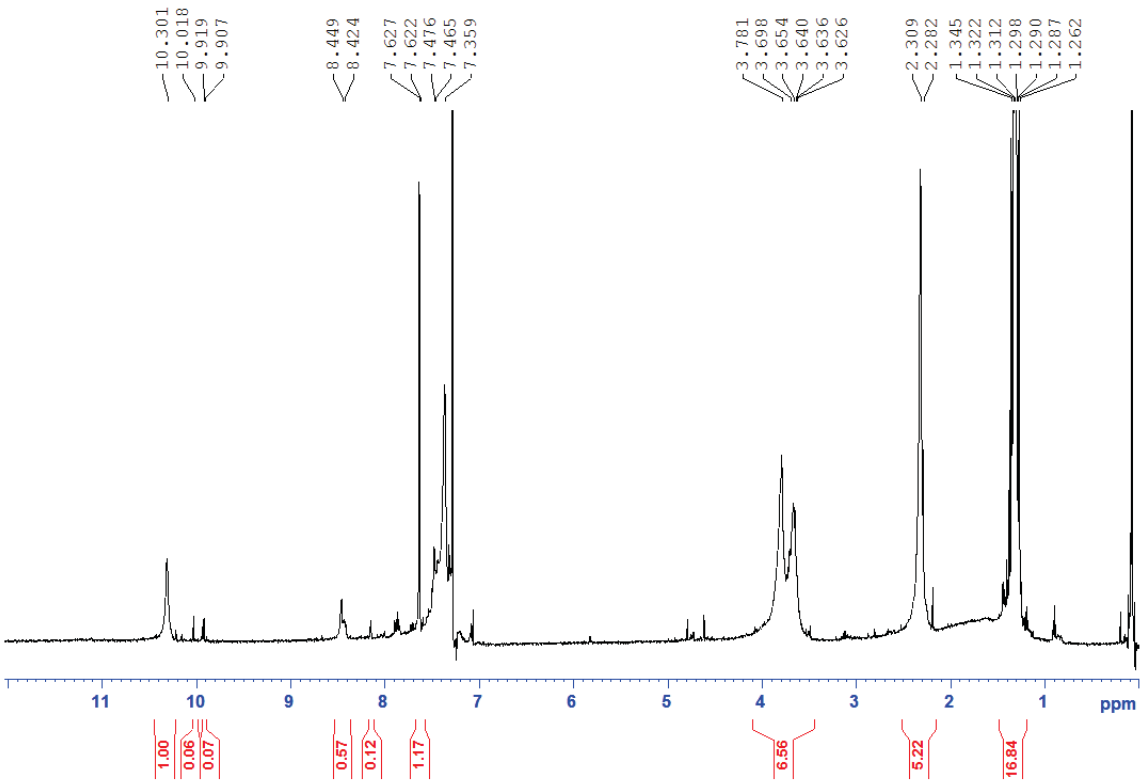

Figure 45. ^{1}H NMR spectrum of JKB-239 solid in $CDCl_3$.

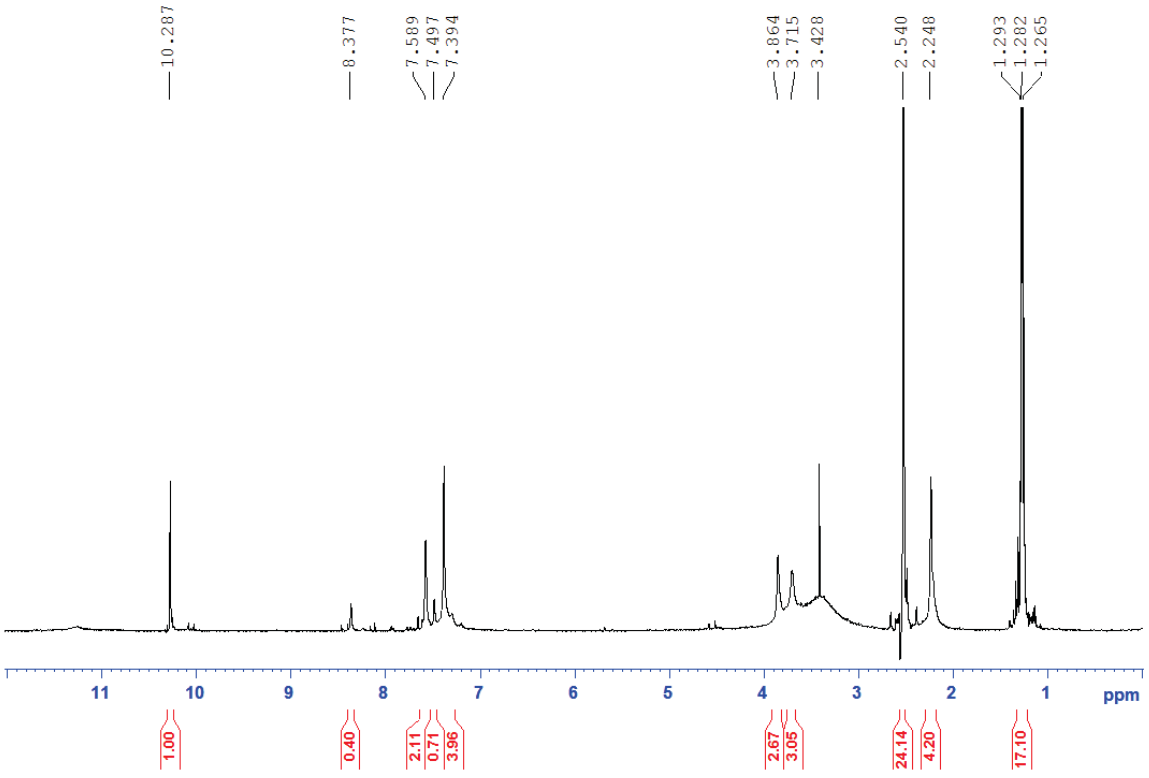

Figure 46. ^{1}H NMR spectrum of JKB-239 solid re-dissolved in DMSO.

Reaction JKB-248 also produced a solid (0.0757 g) which was filtered off and dissolved in deuterated DMSO. ^{1}H NMR analysis suggested that **L2** had been successfully synthesised (Figure 47). However, the solid mostly consisted of potassium chloride, similar to the previous reaction attempt.

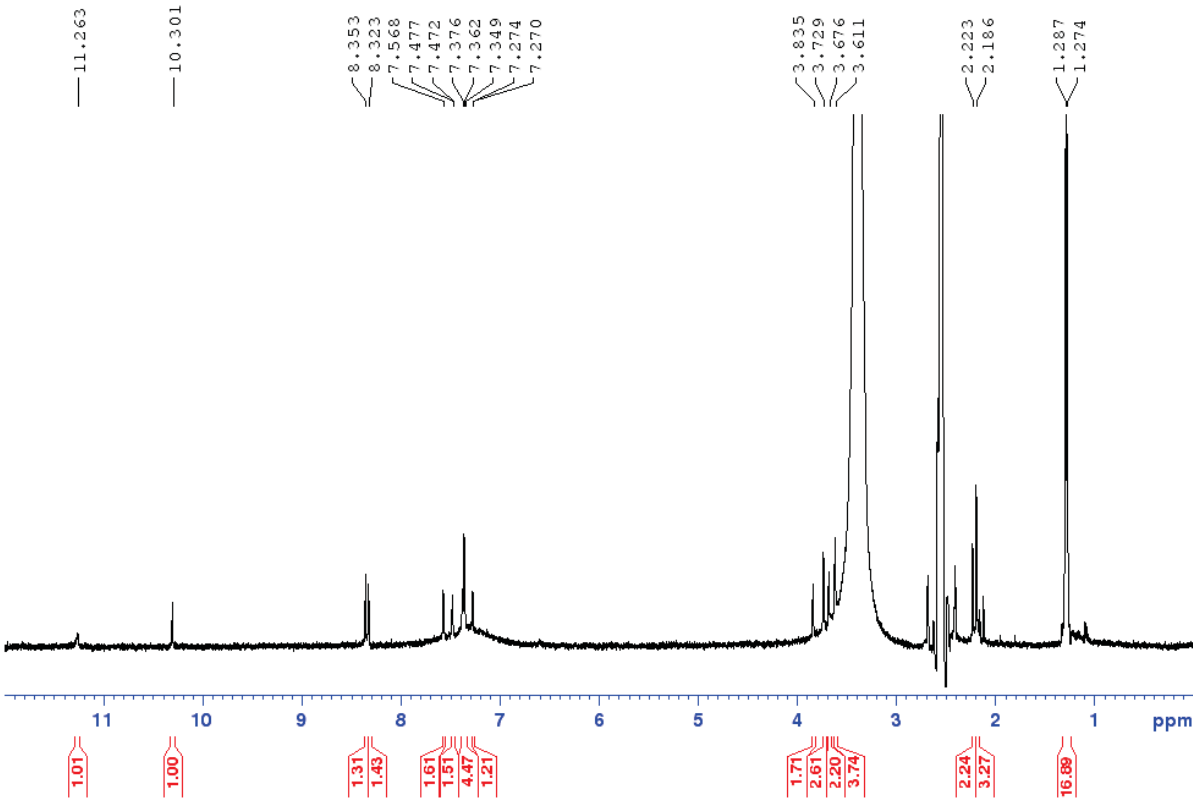

Figure 47. ^{1}H NMR spectrum of JKB-248 solid in DMSO.

For the subsequent series of reactions, the solvent conditions were modified to try and find a solvent system that would result in precipitation of the product.

For reaction JKB-261 the solvent was changed to 1:9 ethanol:dichloroethane due to the greater difference in solubilities of **1c** and **L2** in dichloroethane. Both potassium chloride and hydroxylamine hydrochloride were placed on the frit. As the solvent condensed above the frit, both reactants would dissolve and react forming the neutralised amine which would drip through leaving the KCl byproduct behind. After two days, a pale yellow solid had formed. This solid (0.2004 g) was filtered off and analysed using ^{1}H NMR. The ^{1}H NMR of the solid confirmed that the desired product had been successfully synthesised (Figures 48 and 49), but based on the ratio of the integrated imine and aldehyde peaks, the product contained ~14% impurity of **1c**.

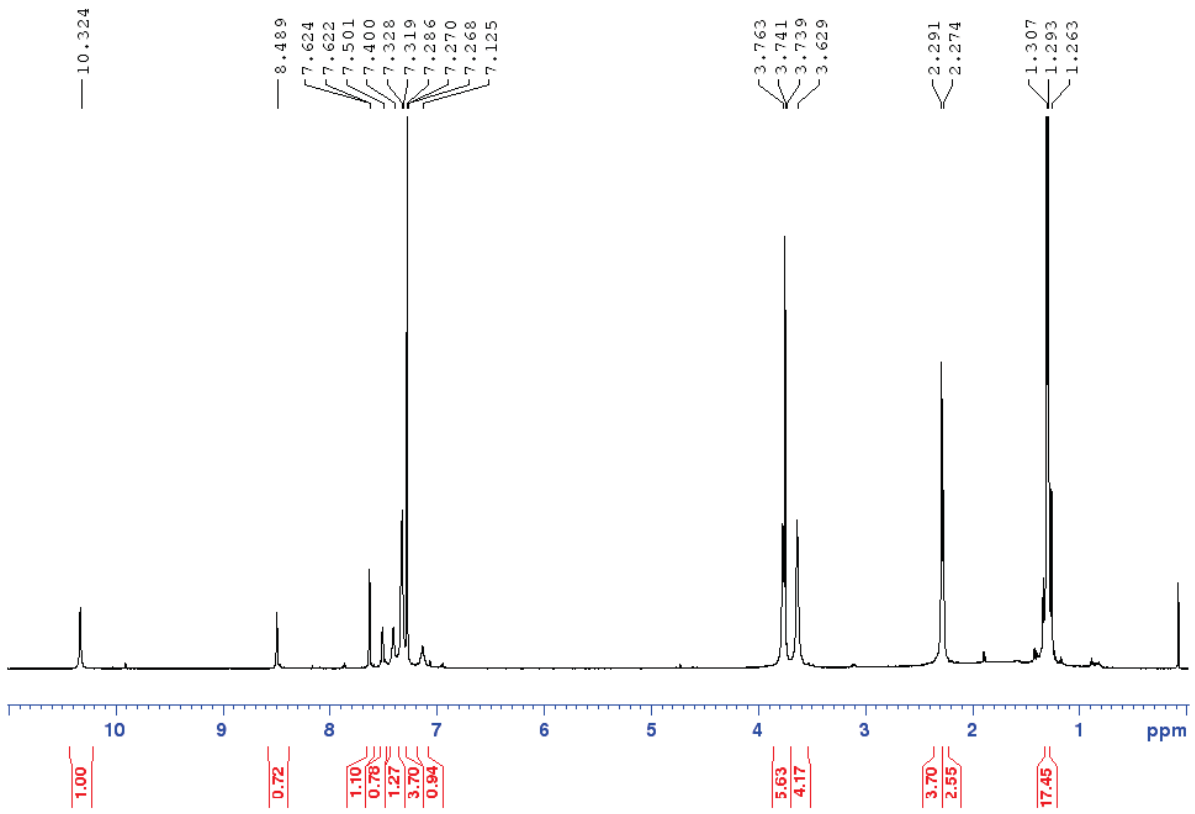

Figure 48. ^{1}H NMR spectrum of JKB-261 solid in $CDCl_3$.

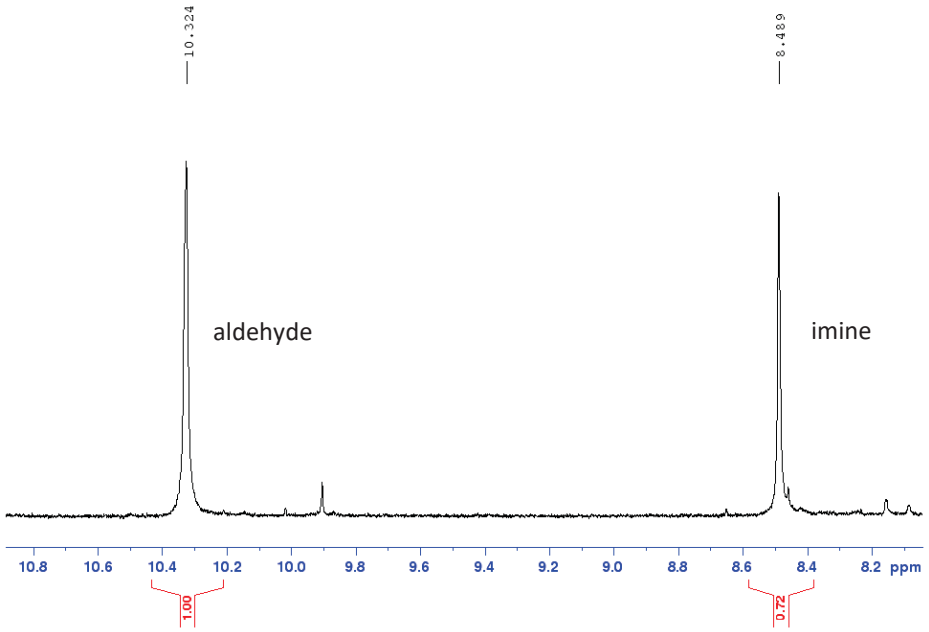

Figure 49. Selected peaks of the ^{1}H NMR spectrum of JKB-261 solid in $CDCl_3$.

One of the biggest constraints of the slow addition set-up for the synthesis of the mono-oxime **L1** was the amount of the starting material **1c** required for each reaction attempt. After this final reaction attempt, there was insufficient time left in the project to make more attempts at the synthesis of the mono-oxime ligand and the pursuit was abandoned.

4.3.4 Summary

There were many unsuccessful attempts to synthesise the di-manganese complex via the di-oxime **L2**, which suggested that route A was not viable. Route B, combining the oximation and complexation reactions, also proved unsuccessful. This route did yield a black solid which CHN analysis suggested was not the desired dinuclear complex. Many attempts at forming crystals from this solid were unsuccessful and the composition of this solid remains unknown.

If there were further attempts to synthesise the dinuclear manganese complex, the most promising method is likely to be route C, with synthesis of the mono-oxime ligand before complexation with manganese perchlorate. There were two methods which showed promise at yielding the mono-oxime: synthesis by high dilution or synthesis by slow addition at low pressure.

For the synthesis of **L2** by high dilution, future attempts could be made without the addition of anhydrous $MgSO_4$. This $MgSO_4$ was included to help drive the reaction to immediate completion by removing generated H_2O.

The most promising method for the synthesis of the mono-oxime is the slow addition of the oxime and base to a concentrated solution of **1c** at low pressure. This type of reaction has been shown to successfully yield an unsymmetric oxime on other types of ligands.[69] Three of the reaction attempts gave a ^1H NMR spectrum which was consistent with the synthesis of the mono-oxime. Two of these products were contaminated with potassium chloride, the third and final reaction attempt appeared to be contaminated by **1c**. Future reactions for the synthesis of the mono-oxime will be completed with 1:9 ethanol:dichloroethane as solvent, ensuring that the concentration of the starting material is as high as possible in order to induce precipitation of the mono-oxime **L2** before it is oximated to the di-oxime **L1**. Once **L1** has been synthesised, complexation reactions may yield the desired di-manganese complex. Unfortunately, time constraints prevented this method from being fully investigated.

4.4 Experimental Details

4.4.1 Synthesis of starting material

The literature scale was followed unless noted otherwise.

Synthesis of N,N'-dimethyl-*p*-xylylenediamine (1a)

Adapted and modified from Stevens and Plieger.[55]

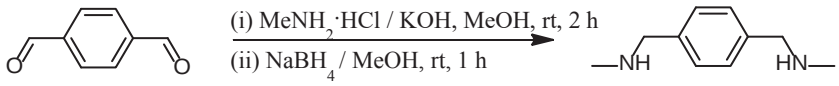

A solution of methylamine hydrochloride (3.180 g, 47.1 mmol) in methanol (60 mL) was allowed to mix with a solution of potassium hydroxide (2.804 g, 50.0 mmol) in methanol (60 mL). The filtered solution was slowly dripped into a second solution of terephthalaldehyde (2.115 g, 15.8 mmol) in methanol (80 mL) over 1h. The pale yellow solution was stirred at RT for 2 h. Sodium borohydride (1.409 g, 37.3 mmol) was added portion wise to the stirred solution over 10 minutes, which was then left to stir overnight. The solvent was removed under reduced pressure and the resulting white solid was dissolved in chloroform (70 mL) and washed with water (2 x 50 mL). The organic layer was separated and dried over anhydrous $MgSO_4$. The solvent was removed under reduced pressure and left under high vacuum overnight, leaving a yellow oil. Yields ranged from 1.747 – 2.233 g (67.4 – 81.9%). ^{1}H NMR analysis suggested that the desired product, N,N'-dimethyl-*p*-xylylenediamine, had been successfully synthesised. ^{1}H NMR ($CDCl_3$, 500MHz) δ 7.27 (4H, s, Ar-*H*), 3.73 (4H, s, CH_2), 2.45 (6H, s, C*H*$_3$), 1.35 (2H, br s, N*H*).

The synthesis of N,N'-dimethyl-*p*-xylylenediamine was also scaled up by a factor of two in comparison to the literature.[55] The product was synthesised in similar yield (4.401 g, 84.2%). ^{1}H NMR analysis confirmed that the desired product had been successfully synthesised.

Synthesis of 3-bromomethyl-5-*tert*-butylsalicylaldehyde (1b)

Adapted and modified from Wang *et al*.[70]

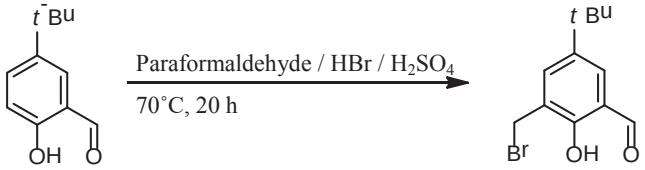

To a mixture of 2-hydroxy-5-*tert*-butyl-benzaldehyde (2.05 g, 11.5 mmol) and paraformaldehyde (0.502 g, 16.7 mmol), 48% HBr (13.7 g, 81.1 mmol) and several drops of conc. H_2SO_4 were slowly added over an ice bath. The mixture was then stirred at 70˚C for 20 h before it was allowed to cool to RT. Water (20 mL) was added to the mixture and the product was extracted into CH_2Cl_2 (20 mL). The product was then washed with water (20 mL). The organic phase was dried over anhydrous $MgSO_4$, filtered and the solvent removed under reduced pressure to give a pale yellow solid (2.792 g, 85.9%). ^{1}H NMR analysis suggested that the desired product had been successfully synthesised. ^{1}H NMR ($CDCl_3$, 500MHz) δ 11.33 (1H, s, O*H*), 9.91 (1H, s, C*H*=O), 7.65 (1H, d, J = 2.5 Hz, Ar-*H*), 7.52 (1H, d, J = 2.5 Hz, Ar-*H*), 4.60 (2H, s, CH_2Br), 1.35 (9H, s, CH_3).

The synthesis of 3-bromomethyl-5-*tert*-butylsalicylaldehyde was also scaled up by a factor of 3.5 in comparison to the literature.[70] The product was synthesised in similar yield (9.557 g, 88.3 %). When the synthesis was scaled up by a factor of four, the yield was 10.328 g (84.1%).

Synthesis of 3,3'-(1,4-phenylenebis(methylene))bis(ethylazanediyl)bis(methylene)bis(5-tert-butyl-2-hydroxybenzaldehyde) (1c)

Adapted and modified from Stevens and Plieger.[55]

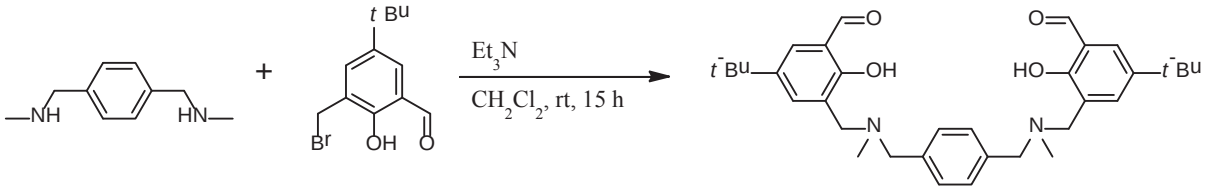

To a stirred solution of trimethylamine (1.316 g, 13.0 mmol) in dichloromethane (50 mL) were added simultaneously and slowly (over 1 h) solutions of N,N'-dimethyl-p-xylylenediamine (**1a**) (1.069 g, 6.5 mmol) in methanol/dichloromethane (1:20, 50 mL) and 3-(bromomethyl)-5-*tert*-butyl-2-hydroxybenzaldehyde (**1b**) (3.596 g, 13.3 mmol) in dichloromethane (50 mL). The resulting mixture was left to stir at RT overnight. The reaction was monitored for completion via ^{1}H NMR. The solvent was then evaporated to dryness to give a yellow solid, which was then redissolved in chloroform (80 mL). The organic layer was washed with water (3 x 30 mL), separated and dried over anhydrous $MgSO_4$. The solvent was removed under reduced pressure and dried under vacuum to give a bright yellow solid in quantitative yield. ^{1}H NMR analysis suggested that the desired product had been successfully synthesised. ^{1}H NMR ($CDCl_3$, 500MHz) δ 10.33 (2H, s, C*H*=O), 7.62 (2H, d, J = 2.8Hz, Ar-*H*), 7.39 (2H, s, Ar-*H*), 7.33 (4H, s, CH_2), 3.76 (4H, s, CH_2), 3.63 (4H, s, CH_2), 2.29 (6H, s, NCH_3), 1.31 (18H, s, C(CH_3)$_3$).

The synthesis of **1c** was also scaled up by a factor of two in comparison to the literature.[55] The product was successfully synthesised in quantitative yield. ^{1}H NMR analysis confirmed that the desired product had been successfully synthesised.

4.4.2 Route A: Synthesis via di-oxime L1

Synthesis of (1*E*,1'*E*)-5-*tert*-Butyl-3-(((4-(((5-*tert*-butyl-2-hydroxy-3-((*E*)(hydroxyimino) methyl)benzyl)(methyl)amino)methyl)benzyl)(methyl)amino)methyl)-2-hydroxybenzaldehyde oxime (L1)

Adapted and modified from Stevens and Plieger.[55]

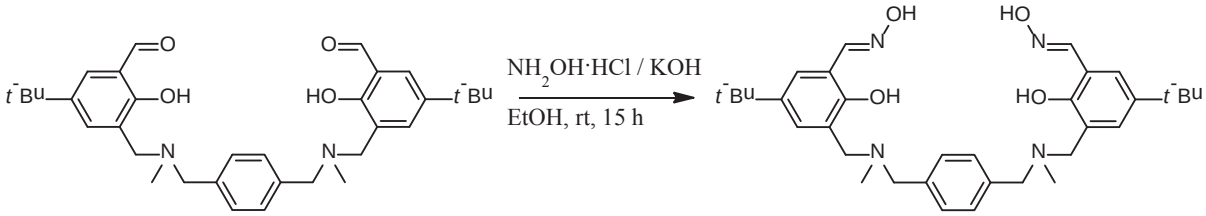

The synthesis of **L1** was scaled down by a factor of two in comparison to the literature. A solution of hydroxylamine hydrochloride (0.215 g, 3.09 mmol) in ethanol (30 mL) was added to a solution of potassium hydroxide (0.195 g, 3.46 mmol) in ethanol (30 mL). The resulting white precipitate was removed by filtration. The filtered solution was slowly dripped into a solution of **1c** (0.521 g, 0.096 mmol) in a chloroform / ethanol mix (1:6, 70 mL) over 1 h. The reaction mixture was then allowed to stir at RT overnight. The solvent was removed under reduced pressure, dissolved in chloroform (50 mL) and washed with water (2 x 10 mL). The organic layer was separated and dried over anhydrous $MgSO_4$, filtered and dried to give a yellow solid. The product was then recrystallised in hot ethanol to give a very pale yellow solid (0.337 g, 61.3%). ^{1}H NMR analysis suggested that the desired product had been successfully synthesised. ^{1}H NMR ($CDCl_3$, 500MHz) δ 8.45 (2H, s, C*H*NOH), 7.45 (2H, d, J = 2.3 Hz, Ar-*H*), 7.30 (4H, s, Ar-*H*), 7.11 (2H, d, J = 2.3 Hz, Ar-*H*), 3.73 (4H, s, CH_2), 3.61 (4H, s, CH_2), 2.26 (6H, s, NCH_3), 1.28 (18H, s, $C(CH_3)_3$).

The reaction was repeated on four times the scale above, twice the scale reported by Stevens and Plieger.[55] While ^{1}H NMR analysis suggested that the desired pure product had been successfully synthesised, there was a lower yield of 41.6% in comparison to the 61.3% yield obtained above and the 53% yield reported by Stevens and Plieger.[55]

General procedure for the formation of the dimetallic coordination compound

CAUTION! Whilst no problems were encountered in the course of this work, perchlorate mixtures are potentially explosive and should therefore be handled with appropriate care. To **L1** (0.050 g, 0.087 mmol) in acetonitrile (4 – 8 mL), $Mn(ClO_4)_2.XH_2O$ in acetonitrile (~2 mL) and sodium methoxide in methanol (0.5 mol L^{-1}) were added. Reaction conditions are

given in Table 15. The crude yields were typically 0.028 - 0.080 g. The solution was filtered and vials were set up for the slow diffusion of diethyl ether into a vial containing 1 mL of the sample in acetonitrile solution. The remaining sample was left to precipitate out of the mother liquor by slowly evaporating the solvent.

Table 15. Reaction conditions for complexations of **L1**.

Reaction Code	L1 : Mn : base ratio	~ Total Solvent volume (mL)	Reaction Time	Temp (°C)	Other notes
JKB-117	1:2:2	6	1 h	RT	
JKB-130	1:2:2	6	50 min	RT	
JKB-139	1:2:2	10	1 h	RT	
JKB-235	1:2:2	10	1 week	RT	
JKB-140	1:2:2	8	overnight	RT	
JKB-131	1:1:2	6	55 min	RT	
JKB-241	1:1:2	10	1 week	RT	
JKB-211	1:1:0	8	2 h	RT	
JKB-242	1:1:0	10	1 week	RT	
JKB-118	1:1:1	6	1 h	RT	
JKB-128	1:1:1	6	45 min	RT	
JKB-132	1:1:1	6	overnight	RT	
JKB-236	1:1:1	10	1 week	RT	
JKB-138	1:1:1	8	overnight	reflux	
JKB-146	1:1:1	10	1 h	RT	added 0.5 mL H_2O
JKB-144	1:1:1	8	1 h	RT	**L1** was doped with 2% **1c**
JKB-145	1:1:1	6	1 h	reflux	**L1** was doped with 2% **1c**
JKB-213	1:1:1	8	1 h	RT	**L1** was doped with 5% **1c**
JKB-214	1:1:1	8	1 h	RT	**L1** was doped with 10% **1c**
JKB-215	1:1:1	8	1 h	RT	**L1** was doped with 33% **1c**
JKB-216	1:1:1	8	1 h	RT	**L1** was doped with 50% **1c**

4.4.3 Route B: Combined oximation and complexation

To an acetonitrile solution (~100 mL) containing **1c** (0.10 g, 0.37 mmol), $Mn(ClO_4)_2 \cdot 6H_2O$ (0.13 g, 0.37 mmol) in acetonitrile (~8 mL) and base were added. A solution of hydroxylamine hydrochloride (0.025 g, 0.36 mmol) in ethanol (10 mL) was added to a solution of potassium hydroxide (0.20 g, 0.36 mmol) in ethanol (10 mL). The resulting white precipitate was removed by filtration. The filtered solution was slowly dripped into the solution containing **1c**, $Mn(ClO_4)_2 \cdot 6H_2O$ and base. The reaction was left stirring overnight. The solution was then reduced in volume to ~20 mL and vials set up for slow diffusion of diethyl ether into a vial containing 1 mL of the sample in solution. The remaining sample was left to precipitate out of the mother liquor by slowly evaporating the solvent.

Two of the reactions which showed promising results were duplicated and scaled up to produce more material for analysis.

Table 16. Reaction conditions for the Route B method.

Reaction Code	Mass of 1c (g)	Base	Oxime: Mn : 1c : base ratio	Reaction Time	Temp (°C)	Duplicates
JKB-217	0.10	-	1:1:1:0	overnight	RT	JKB-219
JKB-251	0.20	-	1:1:1:0	overnight	RT	JKB-253, JKB-256
JKB-218	0.10	MeONa	1:1:1:1	overnight	RT	
JKB-221	0.10	Et_3N	1:1:1:2	overnight	RT	JKB-222, JKB-230, JKB-267
JKB-225	0.20	Et_3N	1:1:1:2	overnight	RT	JKB-254, JKB-255, JKB-263
JKB-252	0.20	Et_3N	1:1:1:2	2 h	reflux	

4.4.4 Route C: Synthesis via mono-oxime L2

Synthesis of (1*E*,1'*E*)-5-*tert*-Butyl-3-(((4-(((5-*tert*-butyl-2-hydroxy-3-((*E*)(hydroxyimino) methyl)benzyl)(methyl)amino)methyl)benzyl)(methyl)amino)methyl)-2-hydroxybenzaldehyde (L2) by high dilution reaction

Adapted and modified from Stevens and Plieger.[55]

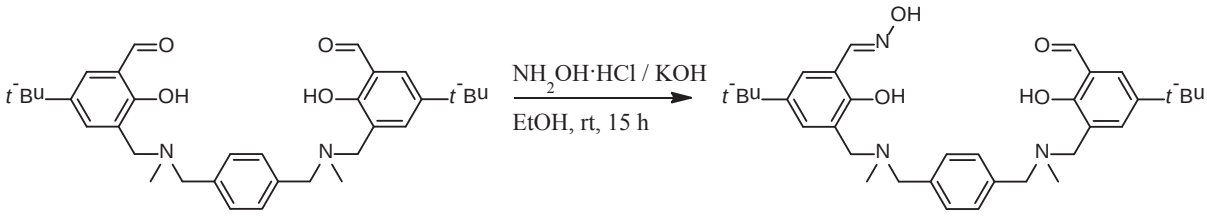

A solution of hydroxylamine hydrochloride (0.0118 g, 0.170 mmol) in ethanol (25 mL) was added to a solution of potassium hydroxide (0.0111 g, 0.198 mmol) in ethanol (25 mL). The resulting white precipitate was removed by filtration. **1c** (0.0939 g, 0.172 mmol) was dissolved in ethanol (50 mL). The two solutions were slowly dripped simultaneously into a round bottomed flask containing ethanol (100-500 mL) and anhydrous $MgSO_4$ over 2h. The reaction mixture was then allowed to stir at RT overnight. The solvent was removed under reduced pressure, dissolved in chloroform (50 mL) and washed with water (2 x 10 mL). The organic layer was separated and dried over anhydrous $MgSO_4$, filtered and dried to give a pale yellow solid (0.091 g, 94.3%).

Table 17. Reaction conditions for the synthesis of **L2** by Route C.

Reaction	Mass of 1c (g)	Total volume (mL)	$MgSO_4$ included
JKB-114	0.10	600	yes
JKB-126	0.10	600	yes
JKB-133	0.10	600	yes
JKB-142	0.10	300	yes
JKB-208	0.30	300	no

General procedure for the formation of the dimetallic coordination compound

CAUTION! Whilst no problems were encountered in the course of this work, perchlorate mixtures are potentially explosive and should therefore be handled with appropriate care. To **L2** (0.050 g, 0.089 mmol) in acetonitrile (4 – 8 mL), $Mn(ClO_4)_2.XH_2O$ in acetonitrile (~2

mL) and sodium methoxide in methanol (0.5 mol L^{-1}) were added. Reaction conditions are given in Table 18. The crude yields were typically 0.064 - 0.069 g. The solution was filtered and vials were set up for the slow diffusion of diethyl ether into a vial containing 1 mL of the sample in acetonitrile solution. The remaining sample was left to precipitate out of the mother liquor by slowly evaporating the solvent.

Table 18. Reaction conditions for complexations of **L2**.

Reaction Code	**L2 : Mn : base ratio**	**~ Total Solvent volume (mL)**	**Reaction Time**	Temp
JKB-115	1:1:1	14	overnight	RT
JKB-134	1:1:1	6	1 h	RT
JKB-135	1:1:1	6	1 h	reflux
JKB-136	1:1:1	6	1 h	RT
JKB-137	1:1:1	6	1 h	reflux
JKB-143	1:1:1	6	1 h	RT
JKB-209	1:1:1	8	1 h	RT
JKB-210	2:2:1	8	1 h	RT
JKB-212	1:1:0	8	1 h	RT

References

1. Aubin, S. M.; Sun, Z.; Eppley, H. J.; Rumberger, E. M.; Guzei, I. A.; Folting, K.; Gantzel, P. K.; Rheingold, A. L.; Christou, G.; Hendrickson, D. N., Single-Molecule Magnets: Jahn−Teller Isomerism and the Origin of Two Magnetization Relaxation Processes in Mn_{12} Complexes. *Inorg. Chem.* **2001,** *40* (9), 2127-2146.
2. Getzlaff, M., *Fundamentals of Magnetism*. Springer: Berlin Heidelberg, 2007; p 387.
3. Scott, R. T.; Parsons, S.; Murugesu, M.; Wernsdorfer, W.; Christou, G.; Brechin, E. K., Synthesis, structure and magnetic properties of a trinuclear $[Mn^{III}Mn^{II}_2]$ single-molecule magnet. *Chem. Commun.* **2005,** (16), 2083-2085.
4. Barros, W. P.; Inglis, R.; Nichol, G. S.; Rajeshkumar, T.; Rajaraman, G.; Piligkos, S.; Stumpf, H. O.; Brechin, E. K., From antiferromagnetic to ferromagnetic exchange in a family of oxime-based Mn^{III} dimers: a magneto-structural study. *Dalton Trans.* **2013,** *42* (47), 16510-16517.
5. Comar, P.; Rajeshkumar, T.; Nichol, G. S.; Pitak, M. B.; Coles, S. J.; Rajaraman, G.; Brechin, E. K., Switching the orientation of Jahn–Teller axes in oxime-based Mn^{III} dimers and its effect upon magnetic exchange: a combined experimental and theoretical study. *Dalton Trans.* **2015,** *44* (46), 19805-19811.
6. Houton, E.; Taylor, S. M.; Beedle, C. C.; Cano, J.; Piligkos, S.; Hill, S.; Ryder, A. G.; Brechin, E. K.; Jones, L. F., Ferromagnetic exchange in a twisted, oxime-bridged $[Mn^{III}_2]$ dimer. *Dalton Trans.* **2012,** *41* (27), 8340-8347.
7. Berg, N.; Rajeshkumar, T.; Taylor, S. M.; Brechin, E. K.; Rajaraman, G.; Jones, L. F., What Controls the Magnetic Interaction in bis-μ-Alkoxo Mn^{III} Dimers? A Combined Experimental and Theoretical Exploration. *Chem. Eur. J.* **2012,** *18* (19), 5906-5918.
8. Beghidja, C.; Rogez, G.; Kortus, J.; Wesolek, M.; Welter, R., Very Strong Ferromagnetic Interaction in a New Binuclear μ-Methoxo-Bridged Mn(III) Complex: Synthesis, Crystal Structure, Magnetic Properties, and DFT Calculations. *J. Am. Chem. Soc.* **2006,** *128* (10), 3140-3141.
9. Housecroft, C.; Sharpe, A. G., *Inorganic Chemistry*. 4th ed.; Pearson Education Limited: Harlow, 2012; p 1213.
10. Shriver, D. F.; Atkins, P., *Inorganic Chemistry*. 3rd ed.; Oxford University Press: New York, 1999; p 763.

11. (a) Pantazis, D. A.; Krewald, V.; Orio, M.; Neese, F., Theoretical magnetochemistry of dinuclear manganese complexes: broken symmetry density functional theory investigation on the influence of bridging motifs on structure and magnetism. *Dalton Trans.* **2010,** *39* (20), 4959-4967; (b) Retegan, M.; Collomb, M.-N.; Neese, F.; Duboc, C., A combined high-field EPR and quantum chemical study on a weakly ferromagnetically coupled dinuclear Mn(III) complex. A complete analysis of the EPR spectrum beyond the strong coupling limit. *Phys. Chem. Chem. Phys.* **2013,** *15* (1), 223-234.

12. (a) Burdett, J. K., Use of the Jahn-Teller theorem in inorganic chemistry. *Inorg. Chem.* **1981,** *20* (7), 1959-1962; (b) Jahn, H. A.; Teller, E., Stability of polyatomic molecules in degenerate electronic states. I. Orbital degeneracy. *Proc. R. Soc. Lon. Ser.-A* **1937,** *161* (A905), 220-235.

13. Freitag, R.; Conradie, J., Understanding the Jahn–Teller effect in octahedral transition-metal complexes: a molecular orbital view of the Mn(β-diketonato)$_3$ complex. *J. Chem. Ed.* **2013,** *90* (12), 1692-1696.

14. Halcrow, M. A., Jahn–Teller distortions in transition metal compounds, and their importance in functional molecular and inorganic materials. *Chem. Soc. Rev.* **2013,** *42* (4), 1784-1795.

15. Halcrow, M. A., Interpreting and controlling the structures of six-coordinate copper(II) centres–When is a compression really a compression? *Dalton Trans.* **2003,** (23), 4375-4384.

16. Fitzpatrick, A.; Stepanovic, S.; Müller-Bunz, H.; Gruden-Pavlović, M.; García-Fernández, P.; Morgan, G., Challenges in assignment of orbital populations in a high spin manganese(III) complex. *Dalton Trans.* **2016,** *45* (15), 6702-6708.

17. Dimitrakopoulou, A.; Psycharis, V.; Raptopoulou, C. P.; Terzis, A.; Tangoulis, V.; Kessissoglou, D. P., Novel mixed-valence manganese cluster with two distinct Mn$_3$(II/III/II) and Mn$_3$(III/II/III) trinuclear units in a pseudocubane-like arrangement. *Inorg. Chem.* **2008,** *47* (17), 7608-7614.

18. De Munno, G.; Julve, M.; Lloret, F.; Cano, J.; Caneschi, A., Magneto-structural effects of the Jahn-Teller distortions on 2,2'-Bipyrimidine-, (bpm-) bridged dinuclear copper(II) complexes: crystal structures and magnetic properties of [Cu$_2$(bpm)(H$_2$O)$_4$(SO$_4$)$_2$].3H$_2$O and [Cu$_2$(bpm)(H$_2$O)$_8$](SO$_4$)$_2$.2H$_2$O. *Inorg. Chem.* **1995,** *34* (8), 2048-2053.

19. Clemens, O.; Haberkorn, R.; Kohlmann, H.; Springborg, M.; Beck, H. P., Synthesis and characterization of the new mixed valent compound Mn_5VO_8. *Z. Anorg. Allg. Chem.* **2012,** *638* (7-8), 1134-1140.

20. Wandner, K.-H.; Hoppe, R., Jahn-Teller effect in manganese(III) fluorides: calcium manganese fluoride ($CaMnF_5$). *Rev. Chim. Miner.* **1986,** *23* (45), 520-31.

21. (a) Armbruster, T.; Oberhaensli, R.; Kunz, M., Taikanite, $BaSr_2Mn^{3+}{}_2O_2[Si_4O_{12}]$, from the Wessels mine, South Africa: a chain silicate related to synthetic $Ca_3Mn^{3+}{}_2O_2[Si_4O_{12}]$. *Am. Mineral.* **1993,** *78* (9-10), 1088-1095; (b) Moore, P. B.; Araki, T., Crystal structure of synthetic $Ca_3Mn^{3+}{}_2O_2[Si_4O_{12}]$*. *Z. Kristallogr. NCS* **1979,** *150* (1-4), 287; (c) Moore, P. B.; Gupta, P. K. S.; Jinchuan, S.; Schlemper, E. O., The kentrolite-melanotekite series, $4Pb_2(Mn,Fe)^{3+}{}_2O_2[Si_2O_7]$; chemical crystallographic relations, lone-pair splitting, and cation relation to $8URe_2$. *Am. Mineral.* **1991,** *76* (7-8), 1389-1399.

22. Alekseeva, A. M.; Abakumov, A. M.; Rozova, M. G.; Antipov, E. V.; Hadermann, J., Synthesis and crystal structure of the $Sr_2MnGa(O,F)_6$ oxyfluorides. *J. Solid State Chem.* **2004,** *177* (3), 731-738.

23. Goubard, F.; Chassaing, J.; Bizot, D.; Quarton, M., Synthesis, structural and spectroscopic studies of $Cr^{II}Nb^{IV}F_6$. *Eur. J. Solid State Inorg. Chem.* **1994,** *31* (3), 223-33.

24. Inaguma, Y.; Iwanaga, D.; Itoh, M.; Aizawa, K.; Shimojo, Y.; Morii, Y., Structure and properties of perovskite-related transition-metal oxides. *JAERI-Review* **1997,** (97-012), 11.

25. Crama, W.; Maaskant, W.; Verschoor, G., The cooperative Jahn–Teller distorted structures of rubidium chromium (II) trichloride and caesium chromium (II) trichloride. *Acta Cryst.* **1978,** *B34* (6), 1973-1974.

26. Corbella, M.; Costa, R.; Ribas, J.; Fries, P. H.; Latour, J.-M.; Öhrström, L.; Solans, X.; Rodríguez, V., Structural and Magnetization Studies of a New (μ-Oxo)bis(μ-carboxylato)dimanganese(III) Complex with a Terminal Hydroxo Ligand. *Inorg. Chem.* **1996,** *35* (7), 1857-1865.

27. Hotzelmann, R.; Wieghardt, K.; Floerke, U.; Haupt, H. J.; Weatherburn, D. C.; Bonvoisin, J.; Blondin, G.; Girerd, J. J., Spin exchange coupling in asymmetric heterodinuclear complexes containing the μ-oxo-bis(μ-acetato)dimetal core. *J. Am. Chem. Soc.* **1992,** *114* (5), 1681-1696.

28. Anderlund, M. F.; Zheng, J.; Ghiladi, M.; Kritikos, M.; Rivière, E.; Sun, L.; Girerd, J.-J.; Åkermark, B., A new, dinuclear high spin manganese(III) complex with bridging phenoxy and methoxy groups. Structure and magnetic properties. *Inorg. Chem. Commun.* **2006,** *9* (12), 1195-1198.
29. Young, D., *Computational chemistry: a practical guide for applying techniques to real world problems*. John Wiley & Sons: New York, 2004; p 381.
30. Van der Maelen Uria, J. F.; Ruiz, J.; Garcia-Granda, S., Theoretical versus experimental geometries in S-bridged manganese carbonyl complexes. *J. Appl. Crystallogr.* **2003,** *36* (4), 1050-1055.
31. Stephens, P. J.; Devlin, F. J.; Chabalowski, C. F.; Frisch, M. J., Ab Initio Calculation of Vibrational Absorption and Circular Dichroism Spectra Using Density Functional Force Fields. *J. Phys. Chem.* **1994,** *98* (45), 11623-11627.
32. Koch, W.; Holthausen, M. C., *A chemist's guide to density functional theory*. John Wiley & Sons: 2015; p 300.
33. Becke, A. D., Density-functional thermochemistry. III. The role of exact exchange. *J. Chem. Phys* **1993,** *98* (7), 5648-5652.
34. Becke, A. D., Density-functional exchange-energy approximation with correct asymptotic behavior. *Phys. Rev. A* **1988,** *38* (6), 3098.
35. Vosko, S. H.; Wilk, L.; Nusair, M., Accurate spin-dependent electron liquid correlation energies for local spin density calculations: a critical analysis. *Can. J. Phys* **1980,** *58* (8), 1200-1211.
36. Lee, C.; Yang, W.; Parr, R. G., Development of the Colle-Salvetti correlation-energy formula into a functional of the electron density. *Phys. Rev. B* **1988,** *37* (2), 785.
37. Foresman, J. B.; Frisch, Æ., *Exploring chemistry with electronic structure methods: a guide to using Gaussian*. 3rd ed.; Gaussian, Inc.: Wallingford, CT, 2015; p 531.
38. Hariharan, P. C.; Pople, J. A., The influence of polarization functions on molecular orbital hydrogenation energies. *Theoret. Chim. Acta (Berl.)* **1973,** *28* (3), 213-222.
39. Davidson, E. R.; Feller, D., Basis set selection for molecular calculations. *Chem. Rev.* **1986,** *86* (4), 681-696.
40. (a) Hay, P. J.; Wadt, W. R., Ab initio effective core potentials for molecular calculations. Potentials for the transition metal atoms Sc to Hg. *J. Chem. Phys.* **1985,** *82* (1), 270-283; (b) Hay, P. J.; Wadt, W. R., Ab initio effective core potentials for molecular calculations. Potentials for K to Au including the outermost core orbitals. *J. Chem. Phys.* **1985,** *82* (1), 299-310; (c) Yang, Y.; Weaver, M. N.; Merz Jr, K. M.,

Assessment of the "6-31+G** + LANL2DZ" mixed basis set coupled with density functional theory methods and the effective core potential: prediction of heats of formation and ionization potentials for first-row-transition-metal complexes. *J. Phys. Chem. A* **2009,** *113* (36), 9843-9851.

41. Biswas, S.; Kar, T.; Sarkar, S.; Dey, K., Synthesis, characterization, and density functional study of some manganese(III) Schiff-base complexes. *J. Coord. Chem.* **2012,** *65* (6), 980-993.
42. Foresman, J. B.; Frisch, *Æ.*, *Exploring chemistry with electronic structure methods: a guide to using Gaussian*. 2nd ed.; Gaussian, Inc.: Pittsburgh, PA, 1996; p 302.
43. McGrady, J. E.; Stranger, R., Redox-Induced Formation and Cleavage of O− O σ and π Bonds in a Peroxo-Bridged Manganese Dimer: A Density Functional Study. *Inorg. Chem.* **1999,** *38* (3), 550-558.
44. McGrady, J. E.; Stranger, R., Redox-induced changes in the geometry and electronic structure of di-μ-oxo-bridged manganese dimers. *J. Am. Chem. Soc.* **1997,** *119* (36), 8512-8522.
45. Noodleman, L., Valence bond description of antiferromagnetic coupling in transition metal dimers. *J. Chem. Phys* **1981,** *74* (10), 5737-5743.
46. Ruiz, E.; Cano, J.; Alvarez, S.; Alemany, P., Broken symmetry approach to calculation of exchange coupling constants for homobinuclear and heterobinuclear transition metal complexes. *J. Comput. Chem.* **1999,** *20* (13), 1391-1400.
47. (a) Soda, T.; Kitagawa, Y.; Onishi, T.; Takano, Y.; Shigeta, Y.; Nagao, H.; Yoshioka, Y.; Yamaguchi, K., Ab initio computations of effective exchange integrals for H–H, H–He–H and Mn_2O_2 complex: comparison of broken-symmetry approaches. *Chem. Phys. Lett.* **2000,** *319* (3–4), 223-230; (b) Yamaguchi, K.; Takahara, Y.; Fueno, T., Ab-Initio Molecular Orbital Studies of Structure and Reactivity of Transition Metal-oxo Compounds. In *Applied Quantum Chemistry: Proceedings of the Nobel Laureate Symposium on Applied Quantum Chemistry in Honor of G. Herzberg, R. S. Mulliken, K. Fukui, W. Lipscomb, and R. Hoffman, Honolulu, HI, 16–21 December 1984*, Smith, V. H.; Schaefer, H. F.; Morokuma, K., Eds. Springer Netherlands: Dordrecht, 1986; pp 155-184.
48. Inglis, R.; Houton, E.; Liu, J.; Prescimone, A.; Cano, J.; Piligkos, S.; Hill, S.; Jones, L. F.; Brechin, E. K., Accidentally on purpose: construction of a ferromagnetic, oxime-based $[Mn^{III}_2]$ dimer. *Dalton Trans.* **2011,** *40* (39), 9999-10006.

49. Barone, V.; Bencini, A.; Gatteschi, D.; Totti, F., DFT Description of the Magnetic Properties and Electron Localization in Dinuclear Di-μ-oxo-Bridged Manganese Complexes. *Chem. Eur. J.* **2002,** *8* (21), 5019-5027.

50. Sameera, W.; McKenzie, C. J.; McGrady, J. E., On the mechanism of water oxidation by a bimetallic manganese catalyst: a density functional study. *Dalton Trans.* **2011,** *40* (15), 3859-3870.

51. Gostynski, R.; van Rooyen, P. H.; Conradie, J., Jahn-Teller distortion in tris [4,4,4-trifluoro-1-(2-thienyl)-1,3-butanedionato]manganese(III) isomers: An X-ray and computational study. *J. Mol. Struct.* **2016,** *1119*, 48-53.

52. Ouyang, C.; Shi, S.; Lei, M., Jahn–Teller distortion and electronic structure of $LiMn_2O_4$. *J. Alloys Compd.* **2009,** *474* (1), 370-374.

53. Willoughby, A., Hons. dissertation, Massey University. **2011**, pgs 38.

54. Brechin, E., Personal Communication. 2013.

55. Stevens, J. R.; Plieger, P. G., Anion-driven conformation control and enhanced sulfate binding utilising aryl linked salicylaldoxime dicopper helicates. *Dalton Trans.* **2011,** *40* (45), 12235-12241.

56. Groom, C. R.; Bruno, I. J.; Lightfoot, M. P.; Ward, S. C., The Cambridge structural database. *Acta Cryst.* **2016,** *B72*, 171-179

57. (a) Biava, H. n.; Palopoli, C.; Duhayon, C.; Tuchagues, J.-P.; Signorella, S., Synthesis, Structure, and Catalase-Like Activity of Dimanganese(III) Complexes of 1,5-Bis[(2-hydroxy-5-X-benzyl)(2-pyridylmethyl)amino]pentan-3-ol (X= H, Br, OCH_3). *Inorg. Chem.* **2009,** *48* (7), 3205-3214; (b) Mukherjee, P.; Kar, P.; Ianelli, S.; Ghosh, A., Isolation of a novel intermediate during unsymmetrical to symmetrical rearrangement of a tetradentate Schiff base ligand in a manganese (III) complex: Catalytic activity of the rearranged product towards alkene epoxidation. *Inorg. Chim. Acta.* **2011,** *365* (1), 318-324.

58. Orchard, A. F., *Magnetochemistry*. Oxford University Press: Oxford, UK, 2003; p 172.

59. Neese, F., Prediction of molecular properties and molecular spectroscopy with density functional theory: from fundamental theory to exchange-coupling. *Coord. Chem. Rev.* **2009,** *253* (5), 526-563.

60. Neese, F., Definition of corresponding orbitals and the diradical character in broken symmetry DFT calculations on spin coupled systems. *J. Phys. Chem. Solids* **2004,** *65* (4), 781-785.

61. Chemcraft version 1.8 build 523. https://www.chemcraftprog.com.
62. McGrady, J., Personal Communication. June/July 2017.
63. McGrady, J., Personal Communication. February 2017.
64. Swart, M.; Costas, M., *Spin States in Biochemistry and Inorganic Chemistry: Influence on Structure and Reactivity*. Wiley: 2015.
65. Stuart, B. H., *Infrared Spectroscopy: Fundamentals and Applications*. Wiley: 2004; p 224.
66. Nakamoto, K., *Infrared and Raman Spectra of Inorganic and Coordination Compounds, Applications in Coordination, Organometallic, and Bioinorganic Chemistry*. 5th ed.; Wiley: 1997; p 384.
67. Das, G.; Shukla, R.; Mandal, S.; Singh, R.; Bharadwaj, P. K.; van Hall, J.; Whitmire, K. H., Syntheses and X-ray structures of mixed-ligand salicylaldehyde complexes of Mn(III), Fe(III), and Cu(II) ions: Reactivity of the Mn(III) complex toward primary monoamines and catalytic epoxidation of olefins by the Cu(II) complex. *Inorg. Chem.* **1997,** *36* (3), 323-329.
68. Brooker, S.; de Geest, D. J.; Kelly, R. J.; Plieger, P. G.; Moubaraki, B.; Murray, K. S.; Jameson, G. B., Exchange-coupled high-spin, low-spin and spin-crossover dicobalt(II) complexes of a pyridazine-containing Schiff-base macrocycle: control of cobalt(II) spin state by choice of axial ligands. *J. Chem. Soc., Dalton Trans.* **2002,** (9), 2080-2087.
69. Schmidt, M.; Gorls, H.; Plass, W., Facile high-yield synthesis of unsymmetric end-off compartmental double Schiff-base ligands: easy access to mononuclear precursor and unsymmetric dinuclear complexes. *RSC Adv.* **2016,** *6* (79), 75844-75854.
70. Wang, Q.; Wilson, C.; Blake, A. J.; Collinson, S. R.; Tasker, P. A.; Schröder, M., The one-pot halomethylation of 5-substituted salicylaldehydes as convenient precursors for the preparation of heteroditopic ligands for the binding of metal salts. *Tetrahedron Lett.* **2006,** *47* (50), 8983-8987.

Appendix 1: Examples of input files

Example *.com* file (for use on the CTCP cluster)

```
$RunGauss$

%oldchk=Mn_dimer_ub3lyp_singlet_631+Gdp_Lanl2dz_fragment.chk
%chk=Mn_dimer_ub3lyp_singlet_631+Gdp_Lanl2dz_fragment_opt.chk
%nprocshared=16
%mem=126GB
# opt ub3lyp/genecp scf=xqc int=ultrafine nosymm guess=read
geom=check

Mn_dimer_ub3lyp_singlet_631+Gdp_Lanl2dz_fragment_opt

4 1 0 1 0 1 3 5 3 -5 -1 1 -1 1

Mn 0
LANL2DZ
****
C N O H 0
6-31+g(d,p)
****

Mn 0
LANL2

1-1632
1-1632
```

Note that the Mn_dimer_ub3lyp_singlet_631+Gdp_Lanl2dz_fragment.chk file contains the connectivities.

Example submission file (for use on the CTCP cluster)

```
#!/bin/bash

#SBATCH --job-name
Mn_dimer_ub3lyp_singlet_631+Gdp_Lanl2dz_fragment_opt.com
#SBATCH --mail-type     ALL
#SBATCH --mail-user     j.k.buchanan@massey.ac.nz
#SBATCH --time          20-00:00:00
#SBATCH --cpus-per-task 16
#SBATCH --mem-per-cpu   8192
#SBATCH --output
Mn_dimer_ub3lyp_singlet_631+Gdp_Lanl2dz_fragment_opt.%j.out #
Include the job ID in the names of the
#SBATCH --error
Mn_dimer_ub3lyp_singlet_631+Gdp_Lanl2dz_fragment_opt.err # output
and error files
#SBATCH --partition     long

module load gaussian/intel/EM64T/SSE4_2-enabled/binary/G09_Rev_D.01
source $g09root/g09/bsd/g09.profile

echo "This job was submitted from the computer:"
echo "$SLURM_SUBMIT_HOST"
echo "and the directory:"
echo "$SLURM_SUBMIT_DIR"
echo ""
echo "It is running on the compute node:"
echo "$SLURM_CLUSTER_NAME"
echo ""
echo "The local scratch directory (located on the compute node) is:"
echo "$SCRATCH"
echo ""

export GAUSS_SCRDIR=$SCRATCH
if [ ! -e $GAUSS_SCRDIR ]; then mkdir $GAUSS_SCRDIR; fi

# Execute the program
g09 <
/home/buchanan/Mn_dimer_ub3lyp_singlet_631+Gdp_Lanl2dz_fragment/
Mn_dimer_ub3lyp_singlet_631+Gdp_Lanl2dz_fragment_opt.com >
/home/buchanan/Mn_dimer_ub3lyp_singlet_631+Gdp_Lanl2dz_fragment/
Mn_dimer_ub3lyp_singlet_631+Gdp_Lanl2dz_fragment_opt.log
```

Generate *.fchk* and *.cub* (on the workstation)

Generate *.fchk* file

In the terminal:
cd gaussian
ls
cd g09
'./formchk [name].chk'

This will output the formatted checkpoint file *[name].fchk* to the same directory as the *.chk* file.

Generate *.cub* file

In the terminal:
cd gaussian
ls
cd g09
./cubegen 0 spin=scf '[name].fchk' '[name].cub' -4 h

spin=scf specifies that a spin density (difference between α and β spin densities) be generated
0 is an old memory flag (defaults to 1 processor)
-4 denotes fine grid
h adds headers to the output file

In order to view molecular orbitals in Gaussview, a cube file for molecular orbitals can be generated by specifying *MO=n* (where *n* specifies the molecular orbitals to be generated) instead of *spin=scf.*

Appendix 2: Molecular orbitals

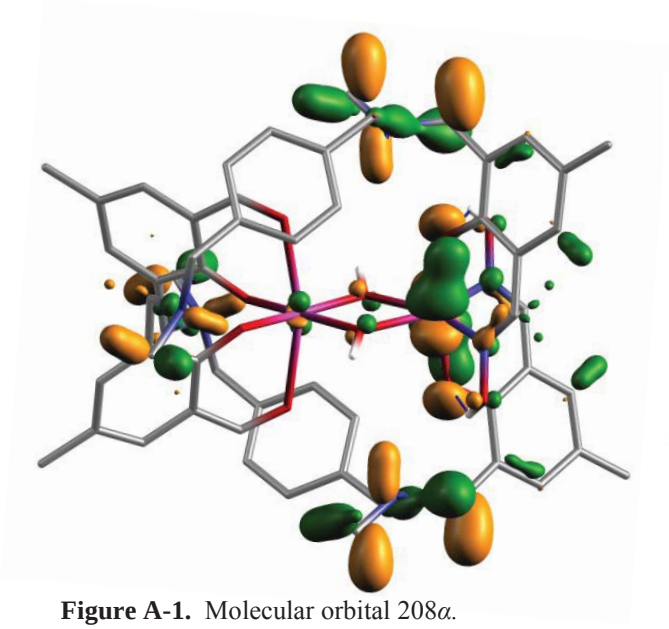

Figure A-1. Molecular orbital 208*α*.

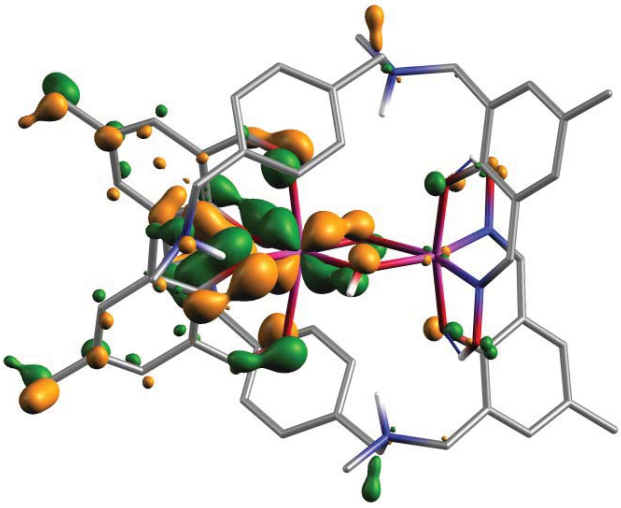

Figure A-2. Molecular orbital 221*α*.

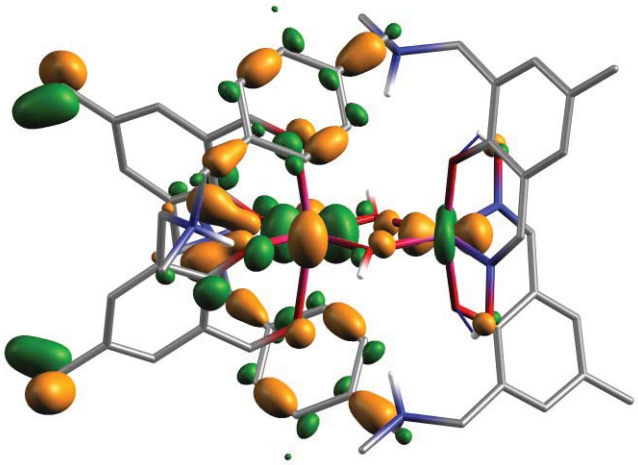

Figure A-3. Molecular orbital 235*α*.

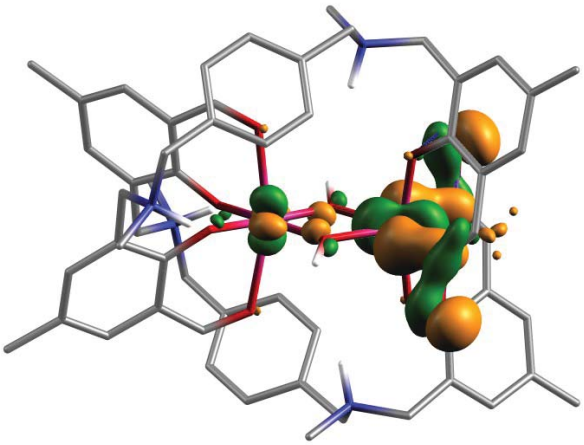

Figure A-4. Molecular orbital 236*α*.

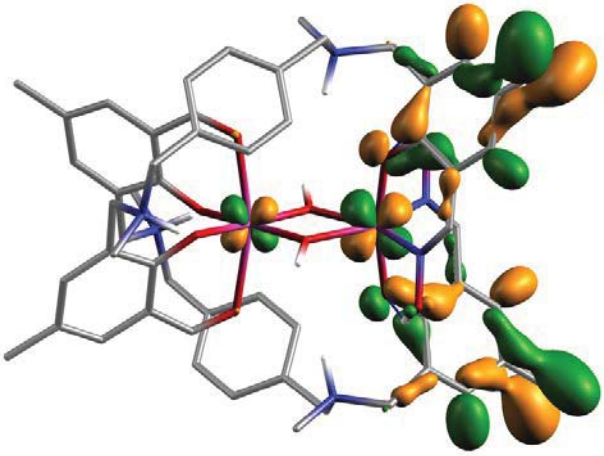

Figure A-5. Molecular orbital 240*α*.

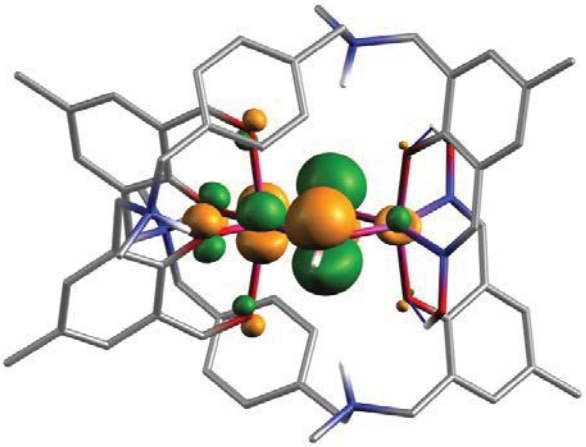

Figure A-6. Molecular orbital 265*α*.

Appendix 3: Assigned ^{1}H NMR spectra

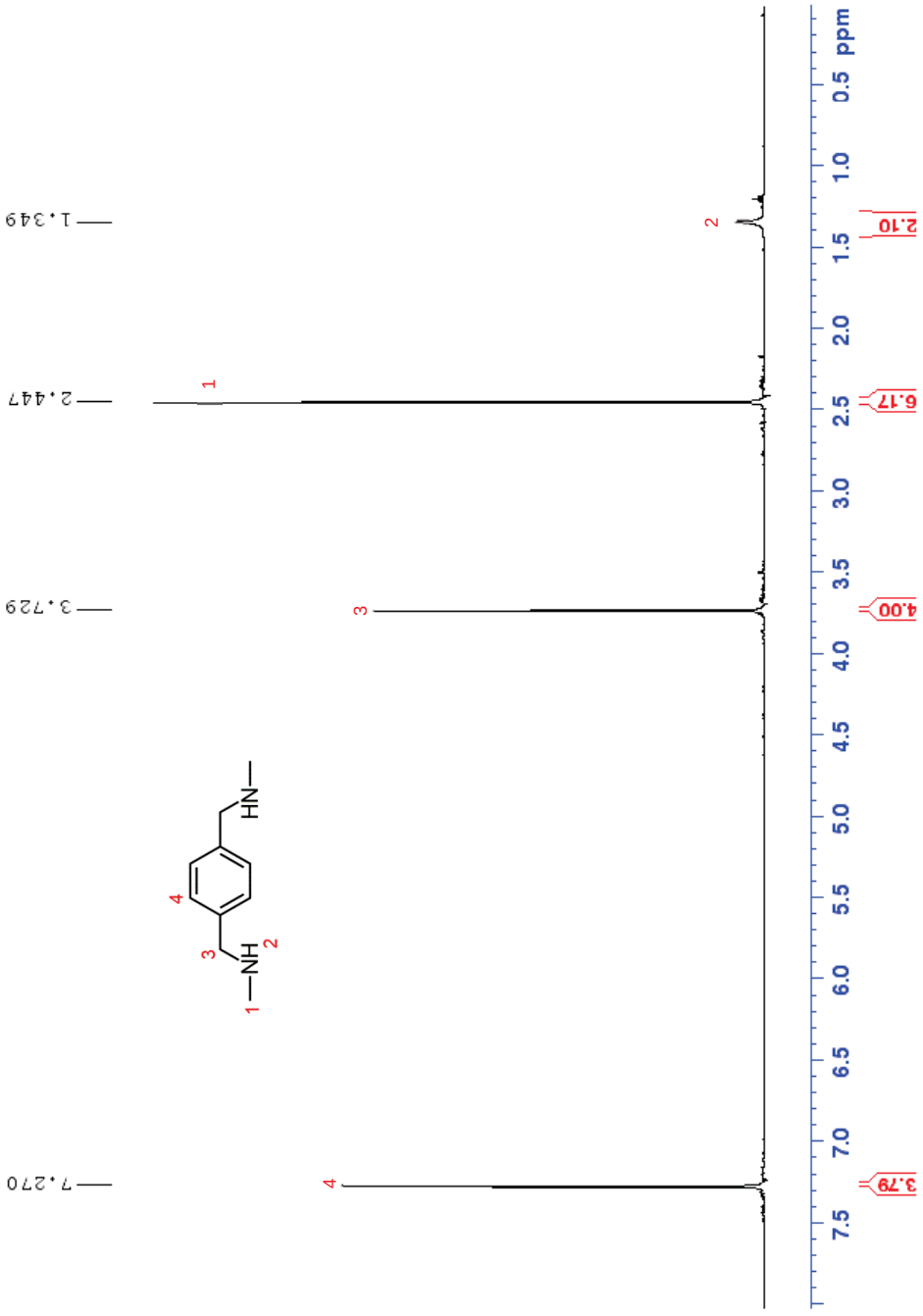

Figure A-7. ^{1}H NMR spectrum of **1a**. Rotated for visual purposes.

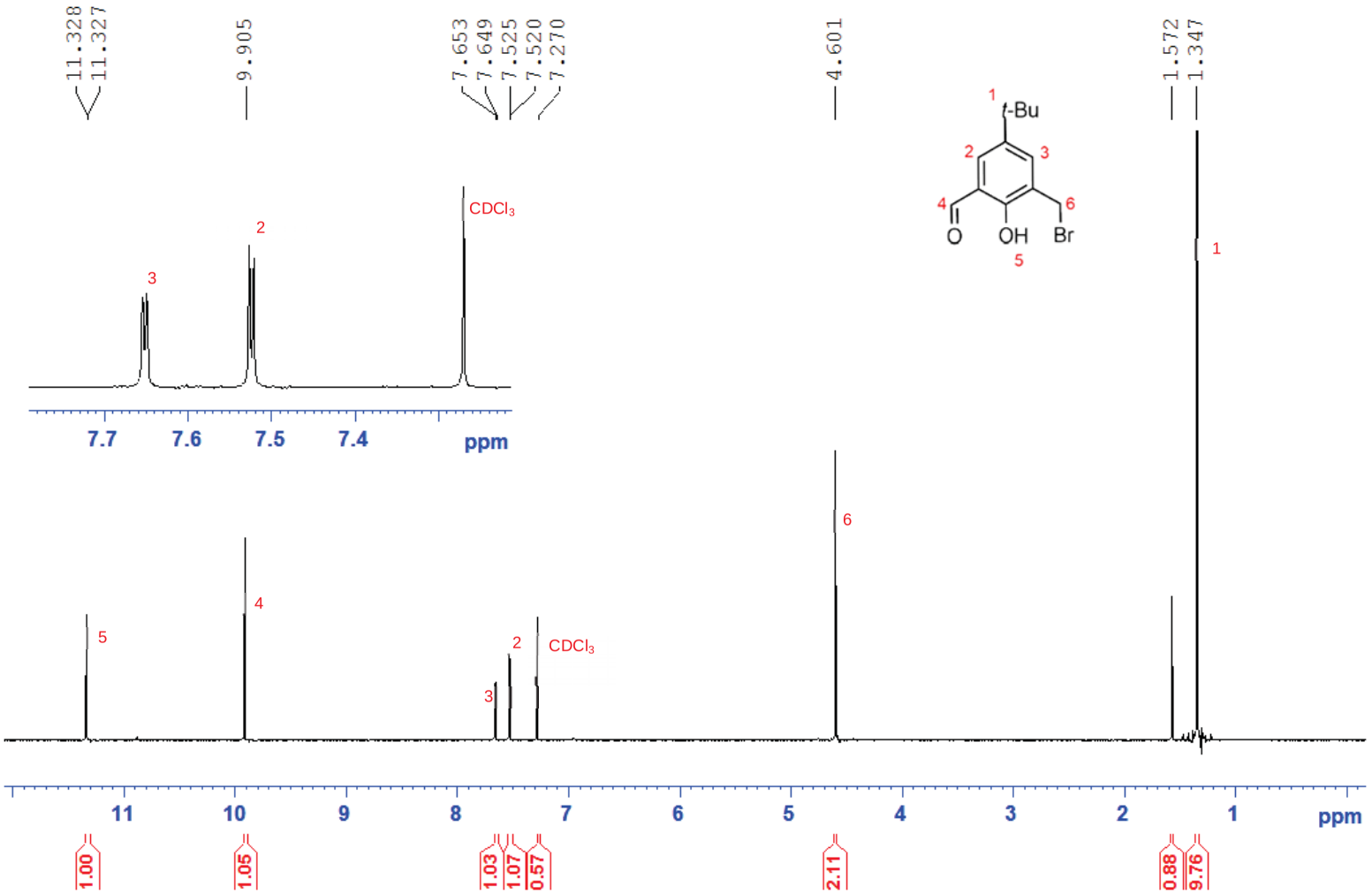

Figure A-8. ^{1}H NMR spectrum of **1b**. Rotated for visual purposes.

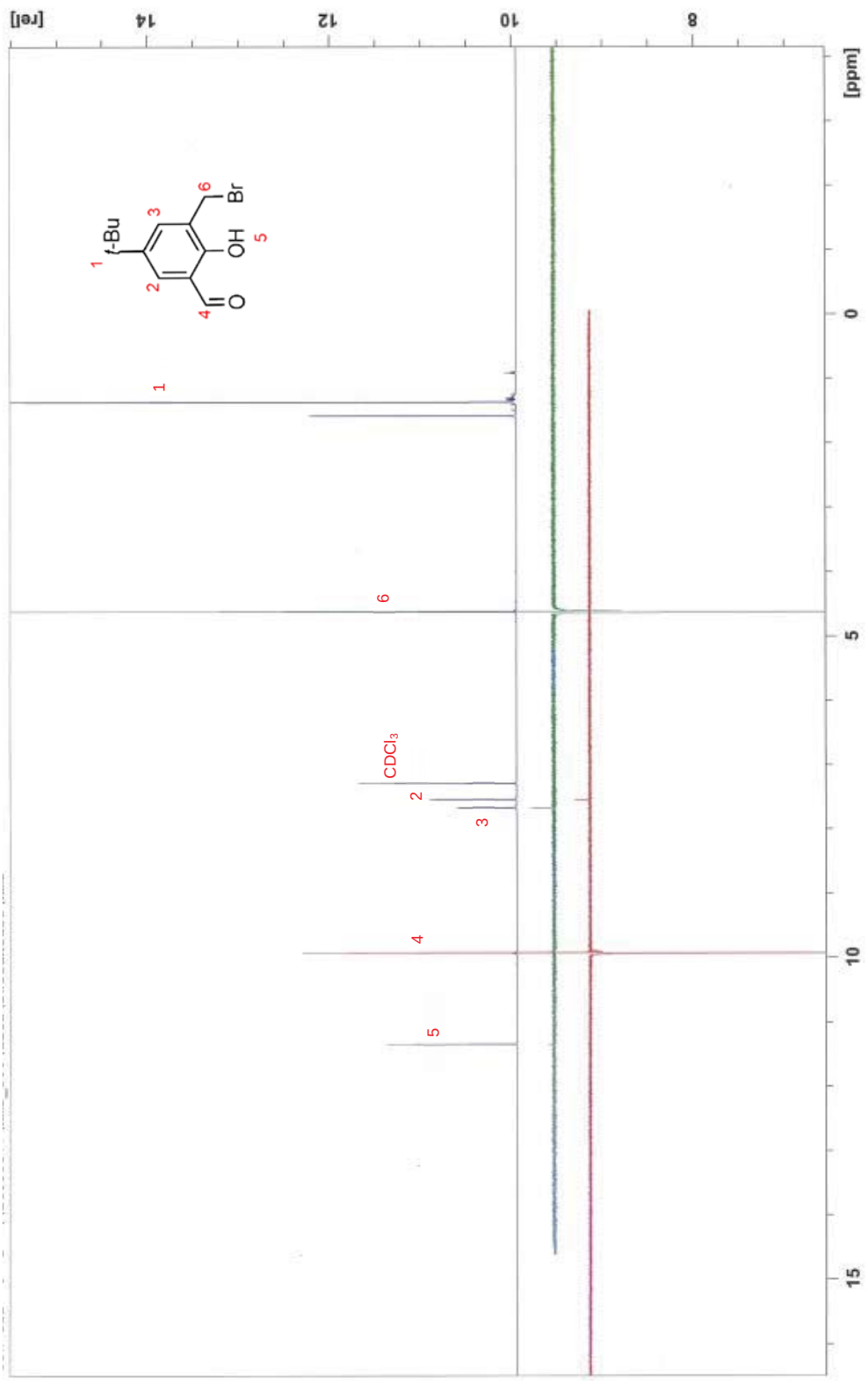

Figure A-9. ^{1}D NOE spectrum of **1b**. Run by Sidney Woodhouse. Rotated for visual purposes.

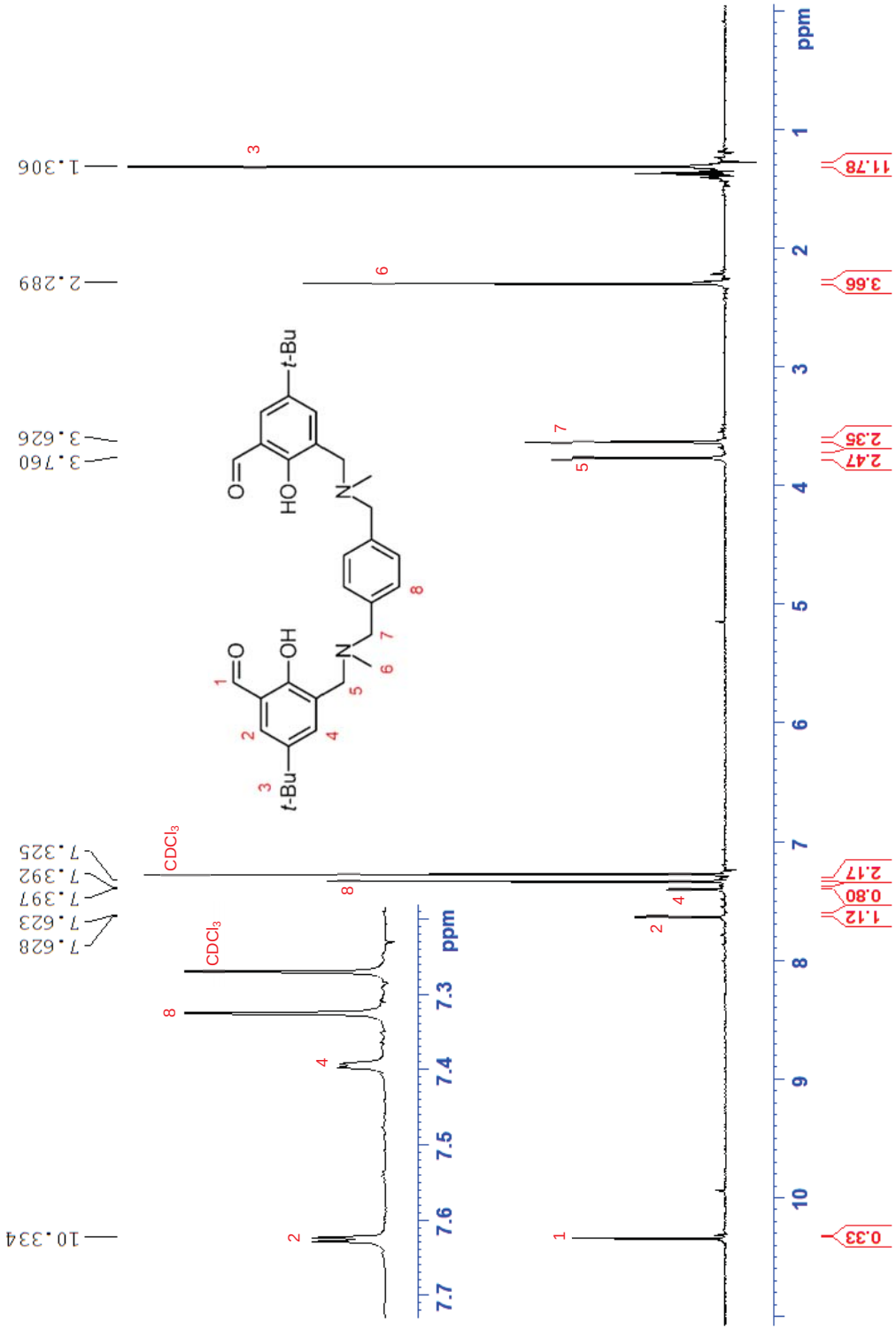

Figure A-10. ^{1}H NMR spectrum of **1c**. Rotated for visual purposes.

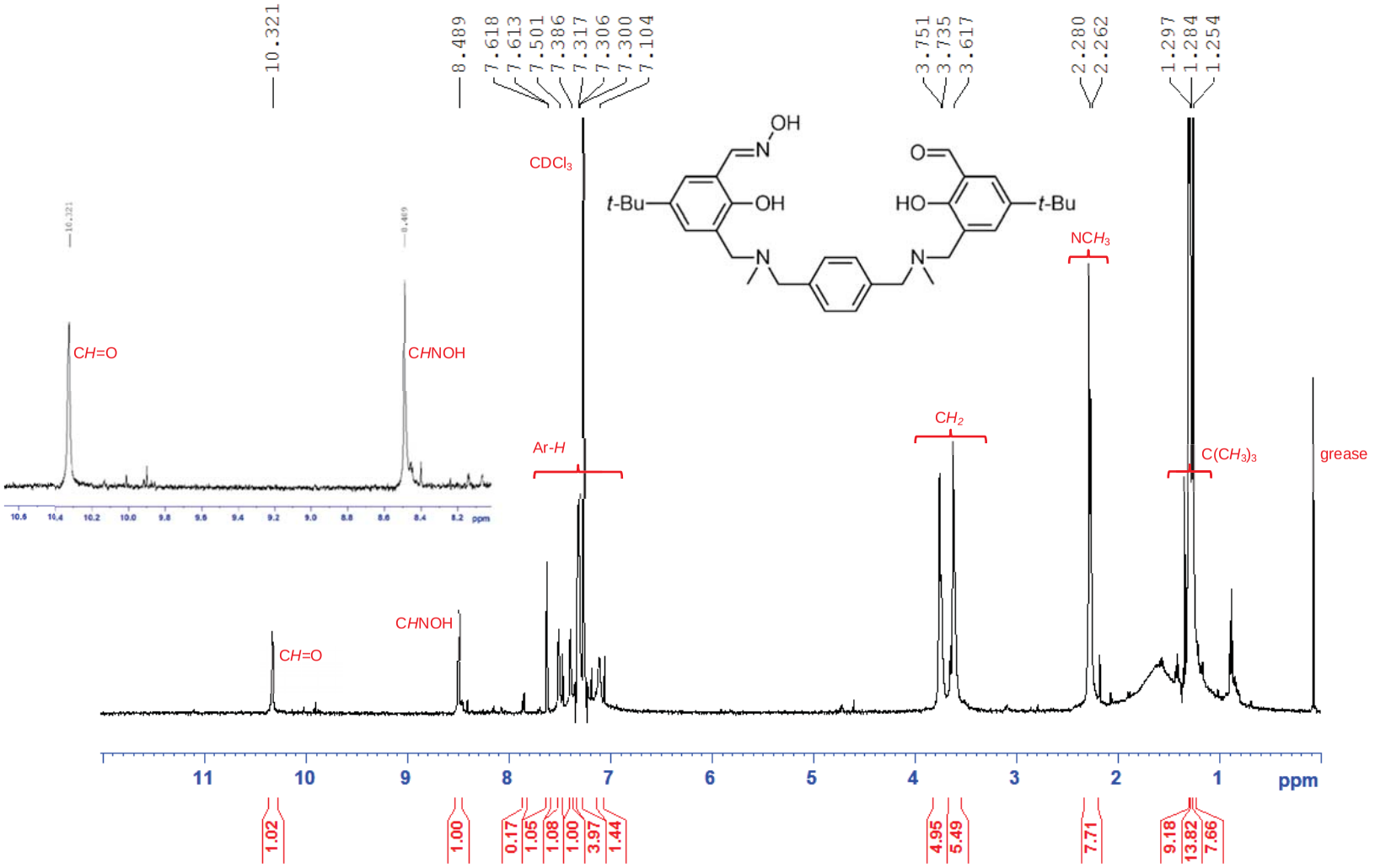

Figure A-11. Initial ^{1}H NMR spectrum of partially oximated ligand **L2** from reaction JKB-126. Rotated for visual purposes.

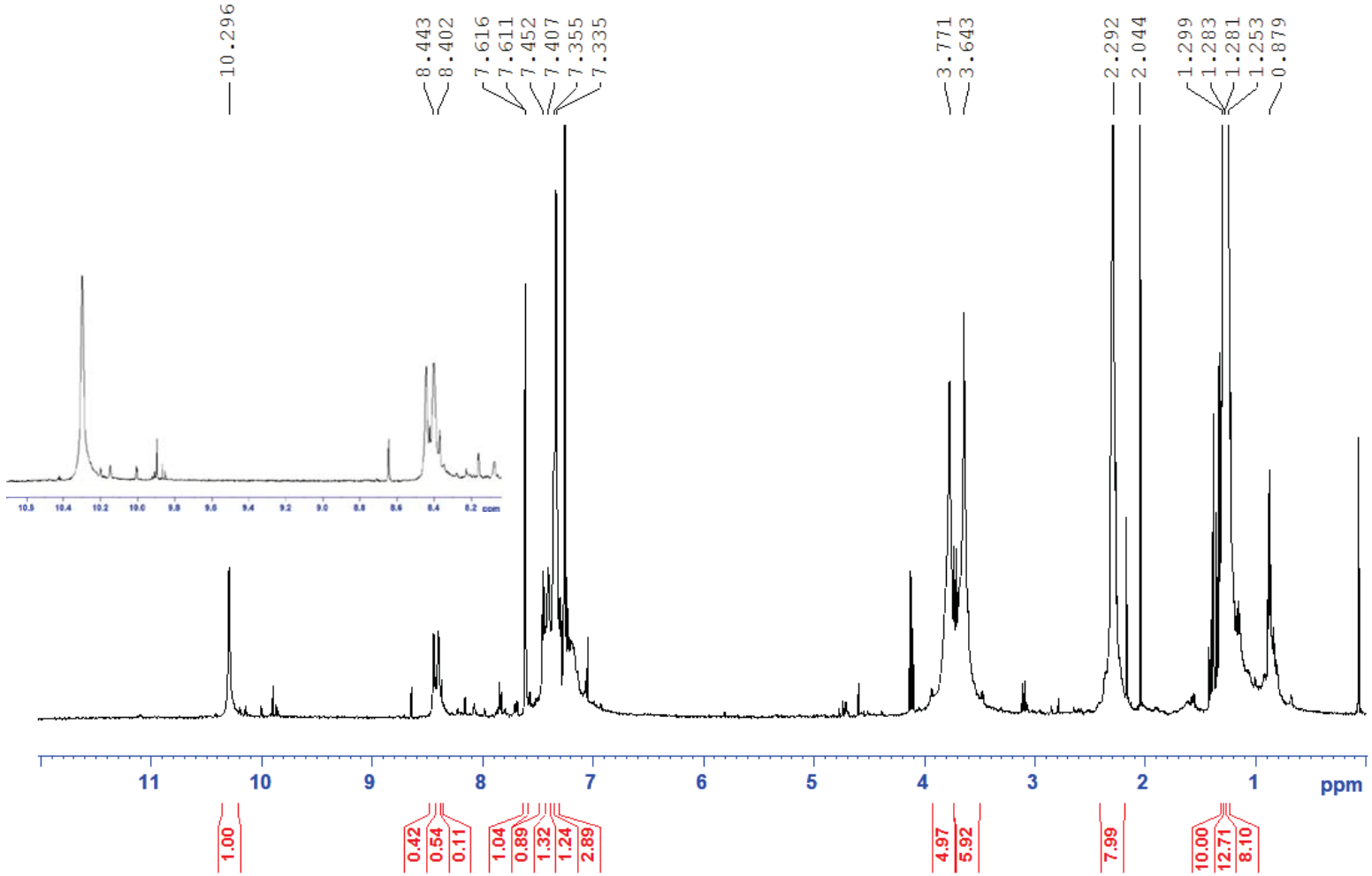

Figure A-12. Initial ^{1}H NMR spectrum of partially oximated ligand **L2** from reaction JKB-126 after filtering off the $MgSO_4$ solid. Rotated for visual purposes.

Appendix 4: IR data

Table A-1. IR data of reactions from Route A.

Reaction Code	Imine Absorption (cm^{-1})	Aldehyde Absorption (cm^{-1})	Viable candidate
JKB-117	1657.2	1697.1	X
JKB-130	1652.3	1695.4	X
JKB-139	1641.1	-	X
JKB-235	1644.2	-	X
JKB-140	1644.8	-	X
JKB-241	1640.9	1695.1	X
JKB-211	1652.8	1695.4	X
JKB-242	1653.2	1695.6	X
JKB-118	1636.2	1693.2	X
JKB-128	1635.4	1694.7	X
JKB-132	1644.3	1695.2	X
JKB-236	1636.4	1693.5	X
JKB-138	1644.1	1693.2	X
JKB-146	1639.8	1696.7	X
JKB-144	1640.8	1694.8	X
JKB-145	1635.0	1696.2	X
JKB-213	1635.7	1695.5	X
JKB-214	1644.8	1694.9	X
JKB-215	1634.8	1695.6	X
JKB-216	1627.5	1696.5	X

Table A-2. IR data of reactions from Route B.

Reaction Code	Imine Absorption (cm^{-1})	Aldehyde Absorption (cm^{-1})	Viable candidate
JKB-217	1633.3	1695.0	X
JKB-251	1633.6	-	X
JKB-218	1642.1	1695.1	X
JKB-221	1631.9	1697.1	X
JKB-263	1635.2	1673.9	X

Table A-3. IR data of reactions from Route C.

Reaction Code	Imine Absorption (cm^{-1})	Aldehyde Absorption (cm^{-1})	Viable candidate
JKB-115	1638.6	1694.7	X
JKB-134	1633.2	1695.5	X
JKB-135	1637.3	1695.1	X
JKB-136	1631.0	1692.7	X
JKB-137	1633.3	1692.5	X
JKB-143	1634.8	1694.5	X
JKB-209	1634.2	1695.4	X
JKB-210	1631.4	1696.8	X
JKB-212	1632.0	1696.3	X

Appendix 5: Mass spectrum of unknown black solid from JKB-263

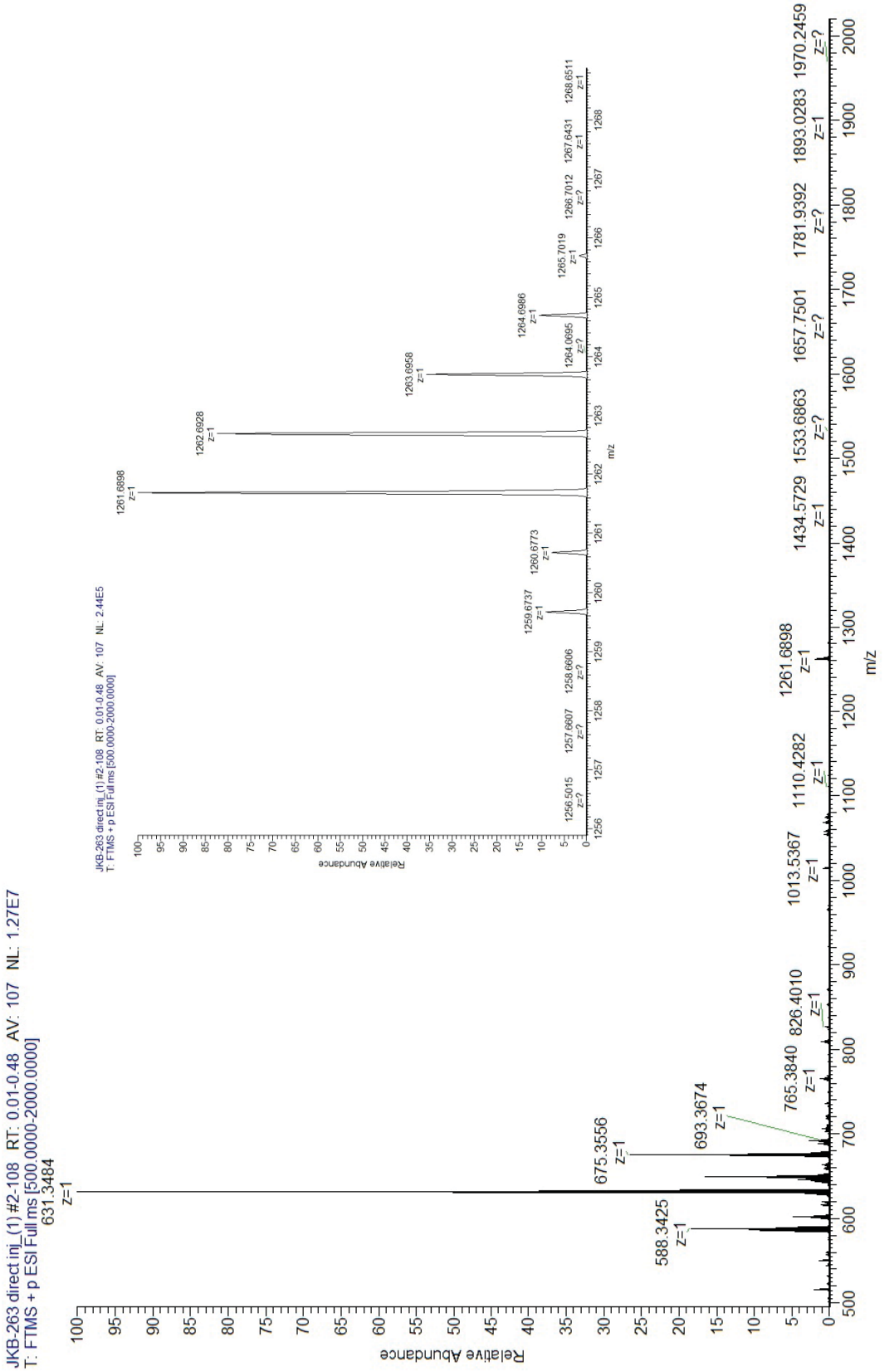

Figure A-13. Mass spectrum of the unknown black solid from reaction JKB-263. Rotated for visual purposes.

Appendix 6: Synthesis of L2 reaction set-up

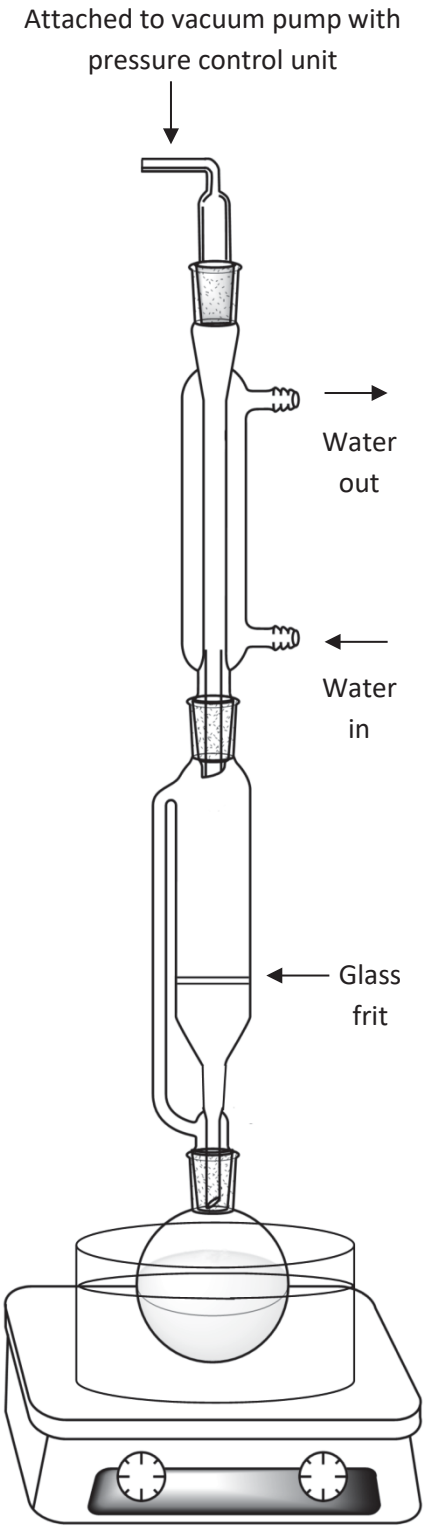

Figure A-14. Reaction set-up for the synthesis of **L2** by slow addition under low pressure.